POLITECNICO DI TORINO

Master’s Degree Course in Automotive Engineering

Deformation and damage models of high strength steels for structural applications in the Automotive industry

Supervisors

Prof. *Paolo Matteis*

Engr. *Daniele De Caro*

Engr. *Matteo Ferrea*

Presented by

Stefano Zarrella

December 2021

To my family

Contents

Introduction

Chapter 1 – Steel in the Automotive industry 1

Bibliography

List of Figures

Chapter 1 – Steel in the Automotive industry

Chapter 2 – The experimental analysis

Chapter 3 – Real case application

List of Tables

Introduction

The objective of this thesis project is to determine, analyse, and implement the different estimating models commonly used in the automotive field to predict the material behaviour in the post-necking region. An additional objective of this project is to comprehend which are the principal damage models used to predict the fracture initiating point on the material, and how these models are implemented concretely. The automotive world is constantly evolving, not only in the technology sector, but also in the material sector. Particularly, the regulations shifted to an always more increased safety in vehicles components and, most importantly, in the passenger cabin. For this reason, improved Advanced High Strength Steels (AHSS), Dual Phase steels (DP), Quenching and Partitioning steels (QP) and others are emerging on the market. Being stronger and lighter, the modern steels allow to reach an improved passengers safety, while guaranteeing low pollutant emissions and low fuel consumption.

Chapter 1 briefly analyse this current situation, putting in evidence the automotive world requests and the solutions adopted in vehicles. The chapter is principally focused on the structural part, and so different microstructures are described, together with the technological processes used to achieve them, in order to understand how the increased strength of these steels has been possible to obtain.

Chapter 2 describes the plastic behaviour implemented for the analysis and fitting of the engineering curve, and necessary to build the true curve which will be used as input for FEM simulations, and the most known damage behaviour models used to study and predict the fracture process of the material under test.

Chapter 3 is focused on the results obtained on all the steels used in this project.

Chapter 1 – Steel in the Automotive industry

Steel makes up about 55% of the average vehicle. In addition to its strength, durability and dependability, steel is also the key to recycling a car at the end of its long life — as steel is continuously recyclable. The steel industry continues to invest in advanced materials and manufacturing technologies that have led to the introduction of a wide variety of new automotive steels. These advanced high-strength steels (AHSS) are strong, lighter, and produced with light life cycle impact, helping automakers decrease a vehicle's life-long carbon footprint. This helps auto manufacturers to reduce the mass of vehicles while maintaining safety standards, thereby increasing fuel economy and reducing tailpipe emissions. The use of current grades of AHSS can reduce a vehicle's structural weight by as much as 25 percent and can cut total life cycle CO_2 emissions by up to 15 percent more than any other automotive material. Today's products are way far stronger than those of a decade ago. The steel industry continues to innovate by introducing new grades and manufacturing processes in support of future mobility, which promises to revolutionize the transportation industry through the proliferation of electrified, connected, and shared autonomous vehicles. As electric vehicles become more commonplace and battery efficiencies improve, use of advanced grades of steel enable reduced weight resulting in a greater range from a single electrical charge.

1.1 The microstructure

To understand how steel is made microscopically, it is necessary to introduce the iron-carbon phase diagram, visible in **Figure 1.1 [1]**. We have to look only up to 2.11% of carbon content. At ambient temperature, pure iron is present in its stable form, *ferrite*, also called *alpha iron*, with a body-centered cubic structure (see **Figure 1.2 [2]**). Ferrite is soft and ductile. At a temperature of 912 °C, the ferrite transforms into *austenite*, also called *gamma iron*, with a face-centered cubic structure (see **Figure 1.2** [2]). Austenite remains stable until a temperature of near 1400 °C, level at which the face-centered cubic structure shifts to a body-centered cubic structure, known as *delta iron*. The iron-carbon diagram is made by considering that the carbon is present as the metastable phase called *cementite* (Fe_3C), that is created with a carbon content of 6.70% in weight.

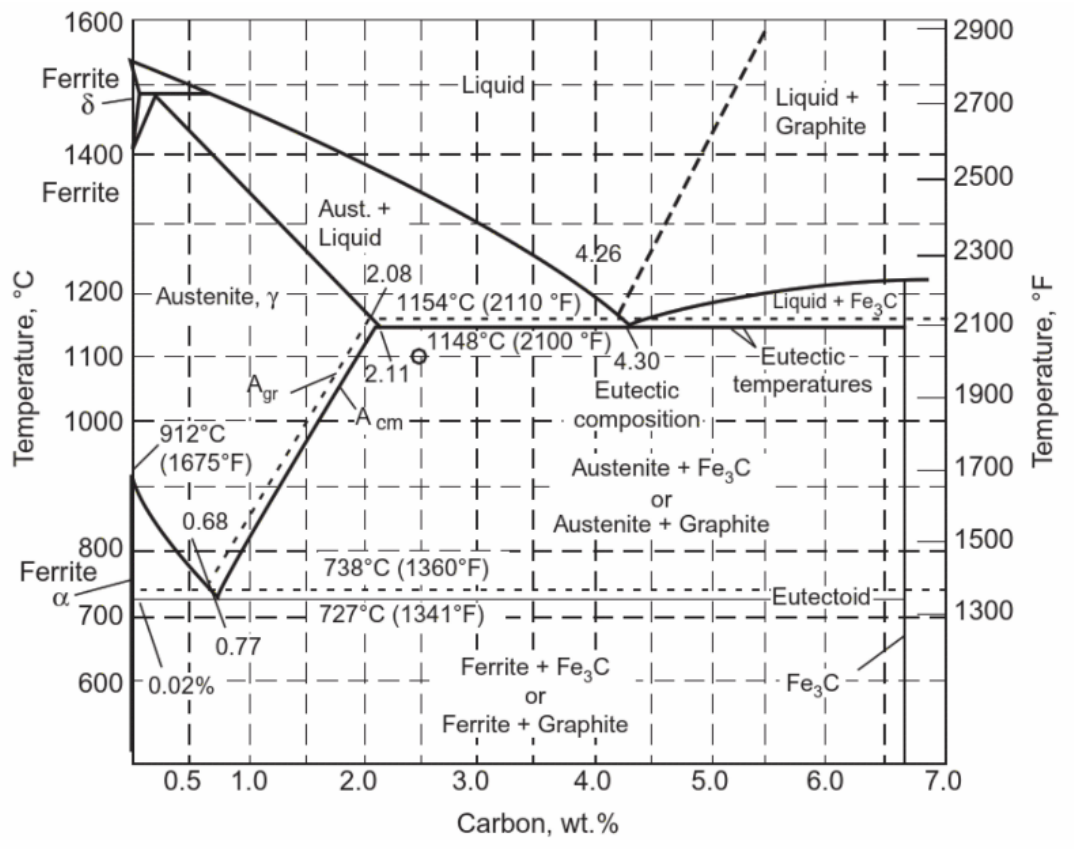

Figure 1.1: Iron-carbon phase diagram
(cementite phase fields with solid lines, graphite phase fields with dashed lines)

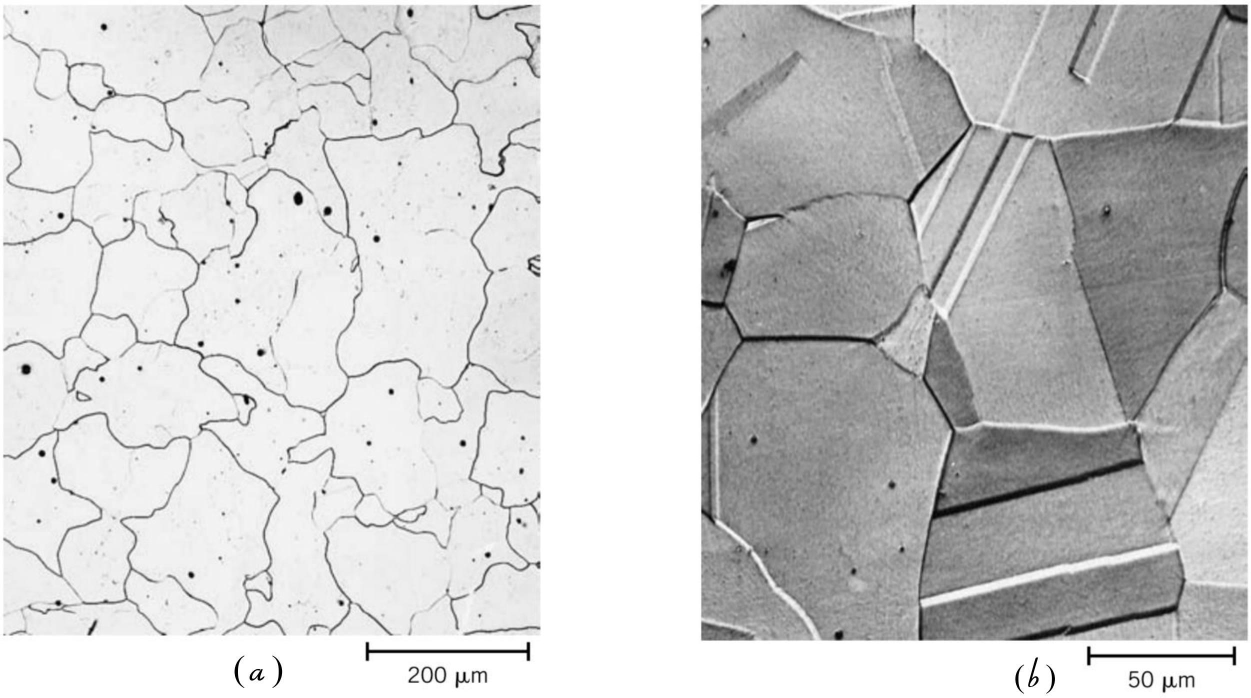

(*a*) (*b*)

Figure 1.2: Microscopic view of ferrite (*a*) and austenite (*b*)

Carbon is an interstitial impurity of iron, and give rise to solid solutions with both ferrite and austenite. It is very little soluble in ferrite, only up to 0.022% in weight. The reason is due to the geometrical configuration of the body-centered cubic structure, which makes difficult the entering of carbon atoms. The maximum solubility level of carbon into austenite is set at 2.11% in weight, at a temperature of 1147 °C. This increment in solubility is due to the face-centered cubic structure of austenite, since interstitial gaps are bigger. In steels, all the carbon is ready in form of iron carbide and not graphite. Cementite is formed when the solubility limit of carbon in alpha iron is exceeded below 727 °C, that means below the eutectoid temperature. This temperature is the one at which there is the eutectoid reaction of the austenite in alternated lamellae of alpha iron mixed with cementite, a structure that is called *pearlite*, which is also the typical structure in the majority of steels (see **Figure 1.3** [2]). This chemical process occurs at the eutectoid composition, that means when the carbon content is 0.77% in weight. Pearlite is present in grains, or colonies. Inside each colony, the lamellae have the same orientation, which instead varies between the colonies. The white stripes are made by ferrite, the black ones are made by cementite. This structure has intermediate mechanical properties between ferrite and cementite.

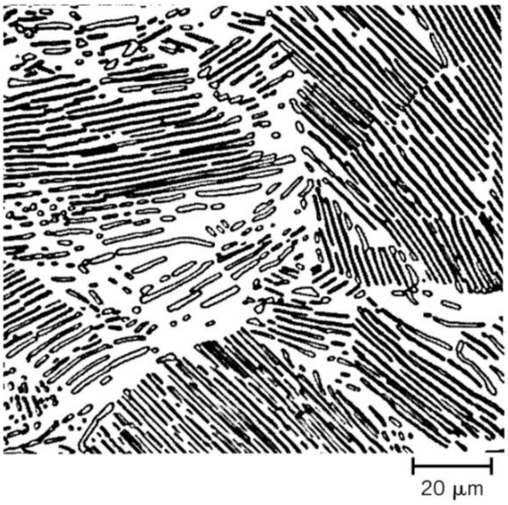

Figure 1.3: Microscopic view of a eutectoid steel (the microstructure is pearlite, in which ferrite is white and cementite is black)

When the carbon content is lower than 0.77% in weight, the steel has an hypoeutectoid structure. With respect to the eutectoid process, in this case there is an additional phase. Let's assume that the initial material is fully austenite and it cools. When the temperature lowers down over the austenitic region, particles of alpha iron, or ferrite, starts to originate on the boarders of the austenitic grains, and two phases are simultaneously present. The ferrite grains continuously grew in dimensions until the temperature reaches the eutectoid value, 727 °C as saw before, and the eutectoid reaction takes place, giving rise to pearlite in its lamellar structure. Since there is an additional phase with respect to the eutectoid case, a quantity of ferrite forms its own phase, which coexists with pearlite, and it is called *proeutectoid ferrite*.

The ferrite that, instead, is present in pearlite, is called *eutectoid ferrite*. **Figure 1.4** shows an example of the microstructure of a hypoeutectoid steel. **[2]**

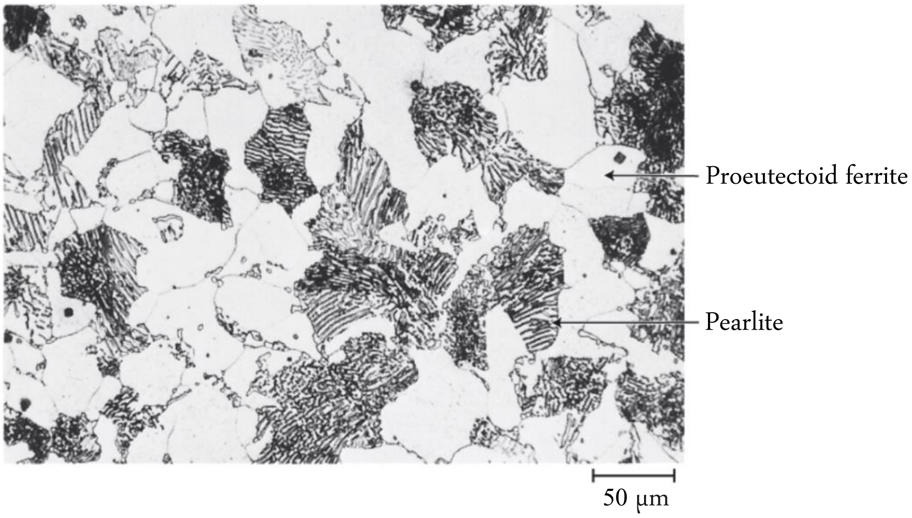

Figure 1.4: Microscopic view of a hypoeutectoid steel

A similar process happens also for steels that have inside a carbon content between 0.77% and 2.11% in weight, the so-called hypereutectoid steels. Also in this case there is an additional phase with respect to the eutectoid condition. The material, complete austenite, is cooled down until the border of the austenite region is reached. When the temperature goes down, two phases exist: austenite and cementite. Cementite starts to form on the border defined by the austenite grains, as seen for the hypoeutectoid steels, and those grains increase their dimensions until the eutectoid temperature is achieved. Since the iron carbide is originated before the eutectoid temperature, not all the cementite will be with pearlite, but a certain amount will be in a separate phase, called *proeutectoid cementite*. The cementite which is part of pearlite, together with ferrite, is called *eutectoid cementite*. **Figure 1.5** [2] shows an example of the microstructure of a hypereutectoid steel.

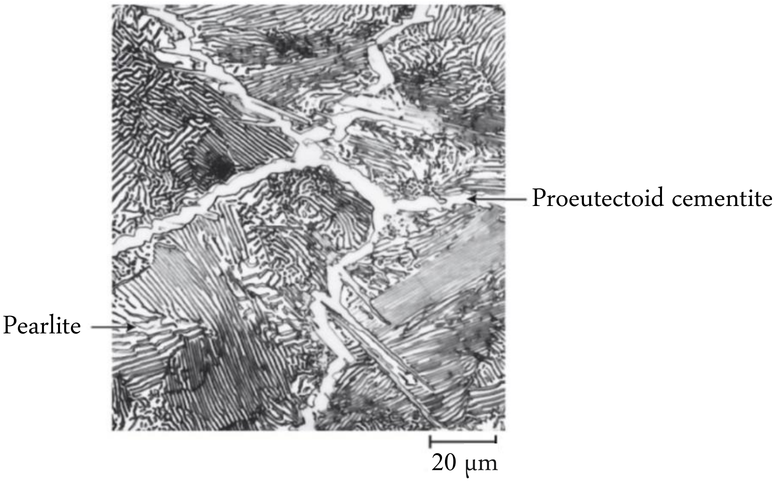

Figure 1.5: Microscopic view of a hypereutectoid steel

Cementite is much harder and more brittle than ferrite. If its fraction inside steel increases, hardness and strength will noticeably improve. Ultimate strength, yield strength and Brinell hardness are variables that always increase with the carbon content, or with the equivalent content of the cementite. However, since cementite is also brittle, ductility and toughness decrease if the quantity of cementite rises up.

1.1.1 The Time-Temperature effect

The pearlite formation occurs when the cooling speed is low. The cooling speed is set by the cooling temperature kept in time. When temperature changes, also the time required to the transformation process from one structure to the other changes. There are cases, such as that of pearlite, in which a reduction of the cooling temperature leads to a reduction in time of the transformation from austenite to pearlite; other cases, such as that of bainite, in which a reduction of the cooling temperature leads to an increase in the transformation time required to pass from austenite to bainite.

To obtain a pearlitic structure, the cooling temperature lies in the range between 540 °C and 700 °C. Lowering the cooling temperature inside this range leads to a reduction in time for the creation of pearlite. When the cooling temperature is just below the eutectoid temperature, the pearlite obtained is the *gross pearlite*, in which the lamellae of ferrite and cementite are larger. Vice versa, when the cooling temperature is near to 540 °C, the diffusion speed of the carbon atoms decreases, and the pearlite that is created is the *thin pearlite*, which is harder and stronger than gross pearlite (which instead is more ductile) due to the higher dimensions of the cementite grains, that reinforce the entire structure.

When the cooling temperature is kept below 540 °C another structure is produced, *bainite*. The bainite is still made of ferrite and cementite, but while in pearlite these elements are lamellae, in bainite these elements are in the form of needles or cleats, depending on the transformation temperature. Particularly, cementite is extended inside the ferritic matrix. Another difference with pearlite is that in the bainitic structure proeutectoid phases are not present. Nevertheless, they share a common property: when austenite is completely transformed into pearlite or bainite, it is not possible to go then from pearlite to bainite or vice versa. Once the microconstituents are created, they cannot be transformed into other ones. This is possible only by heating the material again until it is passed to austenite, and repeat the cooling process. Steels with bainitic structure are harder, more resistant, and more ductile than steels with pearlitic structure, due to the fact that cementite in bainite is thinner and smaller than that available in pearlite. Bainite, shown in **Figure 1.6** [2], can be formed in the range of temperatures that go from about 200 °C up to 540 °C.

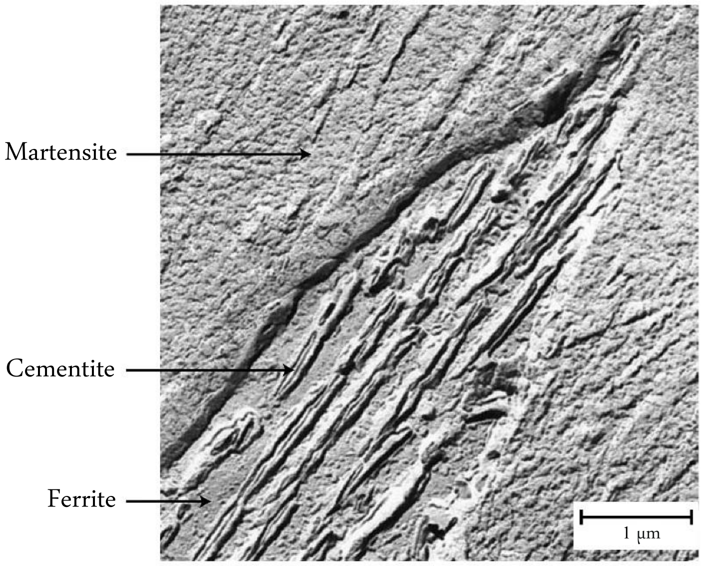

Figure 1.6: Microscopic view of bainite

From bainite, or pearlite, it is possible to obtain another microstructure. When steels with pearlitic or bainitic structures are heated to a temperature lower than the eutectoid one, and it maintained for long time (about 20 hours), the structure generated is the *spheroidite*. Simply, the ferrite and cementite assume another different geometrical disposition: cementite consists in small spheres englobed in a ferrite matrix. Spheroidite is soft and ductile, and it is useful to soften the steels to give them a greater formability. Softness and ductility are much higher than those of gross and thin pearlite, and alloys with a pearlitic structure are harder and more resistant than alloy with a spheroiditic structure.

The last microstructure that steels can assume is the *martensite*, a non-equilibrium monophase. This composition is formed when the steel, brought to the austenitic phase, is cooled very quickly near to the ambient temperature, according to the operation of quenching, that will be described more in detail in another section. With this thermal process, the austenite is transformed in martensite without diffusion of carbon atoms, and this explains the extremely fast speed of transformation. Geometrically, the carbon passes from a face-centered cubic structure of austenite to the body-centered tetragonal structure of martensite, which is a body-centered cubic structure with an elongated vertical dimension. Martensite grains assume the form of needles or cleats, as it is visible in **Figure 1.7***a*. [2] The white area represents the residual austenite that has not transformed during the quenching process. After that operation, a volume increase manifests. Amongst all the structures described, martensite is the hardest and strongest structure that steels could have. With a negligible ductility, it is also the most brittle one, and it is a limiting factor in most applications. There are also internal tensions inside martensite that weaken the entire structure. To solve the problem, we recur to *tempering*. The tempering thermal process consists in heating the martensitic steel at a temperature in the range 250 °C to 650 °C. In this way, internal tensions soften, and two phases are present, constituted by ferrite and cementite. The martensite obtained is called *tempered martensite*, and it is visible in **Figure 1.7** *b* [2] The cementite particles are very small, and are surrounded by ferritic matrix.

The properties of the tempered martensite are the very high levels of hardness and strength, near those reached by martensite, but with improved ductility and toughness, characteristics that allow the tempered martensite to be lot more suitable for engineering applications.

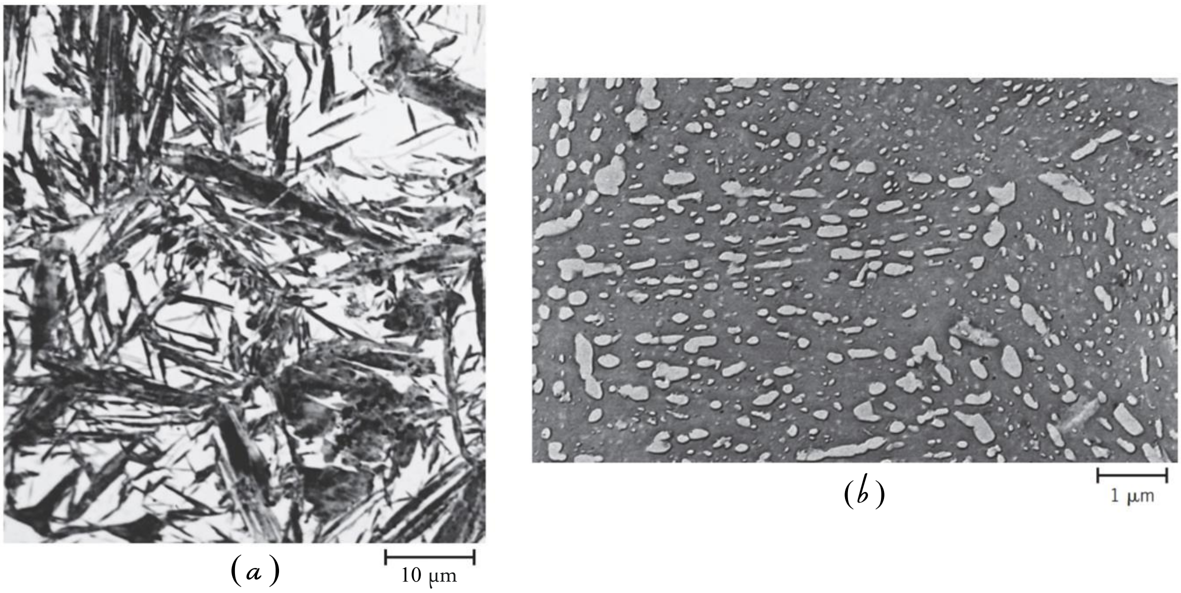
(*a*)

(*b*)

Figure 1.7: Microscopic view of martensite (*a*) and tempered martensite (*b*)

However, it is important to control the tempering process, since the dimension of the cementite grains affect the mechanical properties of the tempered martensite. Temperature and time are the main variables to observe and monitor. If the iron carbide particles are bigger, the material results to be less hard and less strong, although more tough and more ductile, due to the fact that the ferrite-cementite interface surface is reduced. Increasing the temperature, the growth speed of the cementite particles increases, and so it is the trend of the softening of the material. It can happen that tempering could affect the toughness of the material, decreasing it. This is particularly true when the tempering is done between 375 °C and 575 °C, and the phenomenon is more likely to occur for alloyed steels. To avoid the problem, it is possible to control and modify the alloying elements and their composition into the steel, or performing the tempering process outside the temperature interval written before.

Figure 1.8 [2] summarizes the transformation process of austenite into the different microstructures described so far. The red and green lines indicate, respectively, the starting and ending point of the transformation process, while the blue dashed line indicates the points in which the transformation is completed at 50%. **A** stand for Austenite, **P** for Pearlite, **B** for Bainite, **M** for Martensite. The line corresponding to the martensitic transformation is horizontal because it is independent from time.

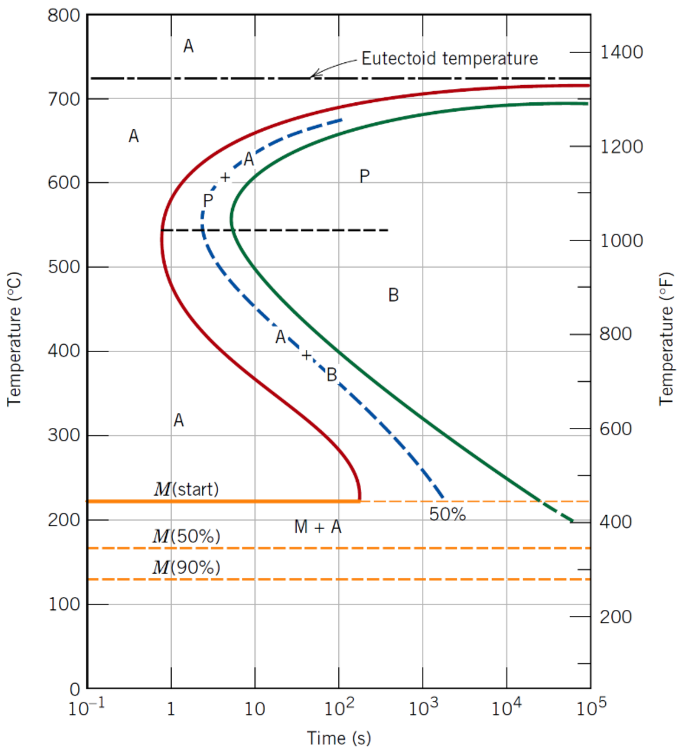

Figure 1.8: Time-Temperature transformation diagram for eutectoid iron-carbon alloy

1.2 The effects of the alloying elements

This sub-chapter starts by explaining the influence of the alloying elements on the microstructures previously described, and ends by summarizing the main mechanical properties affected by each of them. The main alloying elements in steels are titanium (Ti), tungsten (W), silicon (Si), vanadium (V), nickel (Ni), chromium (Cr), molybdenum (Mo), manganese (Mn), and cobalt (Co). Other materials that could be added to steels are aluminium (Al), copper (Cu), sulphur (S), lead (Pb), phosphorus (P), boron (B), nitrogen (N), beryllium (Be) **[3]**.

The alloying elements have two principal effects. There are elements called *α-stabilizers* which shrink the austenite region, favouring the formation of ferrite outside the limiting region of the iron-carbon diagram, while other elements called *γ-stabilizers* that, vice versa, enlarge the austenitic region, favouring so its formation outside the limits defined by the iron-carbon diagram, as depicted in **Figure 1.9** **[4].** Silicon, aluminium, beryllium, phosphorus, titanium, vanadium, molybdenum, chromium, and boron are all included in the class of α-stabilizers. In this case, ferrite will be present more easily, and those alloying elements are used particularly for steels which have to be magnetically soft for electrical transformers.

Elements such as carbon, nickel, nitrogen, manganese, and cobalt, but also inert metals like ruthenium (Ru), rhodium (Rh), palladium (Pd), osmium (Os), iridium (Ir), and platinum (Pt) are included in the class γ-stabilizers. If added in sufficiently high concentration, ferrite is completely replaced by austenite, which will be present at lower temperatures than the eutectoid one visible in the iron-carbon diagram.

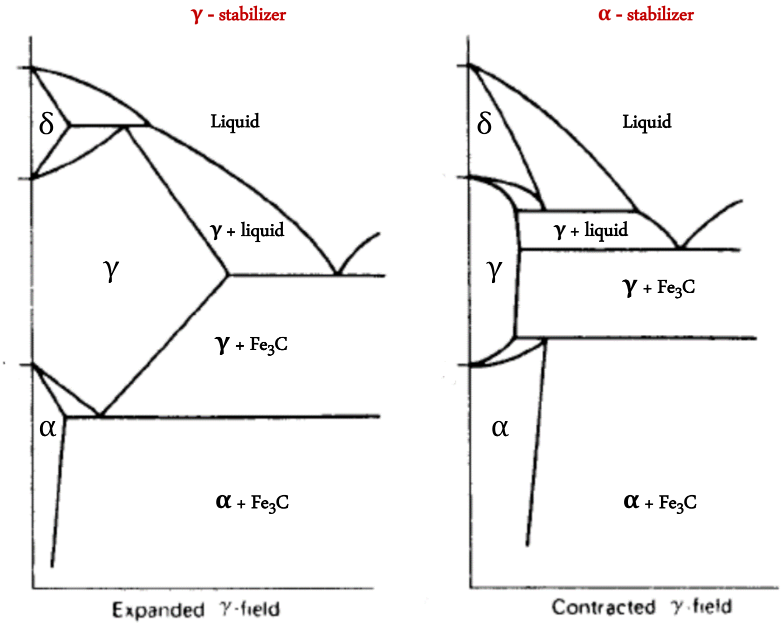

Figure 1.9: γ-stabilizer and α-stabilizer cases

According to the studies performed by Bhadeshia, Harshad K. D. H., et al. [4], the alloying elements are classified in three categories, depending on their abilities to create solutions with ferrite and cementite phases. The first one includes all the elements that are able to enter in solution only with ferrite phase, such as copper, nickel, silicon, and phosphorus. The second category encompasses those materials which can be bonded both with cementite and ferrite, although in low concentration. Bonding with ferrite, they increase its strength. At higher concentrations, instead, the chemical bond with cementite prevails, and the carbides so formed are thermically more stable than cementite. Elements that fall in this category are chromium, molybdenum, manganese, titanium, tungsten, and vanadium. The third and last category is reserved for elements which can form solutions only in the cementite phase. Here, nitrogen (the main one), titanium, and aluminium are present.

Furthermore, the presence of allying elements tends to shift the time-temperature curve of **Figure 1.8** to the right, obtaining results similar to those visible in **Figure 1.10** [2], obviously depending on the type and concentration of the alloying elements. The 4340 Alloy Steel contains iron for 96%, nickel for 2%, carbon for 0.4%, and chromium, manganese, molybdenum, and silicon all under 1% in weight.

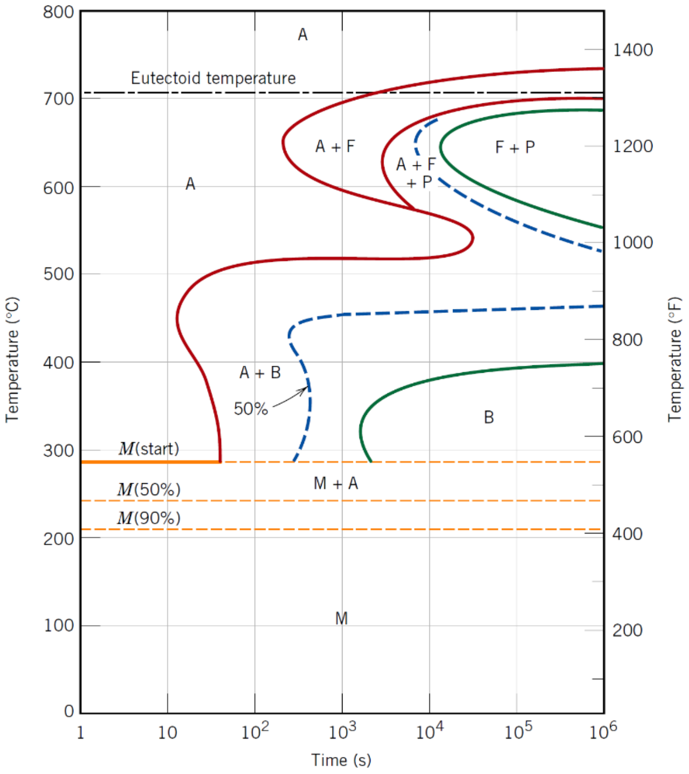

Figure 1.10: Time-Temperature transformation diagram for 4340 Alloy Steel

The slowing down and delay of the ferrite and pearlite reactions by alloying elements enables these reactions to be more readily avoided during heat treatment, so that the much stronger low-temperature phases, such as bainite and martensite, can be obtained in the microstructure. The hard-martensitic structure is only obtained in plain carbon steels by water quenching from the austenitic condition whereas, by the addition of alloying elements, a lower critical cooling rate is needed to achieve this condition.

From **Figure 1.10** we can see that the greatest modification occurs in the bainitic field. The temperature range in which bainite can formed is drastically reduced with respect to the eutectoid case. The reason is of course the presence of alloying elements, but amongst them carbon has the most influence. Indeed, carbon is much more soluble in austenite than in ferrite, and presence of carbides in steel increases as the carbon content goes up, which has the limit of no more than 0.5% in weight to maintain reliable mechanical properties.

It is important to notice that the presence of the alloying elements, and especially their concentration, has effects also on the eutectoid temperature and on the eutectoid composition, intended as carbon content. With the exception of manganese and nickel, the eutectoid temperature rises as the concentration of alloying elements increases, while the carbon content in the eutectoid composition decreases. These effects are clearly visible in **Figure 1.11** *a* and **1.11** *b* . [2]

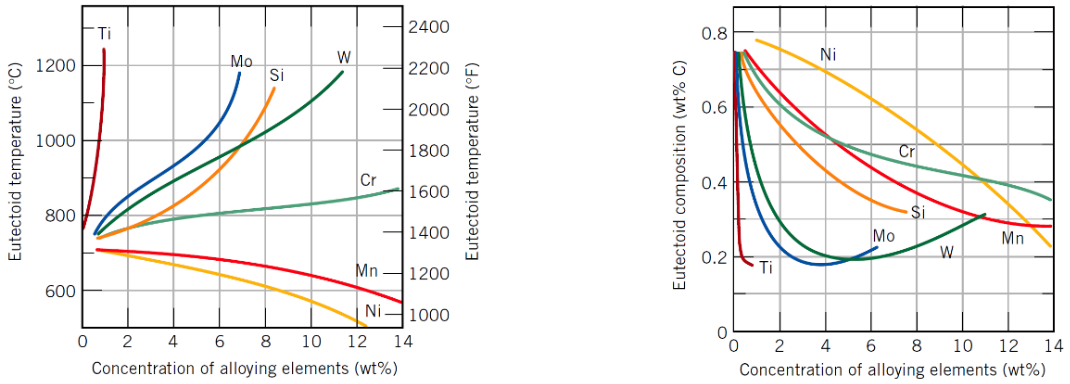

(*a*) (*b*)

Figure 1.11: Effect of the alloying elements on the eutectoid temperature (*a*) and eutectoid composition (*b*)

Excluding cobalt and aluminium, the alloying elements lower the temperature at which the formation of martensite begins. However, carbon has a big impact on it, as it can be seen in **Figure 1.12** [1]. M_S and M_f identify, respectively, the starting temperature and ending temperature of the martensite transformation process. It can be easily seen that a very low amount of carbon content consistently decreases both the temperatures, up to 300 °C. With a carbon content of about 0.7% or more, the martensitic temperature M_f will be below room temperature, so high-carbon steels quenched in water usually contain retained austenite at ambient temperature, with lower performances than martensite. For this reason, the amount of carbon content is controlled up to 0.4% in weight. That value has been proven to be the best deal between mechanical properties and transformation processes. The other alloying elements have their contribute too, but carbon has the predominant one. We conclude the argumentation on the effects of the alloying elements by briefly summarizing the ameliorative actions of each one, in order to understand why they are used in steels.

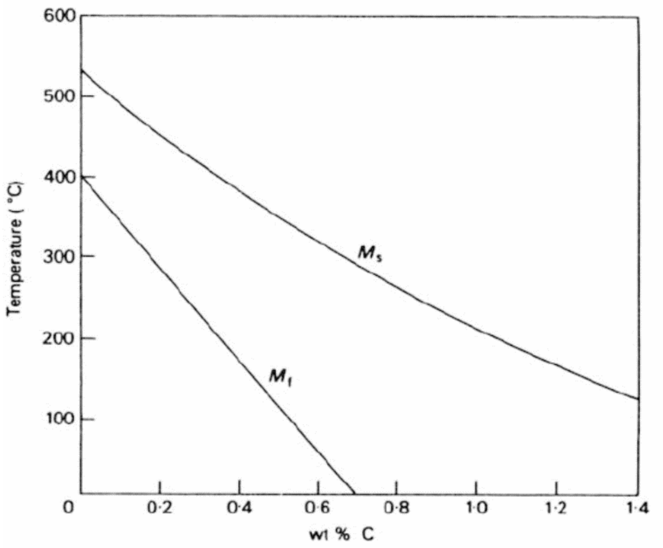

Figure 1.12: Effect of carbon content on M_S and M_f

Carbon – The base element inside steels, in the combined form of cementite (Fe_3C). Carburizing steels have a carbon content beneath 0.2%, quenching and partitioning steels contain from 0.2% to 0.6% in weight, while steels for tooling have inside from 0.6% to 2.1% of carbon in weight [3]. A carbon presence superior to 0.2% in weight proportionally reduces machinability, weldability, toughness, and cold plasticity, while increases tensile strength, hardness, hardenability, and wear resistance.

Nickel – In stainless steels its amount could reach 25% [3]. It is usually added with chromium, or molybdenum, or both. Nickel is able to increase mechanical and corrosion resistance, and hardness in case of annealing or quenching and partitioning. It also improves resilience at low temperatures and the hardenability, operation that could be done at lower temperature and speed. With chromium, it increases ductility and fatigue resistance **[5]**.

Chromium – In stainless steels it is present from 3% to 25% in weight [3]. Usually, it is added with other alloying elements, but could also be present individually. Its effects are similar to those of nickel, but in case of annealing the chromium, besides enhancing hardness, also increases brittleness. This means that, to solve the problem, steels alloyed with chromium have to be worked with a quenching and partitioning operation, in order to improve the mechanical resistance at high temperatures. In high-carbon steels, chromium brushes up wear and abrasion resistance **[6]**.

Molybdenum – In stainless steels molybdenum can be found up to 2.5% in weight [3]. Normally it is coupled with nickel and chromium, but nothing prevents its presence with other elements. This material is able to increase the mechanical resistance and hardness at high temperatures, it improves machinability, hardenability, wear resistance, and allows to slow down the enlargement rate of the austenitic grains while reducing also the brittleness due to tempering **[7]**.

Vanadium – It is present in steels always with other alloying elements, and in small quantities. Vanadium is able to form carbides which tend to harden, so it is an element able to maintain good hardness at higher temperatures. It also improves tempering resistance and elasticity [3].

Manganese – It is used as alloying element for quantities that does not exceed 2% in weight [3]. Manganese decreases the temperature at which the martensite transformation begins, with minor increases in retained austenite contents. This translates into higher yield and tensile strength values, so steel gains higher resistance **[8]**. Furthermore, also hardness is improved, thanks to the uniform distribution of the carbide phase in the austenite phase **[9]**.

Silicon – Steels has a silicon content not superior to 2% in weight [3]. It improves yield and tensile strengths, and fatigue resistance, but increases also the brittleness, that could be corrected with a process of quenching and partitioning. Furthermore, it ameliorates the oxidation resistance at high temperatures, the wear resistance, but decreases the formability both at low and high temperatures **[10]**.

Titanium – It helps in upgrading the corrosion resistance and the weldability of steels [3].

Tungsten – It allows to increase the mechanical properties at high temperatures. The maximum levels of hardness are achieved with a content that goes from 13% to 25% in weight [3].

Copper – Present in small quantities, less than 0.2% in weight [3], in almost all the steels. It is able to refine the corrosion resistance and to raise the elasticity limit.

Phosphorus – Present only in small quantities, about 0.035% in weight [3], due to the fact that it increases the grain dimensions. However, it improves the corrosion resistance and decreases the steel toughness.

Boron – Used in very small amounts, no more than 0.01% in weight [3], to improve hardenability. It also reduces toughness and increases the austenitic grains dimensions.

Cobalt – Used to increase the tempering resistance and the hot hardness by the action on the martensite grains, similar to what molybdenum, tungsten, and vanadium do too. Employed in tools steels.

Aluminium – It acts as deoxidizer.

1.3 Classification

The basic classification of steels includes four types of steels. Carbon steels look opaque, and are vulnerable to corrosion. These steels are in turn divided in three categories: *low-carbon steels* contain an amount of carbon not superior to 0.30%, *medium-carbon steels* have carbon of about 0.60% in weight, and in *high-carbon steels* the amount of carbon content could reach 1.5% in weight [3]. Containing very small amounts of other alloying materials, carbon steels are exceptionally strong, and this is the main reason of their use in the automotive industry. The second type of steels is characterized by the alloy steels. Alloy steels have a combination of different alloying elements, whose concentrations directly affect the strength. These steels tend to be cheaper than carbon steels, and are more resistant to corrosion. Another type of steels used in the automotive world is the stainless steel. Stainless steels have a chromium content that could reach 25% in weight [3], which is the main alloying element. The main advantages of stainless steels are their resistance to corrosion and their ability to be easily moulded into various shapes. Finally, there are tool steels, which are not used in automotive applications. Alloyed with cobalt, molybdenum and tungsten, they are hard and both heat and scrape resistant, and that's why they are widely used to make metal tools. In automotive industry, the classification of steels is different. In this sector we consider deep drawable steels, hot forming steels, High Strength Low Alloy (HSLA) steels, dual-phase steels, TRIP steels, and quenching and partitioning (QP) steels **[11]**.

1.3.1 Deep drawable steels

Deep drawing steels are used normally in the form of sheets which are formed into formed products by a sheet forming process. The commonly used processes for sheet forming are deep drawing and stretch forming processes. Deep drawing is the most popular steel forming process available to manufacturers since it offers outstanding forming characteristics and good resistance to ageing. Deep drawing is a process that involves using a die to form blank sheets of metal into a desired shape around a punch. For performing effectively this operation, the steel must have good formability, so it has to be able to plastically deform without rupturing. The parameters that affect the ability of a steel to be deep drawn are its chemical composition, its microstructure, its surface quality, and its mechanical properties, as well its anisotropy. Anisotropy is the property by which a material has mechanical characteristics which depend in the direction, for example along different axis. In deep drawable steels, both planar and normal anisotropy are very important. The higher the normal anisotropy and the lower the planar anisotropy, the better is the steel sheet for forming operation.

Two main categories exist for deep drawable steels, aluminium killed (AK) steels and interstitial free (IF) steels. [1] Aluminium killed (AK) steels are those in which aluminium has been added to deoxidize them. Instead of aluminium, other additives could be introduced, such as nitrogen, carbon, and manganese. The steel is referred to be 'killed' for the reason that it will silently go through solidification process in the mould, with no gas getting out of the mould. The addition of nitrogen produces aluminium nitride (AIN), which allow the steel to increase its strength at high temperatures. In particular, the optimal nitrogen content is set in the range 0.005% to 0.01% in weight, while the optimal aluminium content is found in 0.025% to 0.04% in weight [1]. Instead, the amount of carbon content up to the limit of 0.4% in weight leads to increment in the yield and ultimate tensile strength at high temperatures, and in a reduction of the elongation. Interstitial free (IF) steels have no interstitial solute atoms to strain the solid iron lattice, resulting in very soft steel. IF steels have interstitial free body-centered cubic ferrite matrix, and contain carbon in the range 40 ppm to 70 ppm and nitrogen in the interval 30 ppm to 50 ppm **[12]**. The lack of interstitial atoms in the atomic structure enables IF steel to have extremely high ductility, ideal for deep-drawn products. In fact, IF steels are sometimes called extra deep drawing steels (EDDS). They have relatively low strength, although they are sometimes strengthened by the reintroduction of nitrogen or other elements, but high work hardening rates and excellent formability. These steels have a yield strength of about 145 MPa **[13]**. An improvement in those mechanical properties could be achieved by adding to steel manganese, phosphorus, silicon, and niobium, or titanium. However, manganese and phosphorus are the most common elements added to enhance the mechanical behaviour of the steel, so that it acquires the name of interstitial free high strength steel (IFHS), with yield strength that could reach over 300 MPa, and ultimate tensile strength that could go up to more than 400 MPa [12].

Against, these elements reduce formability and deep drawability. IF steels made using only titanium are very common, and are used to obtain the best mechanical properties for deep drawing operations. There are case in which titanium is coupled with niobium, to stabilize the structure. Some advantages of interstitial free steel include superior stamping, forming, and drawing performance, the ability to create more complex parts, the age hardening resistance, and the improved coating adhesion for galvanized products. The main disadvantage of interstitial free steel is that it can be very soft, resulting in shearing and punching difficulties. Those steels are used for automotive bodies and components, such as longitudinal beams, cross members, B-pillars, wheel arches, particularly with nitrogen as alloying element which increases the strength.

1.3.2 High Strength Low Alloy (HSLA) steels

High strength low alloy steels signed history in the automotive materials. They were introduced when there was the biggest effort to reduce the weight of vehicles to save fuel consumption. In the same time, other requirements had to be respected, such as reduction of CO_2 emissions, improved crash resistance, better material formability, weldability, and superior aesthetic quality and maintainability. To answer to those requests, HSLA steels started to be implemented in underbody components, suspension arms, cross-member tunnels and longitudinal beams. Some variants of HSLA steels are also present in wheels **[14]**. These steels offer good fatigue, torsional rigidity, and impact strength, and they are also more resistant to corrosion than carbon steels. High strength low alloy steels have a maximum carbon content of 0.15% in weight, silicon content up to 0.6%, manganese up to 1.7%. Other alloying elements include aluminium, not less than 0.015% in weight, niobium up to 0.1%, and silicon and phosphorus for maximum value less than 1% in weight **[15]**. This has led to unprecedented steel innovation to produce alloys with high strength and good cold formability. Particular HSLA steels can have a yield strength superior to 700 MPa, thanks to the addition of molybdenum. This element promotes the formation of bainitic microstructures that have higher strength than ferrite-pearlite microstructures. These bainitic steels are particularly interesting for structural reinforcement parts, wheels, chassis parts, and truck frames. The synergetic interaction of molybdenum with microalloying elements like niobium and titanium has also led to the development of ultrahigh-strength ferritic steels. The strength in these steels is gained by massive precipitation hardening. More in detail, molybdenum delays the precipitation of microalloying elements during thermomechanical rolling, retards the recrystallization during hot rolling, retards the transformation from austenite to ferrite, leading to finer grain size, and prevents coarsening of fine niobium and titanium carbides particles precipitated in ferrite. However, the addition of alloying elements is not the only action that allow to improve the mechanical properties. To control them, HSLA steels are subjected to rolling processes to induce deformations at high temperatures, which in turn will lead to substantial strengthening in the microstructure when steel is cooled.

There are many different grades of HSLA steel available because of the variety alloying element combinations that can be used. The chemical composition and grade should be dependent on the intended application of the HSLA steel.

1.3.3 Hot forming steels

Hot forming, also known also as hot stamping or press hardening, is a process which consists of heating the steel above the recrystallization temperature (that lie in the range of 500 °C to 600 °C, depending on the specific steel used) to soften it. In fact, at that temperature, new grains are produced, and the hardness of the material decreases. Hot forming includes processes like forging, hot rolling, and extrusion. This process is particularly suitable for components that must withstand high loads, such as cylinders, crankshafts, connecting rods, and gears.

Hot forming process can be executed directly or indirectly, as depicted in **Figure 1.13** **[16]**. In the direct process the unformed steel blank is heated in a furnace, formed t hot temperature, and then quenched in a die. In the indirect process is firstly formed and trimmed at cold temperatures, then is heated in the furnace and quenched in a die. A typical hot stamping line consists in a feeding zone, a furnace, a material handling system (which is automatized in mass production to reduce at most the transfer times), a press with a die set (hydraulic press is typically used to obtain complex geometries), a trimming/piercing system, and an unloading area. Typical steels which are hot formed are the C-Mn-B steels, and the most common one is the 22MnB5. The 22MnB5 steel is characterized by a maximum carbon content of 0.25% in weight, manganese in 1.35% in weight, and boron in 0.004% in weight **[17]**. Higher amounts of manganese lead to a reduction of toughness and to higher probability of cracks formation. The ultimate tensile strength can reach values up to 1500 MPa [17].

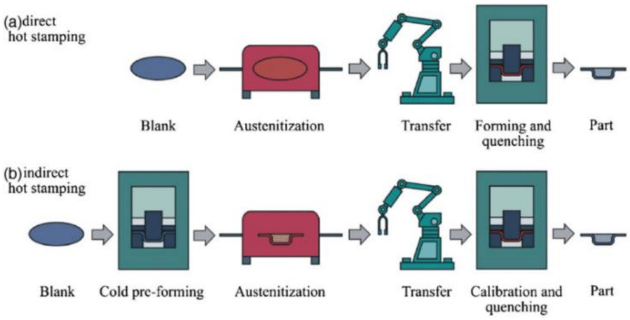

Figure 1.13: Direct and indirect hot stamping processes

The 22MnB5 is also known as Usibor®1500. However, varying the composition of the alloying elements it is possible to obtain a different combination of mechanical properties for Manganese-Boron hot formed steels, as evidenced in **Table 1** [17] and **Table 2** [17].

Steel	**B**	**C**	**Cr**	**Mn**	**P**	**S**	**Si**	**Ti**
20MnB5	0.003	0.18	0.30	1.25	0.020	0.007	0.35	0.030
22MnB5	0.003	0.25	0.18	1.25	0.020	0.007	0.25	0.026
27MnCrB5	0.003	0.27	0.34	1.25	0.020	0.005	0.27	0.033
30MnB5	0.003	0.30	0.15	1.30	0.020	0.007	0.27	0.030
34MnB5	0.003	0.35	0.17	1.30	0.020	0.005	0.25	0.035
40MnB5	0.003	0.40	0.47	1.25	0.020	0.005	0.25	0.040

Table 1: Chemical composition of Manganese-Boron steels.
The values are referred to the average percentage in weight.

For automotive applications, the aim of hot formed steels is to improve the crashworthiness and to save weight. The reduction in weight can be achieved by adding more carbon particles, but this action leads, as said before, to a reduction of toughness and so to eventual bigger mechanical problems. For this reason, 22MnB5 is the preferred steel.

Steel	**As delivered**		**Quenched**	
	YS	**UTS**	**YS**	**UTS**
20MnB5	530	650	967	1354
22MnB5	550	700	1010	1478
27MnCrB5	570	760	1097	1611
30MnB5	600	760	1135	1740
34MnB5	620	820	1225	1919
40MnB5	780	950	1378	2040

Table 2: Mechanical properties of Manganese-Boron steels.
YS = Yield Strength, **UTS** = Ultimate Tensile Strength
All the values are in Megapascal [MPa]

As advantages, hot forming steels have a low springback, allow to obtain complex shapes, have a good dimensional stability, guarantee a weight reduction, can be formed with application of low forces, are suitable for all the types of quality required, and have uniform mechanical properties. Hot forming steels are particularly well suited for the entire range of structural parts which require anti-intrusion resistance in a crash, and so are adopted for front and rear bumper beams, door reinforcements, A and B pillars reinforcements, floor and roof reinforcements, and roof and dash panel crossmembers **[18]**.

1.3.4 Advanced High Strength Steels (AHSS)

Nowadays, new innovations occurred in materials science and more performant steels have been obtained, such as the Advanced High Strength Steels (AHSS) and Ultra High Advanced Strength Steels (UHSS).

The first generation of AHSS includes dual-phase (DP), complex-phase (CP), martensitic (MS) and regular transformation-induced plasticity (TRIP) steels. This first generation has more formability than HSLA steels at the same strength level. This is due to its multiphase microstructure, which contains ferritic and martensitic phases for a balance between formability and strength. The unique microstructure of these steels is created by special heat treatments. The biggest limiting factor of the first generation of Advanced High Strength Steels is their low formability. The second generation of AHSS includes a new generation of transformation-induced plasticity (TRIP), hot-formed (HF), and twinning-induced plasticity (TWIP) steels. Both the first and second generation of Advanced High Strength Steels are designed to meet the functional performance demands of certain components in the automotive industry. For TWIP steels, the formability property of these steels is way higher than that of the first generation, but their higher cost limits their use. Finally, a new class is under development, the one called third generation. The third generation of AHSS allows to obtain the best results in terms of tensile strength and ductility, without the cost problems associated to the second generation. This last class guarantees a very high elongation, with an elasticity modulus that could achieve the highest value, and a consistent weight reduction in the car body parts. Typical car body applications are the structural safety components. The front and rear rails and the safety cage, including A pillar, B pillar, roof rail, sill, and hinge pillar, need to be formed accurately into complex shapes to maintain vehicle stiffness, resist high vehicle loading forces, and absorb impact energy in a crash situation. **Figure 1.14** summarizes the main mechanical characteristics of the main automotive steels.

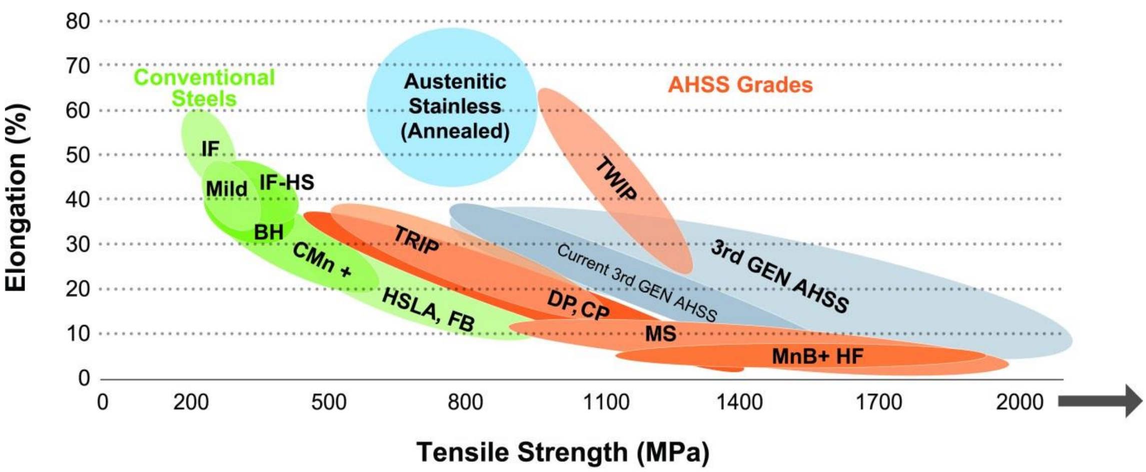

Figure 1.14: Classification of the main automotive steels **[19]**

1.3.5 Dual-phase steels

Dual-phase steels are one of the advanced high strength steels used in the automotive industry. They are characterized by a very high strain hardening and hardenability, and by a good formability. These steels feature tensile strength 450 MPa to 1350 MPa **[20]**. Dual-phase steels are produced by controlled cooling from the austenite phase (in hot-rolled products) or from the two-phase ferrite plus austenite phase (for continuously annealed cold-rolled and hot-dip coated products) to transform some austenite to ferrite before a rapid cooling transforms the remaining austenite to martensite. Due to the production process, a small number of other phases, like bainite and retained austenite, may be present.

Dual-phase steels have a ferritic-martensitic structure. Soft ferrite is the primary constituent, present for about 90% in weight, which surrounds the martensite areas, which is the secondary phase (see **Figure 1.15**). The white areas are made of ferrite, the dark ones are made of martensite. The ferrite phase is normally continuous, and gives the steel a good level of ductility.

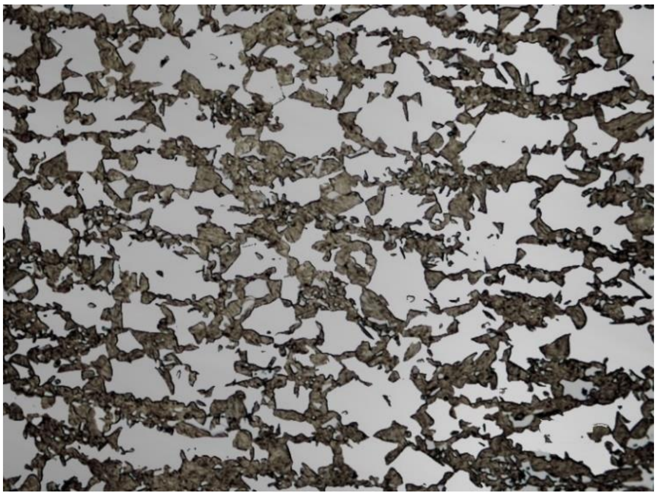

Figure 1.15: Microstructure of a dual-phase steel **[21]**

It is understandable that the overall mechanical properties of dual-phase steels depend on the characteristics of its microstructure, such as volume fraction, grain size and aspect ratio, and carbon content. Increasing the volume fraction of martensite generally increases the strength of the steel. The volume fraction of austenite reached to give rise to dual-phase steels is influenced primarily by silicon and aluminium. Their presence reduces the amount of austenite volume fraction with temperature. Also, austenite fraction is reduced by a decrement of the carbon content at the eutectoid composition. To solve the problem, manganese is added to steel, so that austenite formation is favoured and stabilized. However, the element that guarantees the strongest stabilizing effect for the austenite is molybdenum. This element facilitates the transformation from austenite to martensite at the lowest cooling rates. Furthermore, molybdenum is able to shift the ferritic transformation to lower cooling temperatures, lowering also the temperature at which the bainitic transformation occurs. In this way, the bainite at the end of the transformation process is noticeably reduced. Another alloying element that could replace molybdenum is chromium. The alloying elements have direct effects also on the temperature at which the transformation into martensite takes place. In particular, the highest effects are given by carbon, manganese, chromium, and silicon. Carbon, usually present for 0.20% in weight, acts as an austenite stabilizer, strengthens the martensite, and determines the phase distribution. Manganese, used between 1.5% and 3%, also stabilizes the austenite, strengthens the ferrite solid solution, and retards ferrite formation. Silicon promotes ferritic transformation, while chromium and molybdenum, used up to 0.4% in weight, can retard pearlite and bainite formations. Additionally, microalloying elements, such as vanadium or niobium, can be used as precipitation reinforcement, and to refine the microstructure.

Hot-rolled dual-phase steels are particularly suitable for weight-saving production of wheels, chassis parts, profiles, and body reinforcements. Cold-rolled dual-phase steels are suitable for both complex structural parts, such as side members and cross members, as well as stretch-formed exterior parts with special requirements in terms of buckling strength (doors, roofs, trunk lids). The high yield point and high tensile strength lead to high fatigue limits. Fine and dispersed distribution of martensite and ferrite avoids any adverse effect on the fatigue limit, on account of the strength difference between the structural components of ferrite and martensite. Higher strength values due to work hardening as an effect of deformation, contribute to the improvement of the material behaviour. The high level of strength and the high strain-hardening capacity make dual-phase steels ideal for crash energy absorbing components.

1.3.6 TRIP steels

TRIP steels are another type of Advanced High Strength Steels (AHSS), and the acronym stands for TRansformation Induced Plasticity, referring to the strain hardening effect that occur during the plastic deformation, while austenite is transforming into martensite. The microstructure of TRIP steels consists in a ferritic (~60% in volume) and bainitic (~25% in volume) matrix, also with the presence of retained austenite (~15% in volume) **[22]**. To obtain smaller volumes of retained austenite, carbon is added to the steel, in order so to reduce the temperature at which the martensitic transformation begins.

TRIP steels are characterized by a low quantity of alloying elements. Usually, the total amount of all the added elements do not exceed the 4% in weight. The main alloying elements are carbon, manganese, and silicon. Carbon has a strong solid solution strengthening effect, and also lower amounts of carbon particles are able to increase the tensile strength considerably. However, carbon contents superior to 0.2% in weight lead to welding issues. Manganese increases the hardenability of the steel, and amounts in the range 1.5% to 2% in weight contribute to slowing down the pearlite reaction, promoting the formation of acicular ferrite or bainite, leading so to improvements in the strength. In addition, manganese reduces the temperature at which the martensite transformation occurs, favouring the stabilization of austenite. Manganese additions superior to 2.5% in weight are to avoid, since will increase the brittleness of the structure. Silicon stabilizes the ferritic and the austenitic phases. It is also insoluble in cementite, and so it prevents cementite formation **[22]**. Aluminium addition is used to replace the silicon addition. Aluminium, like silicon, is a ferrite stabilizer, and it is also insoluble in cementite. Unlike silicon, aluminium increases the driving force of austenite-bainite transformation. However, the main limiting factor of aluminium is that is not a good strengthening element, so the desired mechanical properties can be reached if aluminium is replaced by silicon. Niobium and titanium are added to increase the strength of the steel by grain refinement and precipitation strengthening.

TRIP Steels can be produced as hot-rolled, cold-rolled, or hot dip galvanized, with a strength range from 400 MPa to 600 MPa **[23]**. TRIP steels have higher ductility with respect to dual-phase steels, and this is why their main use in vehicles is for crash absorbing components. The stability and the amount of retained austenite in the TRIP steels are of utmost importance to achieve this high ductility level, which ensures that a high amount of energy is absorbed in the event of a crash. In the automotive sector, TRIP steels are employed in the construction of frame rails and reinforcement parts, as well as lightweight structural components **[24]**.

1.3.7 Quenching and Partitioning (QP) steels

Quenching and Partitioning (QP) steels are one of the most attractive type of steels for the third generation of Advanced High Strength Steels. Usual steels of this type are the C-Si-Mn and the C-Si-Mn-Al steels. The name of this class of steels derived from the thermal process that steels undergo. The quenching and partitioning process consists in heating the steel sheets above the austenitic temperature (i.e. above 800 °C), maintaining that value for a certain time in order to let the material to acquire the austenitic structure. When the heating process is completed, the steel is rapidly cooled according to the *quenching* operation. Doing so, a fraction of austenite is transformed in primary martensite (α'_p). After that, the material is heated again, but a temperature that is just above the one at which the transformation into martensite occurs (M_S), so in the range 450 °C to 500 °C, and maintained at that value in time. From now on, the *partitioning* process occurs. With that thermal process, the austenite is stabilized, thanks to the fact that the carbon particles accumulate in the grains. To obtain other martensite, called secondary martensite (α'_s), and so to increase the martensite content in the entire steel, another quenching treatment is done. Now, the structure of the steel is made by martensite, in greater amount, and retained austenite. This retained austenite is essential to increase the malleability and ductility of the steel. Retained austenite allow the steel to be worked with different mechanical processes, and this would be not possible is the structure were made completely in martensite. **Figure 1.16 [25]** summarizes the quenching and partitioning thermal process. In order to achieve the most effective partitioning and associated austenite retention by carbon partitioning from martensite into the remaining austenite, competing reactions must be limited. Sufficient retardation of cementite precipitation can be achieved by alloying additions of silicon, aluminium, and/or phosphorus in austempered bainitic and quenched and partitioned martensitic microstructures. Silicon is used to stabilize the austenite phase during continuous annealing and at room temperature, because silicon significantly increases the carbon activity in both ferrite and austenite and decreases carbon solubility in ferrite. Manganese is a very wide used alloying element for automotive steels. Automotive industry uses steels with manganese content that varies between 7% and 10% in weight, concentrations that characterized the medium manganese content steels. Manganese increases ductility and raises the ultimate tensile strength.

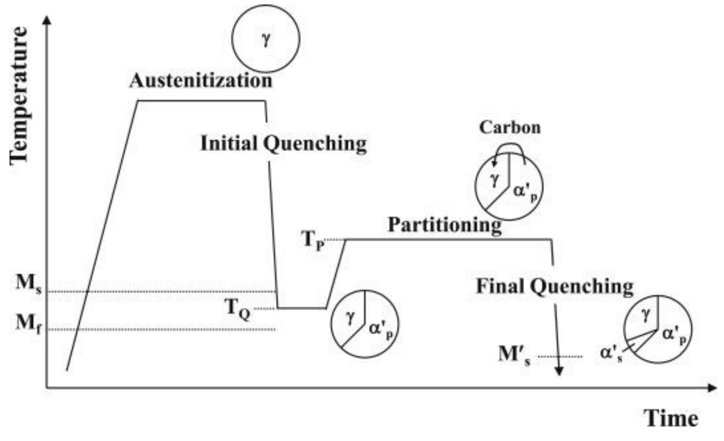

Figure 1.16: Schematization of the quenching and partitioning process

Also, manganese helps in stabilizing the austenitic phase. The carbon content in current QP steels is limited from 0.15% to 0.30% in weight due to weldability concerns.

The work-hardening rates of QP steels are substantially higher than for conventional High Strength Steels (HSS), providing significant stretch forming capability. Compared to most other HSS with the same tensile strength, QP steels exhibit much higher formability; hence, they are particularly well suited for automotive structural and safety parts, such as cross members, longitudinal beams, B-pillar reinforcements, sills, and bumper reinforcements, which cannot be cold formed using conventional HSS with similar strength levels. **Figure 1.17 [26]** provides a view of the microstructure of a QP steel.

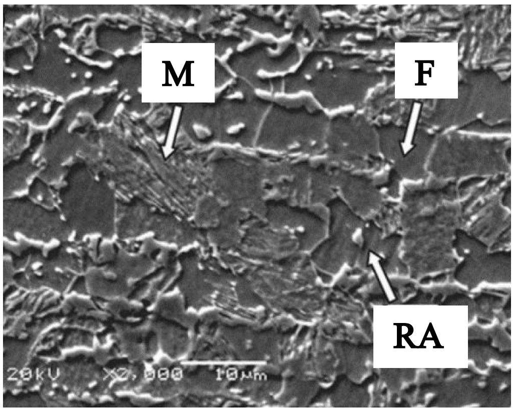

Figure 1.17: Microscopic view of a QP steel microstructure
M = Martensite; **RA** = Retained Austenite; **F** = Ferrite
Ferrite is present only in case of partial austenitization.

Chapter 2 – Plastic and damage behaviour models

2.1 True curve estimations

The true curve of the material can be estimated by different mathematical models. These estimations are used to predict the material’s behaviour after the onset of the necking condition. The estimated curves differ from each other and from the true curve due to the fact that different parameters are taken into account between them. Some models are more precise, others are more restricted, but the aim is to predict the structural behaviour. In this project, the models considered are the Hollomon law, the Ludwik estimation, the El Magd and Swift & Voce estimation, the MLR method and the Bridgman estimating model. We will see that all these models cannot approximate perfectly the elastic behaviour of the steel; however, what is important is to have a smooth transition after the necking point of the experimental true curve. To reduce at its minimum value the error between the estimated curve and the experimental curve, an automatized Excel file has been developed.

2.1.1 Hollomon law

The Hollomon model, or Hollomon law, is based on an exponential law, the power law, where the true stress and the true strain are correlated with a strength coefficient **K** and a strain hardening exponent **n**.

$$\sigma_T = K\varepsilon_T^n \tag{27}$$

Both the parameters K and n are determined in the elastic region of the true stress-true strain curve. The Hollomon law has been used for value of strains up to 1, that corresponds to 100% of deformation. Very important for the virtual simulations is the necking constraint. In other words, it is necessary to ensure that the ratio between the difference in two consecutive loads and the difference in two consecutive value of strains has to be at least very similar, to the value of stress registered at the onset of the necking. This constraint has some negative effects on the approximation of the curve, but ensures that the software starts the necking at the exact point. The Hollomon model produces a continuous monotonically increasing curve which is prolonged up to the value of strain equal to 1. Using this model, it has been assumed that the starting point of this model coincides with the beginning of the plastic region. In the Hollomon hardening model expression, the strain-hardening exponent measures the ability of a metal to strain-harden, larger magnitudes indicate larger degrees of strain hardening. For most metals, the strain-hardening exponent falls between 0.10-0.50 **[28]**; however, perfectly elastic plastic-solids have a strain-hardening exponent of zero. The strain-hardening exponent and the strength coefficient are both determined from the logarithm of the true stress versus the logarithm of the true strain in the region of uniform elongation.

The validity of the Hollomon estimating model is confirmed by the studies carried by Mansoo et al. **[29]** on a dog bone specimen similar to the one analysed in this thesis. By using Hollomon law, the necking should occur when the true strain reaches the hardening exponent **n**, according to the Considère criterion **[30]**. The Hollomon law has been used before the necking condition, until the point at which necking begins. The true stress-strain curve has been obtained with the incompressibility assumption, according to which the plastic strains do not involve any volume change **[31]**. The plastic behaviour estimation with the Hollomon model is determined with a Finite Element Method analysis on AFDEX2D software. In order to perform an accurate analysis, only a local area near the central section of the specimen has been meshed. In **Figure 2.1** is possible to see the engineering curve and the true curve obtained from the tests.

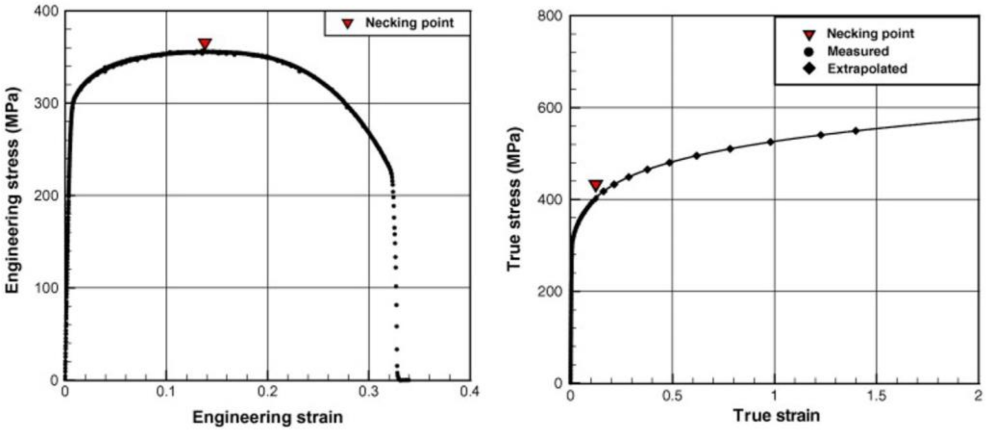

Figure 2.1: Engineering curve and true curve used for FEM test [29]

The error between the predictions and the experiments increases as the elongation increases after necking, because the reference stress–strain curve underestimates the strain-hardening effect, causing the necked region's elongation to increase, compared to that of the other region. Due to this limitation, the Hollomon model is not used to predict the whole tensile test, but only to estimate with a satisfactory accuracy the necking point. The effective deformation in the tensile tests is not uniform, and the major deformation region moves continuously, usually in a longitudinal direction. In the major deformation region, the structural rigidity is enhanced, because the strain-hardening effect due to plastic deformation is stronger, relative to the area-reduction effect before necking. Thus, the major deformation region moves to the other, less strain-hardened, region. When the area-reduction effect becomes stronger than the strain-hardening effect during the tensile test, the situation is reversed, which means that the major deformation region becomes weak and the additional deformation leads to necking. However, the necking position on the tensile test specimen cannot be predicted, because the major deformation region moves from place to place, even though the elongation at the necking point can be exactly predicted. This is because necking takes place when the strain-hardening effect becomes weaker than the area-reduction effect on structural rigidity in the major deformation region.

2.1.2 Ludwik model

The Ludwik model is basically a Hollomon law model with value of stresses translated alongside the stress axis of a determined quantity A:

$$\sigma_T = A + K\varepsilon_T^n \qquad \textbf{[32]}$$

The validity of the model has been proposed by Gupta et al. [32], where a finite element method analysis performed on Abaqus has been carried on to test the Ludwik model. The extrapolation method has been used to evaluate the post-necking behaviour due to the fact that this phenomenon generates a non-uniform deformation. The Ludwik model tests have been done on a dog bone aluminium specimen with gauge length of 40 mm and cross section of 10 mm width. Experimental value of the true stress at necking is 622.9302 MPa for Al2014-T6 alloy under quasi-static loading (0.4 mm/s) which is used in numerical simulation. Here, the velocity is taken as 0.4 mm/ s to obtain the strain rate of 0.01 s^{-1} as the gauge length of the specimen is 40 mm. To calibrate the model in order to obtain the most precise results, i.e. the best stress concentration result, the interested region on the specimen has been meshed in different ways, obtaining that the size 0.1 of the gauge section provides the best accuracy. **Figure 2.2** [32] compares the different meshing options. The curve for large deformations is obtained with Abaqus software.

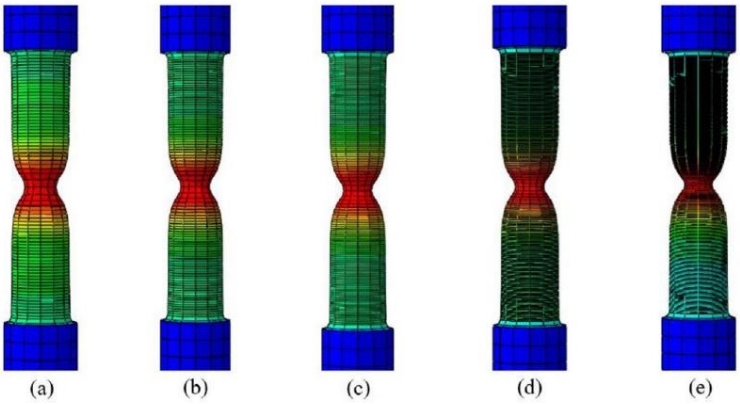

Figure 2.2: Simulated equivalent stress contour using different mesh sizes at gauge section (a) 0.5 (b) 0.4 (c) 0.3 (d) 0.2 (e) 0.1

The material parameters of the different models are estimated by least square regression method based on experimental flow curve with minimizing error, in particular A=57.445, K=858.92, and n=0.17911. It is observed that the predicted results of the Ludwik model fitted quite well the experimental results in the pre-necking zone, while the precision consistently reduces after the necking occurrence. The accuracy is already decreasing near the necking region, where you can clearly see (**Figure 2.3** [32]) the data divergence between the experimental curve and the estimated one.

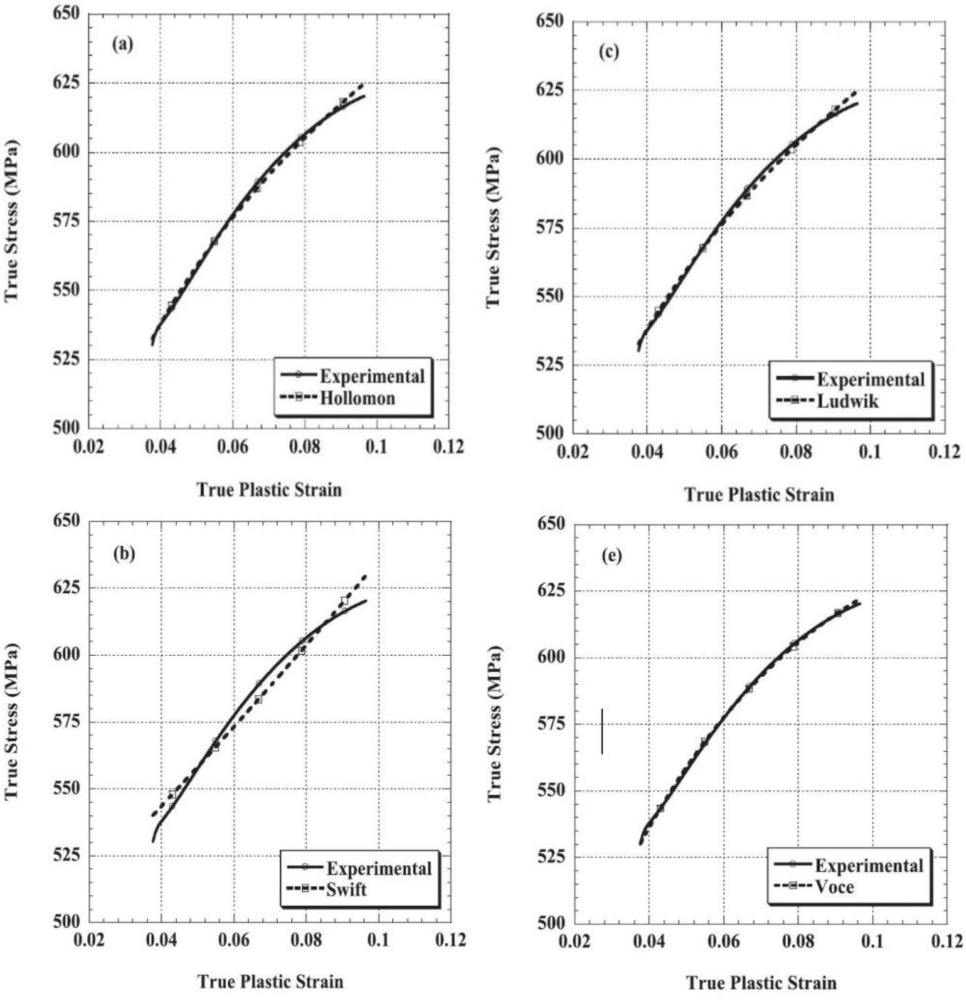

Figure 2.3: Ludwik and other estimated curves

All the models fit quite well the experimental curve. In particular, the experimental value of true stress at necking is 622.93 MPa; whereas the true stress estimated from simulation is 622.91 MPa at necking. Instead, the true stress found at necking for Hollomon, Ludwik, Swift, and Voce models are 630.9, 631.3, 636.5, and 626.3 MPa respectively. We can see how the Hollomon model and the Ludwik model originates two curves which are very similar between them. For large values of strain, i.e. for large deformations, the Ludwik estimating curve and the Hollomon curve provides the closest results to the experimental ones, while in the pre-necking phase the best behaviour is given by the Voce estimating model, while the Swift curve overestimates the flow curve. In this project, a combination of the Swift and Voce models is used. Finally, Gupta et al. provided that Numerical simulation on stress–strain behaviour of the alloy in Abaqus displays close agreement to the experimental curve, that all the models fit well the experimental curve although the Voce estimation gives the best accuracy, while the Hollomon and Ludwik curves provide the best behaviour description in the post-necking region.

2.1.3 El Magd estimation

The El Magd estimation curve can be determined by implementing the following equation:

$$\sigma = A + \beta_1 \varepsilon + K[1 - \exp(-\beta_2 \varepsilon)] \qquad \textbf{[33]}$$

The variables A, β_1, β_2, K are experimentally determined. However, the El Magd approximation method is not so much precise, since for larger value of strains the curve tends to be linear and stresses are generally too much higher with respect to the other curve estimation methodologies. In other words, the El Magd model provides the highest linear work hardening rate at high strains. This model is a quasi-static model, where the flow stress is a function of plastic strain. Şener et al. [33] proved the accuracy of the El Magd model on two types of steels, austenitic and ferritic. Tensile tests were carried out for determination of flow curves of Austenitic 304 and Ferritic 430 stainless steel sheets. The specimens were prepared according to ASTM E8M standard specification, by laser cutting. The thicknesses of the 304 and 430 stainless steel sheets were 0.8 and 0.7 mm, respectively. 50 kN load capacity universal tensile testing machine was used. The experiments were conducted at constant strain rate in all directions. The tensile test measurements were made via Digital Image Correlation technique, and the engineering curve has been drawn. The elasticity modulus, E, was calculated by dividing the tensile stress by the strain in the elastic portion, i.e. linear region, of the stress-strain curve, while the yield stress was obtained by means of an offset to 0.2% of strain, related to the straight part of the elastic behaviour region. The parameters for such models are identified from experimentally determined flow curves of materials by curve fitting techniques. Nonlinear least square regression method and Levenberg-Marquardt algorithm **[34]** were used. In **Figure 2.4 and 2.5** [33] it is possible to see approximations obtained with El Magd and other models on Austenitic and Ferritic steels.

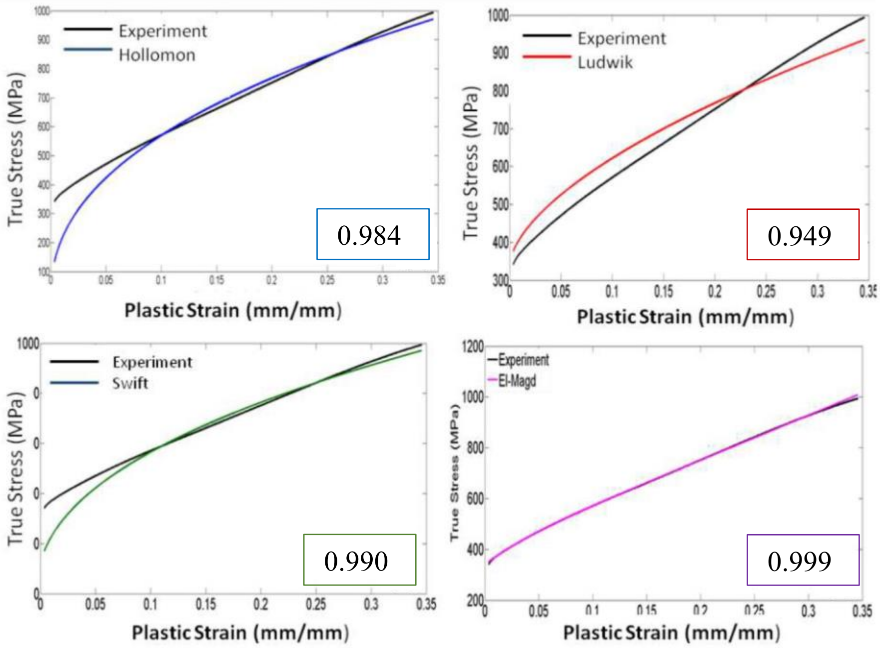

Figure 2.4: Predicted flow curves for Austenitic 304 steel

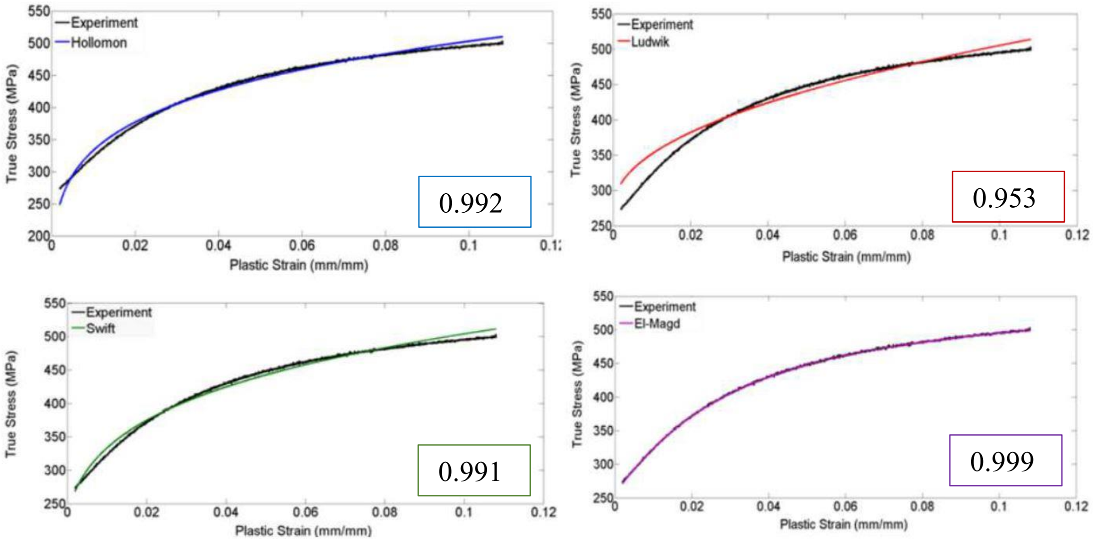

Figure 2.5: Predicted flow curves for Ferritic 430 steel

The validity and precision of the estimated curves has been evaluated by a nonlinear regression parameter (R^2). As said at the beginning, this parameter acts as a variable for the minimization of the sum of squared residuals. Indeed, R^2 is the square of the correlation between the experimental values and the estimated ones, and higher is its value and better is the approximation provided by the model considered. Şener et al. [33] compares the models based on this variable, proving important differences. In **Figure 2.4** and **Figure 2.5**, on the bottom right of each model diagram, you can read the value of the nonlinear regression parameter. The El Magd model provides the highest, and hence the best, value of nonlinear regression parameter, that mean that the predicted curve has a very good fitting. In contrast, the Ludwik estimation provides the worst curve fitting. Compared to the results obtained by Gupta et al. [32], the Ludwik estimation is even worse, proof that this estimating model is not so suitable in the pre-necking behaviour description with respect to the other estimating models.

2.1.4 Swift & Voce estimation

The Swift & Voce methodology combines the results of the characteristic polynomials of Swift and Voce functions. In particular, the characteristic equations of the two models are the following **[35]**:

$$Swift \qquad \sigma = K(\varepsilon_0 + \varepsilon_t)^n$$

$$Voce \qquad \sigma = k_0 + Q(1 - e^{-\beta\varepsilon_t})$$

The introduced variables **K**, $\boldsymbol{\varepsilon_0}$, **n**, $\mathbf{k_0}$, **Q** and **β**, are adjustable parameters determined by fitting the experimental data. The Swift formulation is similar to the Hollomon model previously described. It can be achieved by moving the stress axis of the Hollomon model along the positive strain axis through a distance of ε_0. Therefore, the Swift model is more suitable when prior cold work is involved, with ε_0 representing the amount of prestrain. The Voce concept is adopted when the flow stress of some material may display non-linearly with the increment of the equivalent plastic strain first, saturated into a constant value with further plastic deformation. The combination of both the effects is represented by a weighted sum between the Swift stress estimation and the Voce stress estimation.

$$Swift\,\&\,Voce \qquad \sigma = \alpha\,[K(\varepsilon_0 + \varepsilon_t)^n] + (1 - \alpha)\,[k_0 + Q(1 - e^{-\beta\varepsilon_t})]$$

The parameter **α** is simply a coefficient arbitrarily determined in order to find the most proper value that allows to approximate, with a satisfactory precision, the true curve obtained from the experimental data. The reference for this type of model is provided by Kim H. et al. [35] which uses the Swift and Voce models, separately, to study the plastic behaviour of Dual Phase (DP780) and TRIP (TRIP780) steels, materials used in the Automotive industry. The tensile test specimens are obtained from 1.2 mm steel sheet, and the measurements are taken by the Digital Image Correlation technique and extensometers placed over a gauge length of 50 mm. In order to validate the proposed identification procedure, virtual measurements were computed using the FE software Abaqus. The constitutive parameters of the models are obtained from the Virtual Fields Method (VFM) [35]:

$$-\int_v \left[\int_0^t \frac{d\sigma_{ij}}{dt}dt\right]\varepsilon_{ij}^* dV + \int_{\partial V} T_i u_i^* dS = 0$$

The first term is the internal virtual work, the second one is the external virtual work. The Virtual Fields Method is an inverse computation technique based on the Principle of Virtual Work (PVW), used to estimate mechanical properties of materials from full-field strain measurements, and describes the global equilibrium of the solid. dσ/dt is the stress rate, V the volume of the specimen, ∂V the boundary of the specimen where the tractions are applied, T the surface tractions acting on ∂V, u^* the virtual displacement field, and ε^* is the virtual strain field derived from u^*. The parameters identified using the VFM were compared to the reference values, which were the input of the Finite Element simulations. In **Figure 2.6** [35] it is possible to see the curve estimated by the two laws, with respect to the experimental curve.

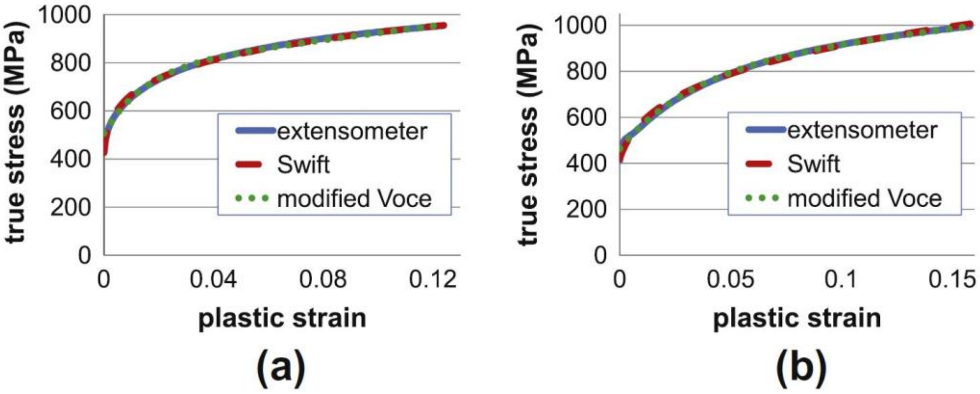

Figure 2.6: True stress-strain curve for DP780 (a) and TRIP780 (b)

The pure Voce model is characterized by a high discrepancy with the experimental values, and for this reason it is used a modified version of it, simply called modified Voce. It is similar to the pure Voce formulation, but slightly changed [35]:

$$\sigma_s = Y_0 + R_0\varepsilon_p + R_{inf}\left(1 - exp\left(-b\varepsilon_p\right)\right)$$

Y_0, R_0, ε_p, R_{inf} and b are all parameters to be determined. From the graphs we can see how these models, although different, are very similar, and provide curves which are valid and very accurate. In this project, a combination of Swift and Voce model is used, to exploit the benefits of both the plastic behaviour models. The merge allows to obtain a better approximation of the experimental curve, reducing the errors also in case of large strains.

2.1.5 MLR estimation

The true curve obtained characterizes correctly the material only in the pre-necking phase of the straining; during the post-necking phase this curve differs substantially from the real material curve because, since the necking phenomenon arises, the stress state departs gradually from uniaxiality and from uniformity across the neck section. In other words, the true-stress (current ratio between load and resisting area) is perfectly coincident with the local axial stress and with the local von Mises stress on the neck centre, only until the necking initiates. On the contrary, under well-developed necking conditions, these three stresses differ substantially each other. The MLR technique aims at plotting a graphical trend of the ratio between the averaged and cross-section value of stresses, $\sigma_{eq,Avg}/\sigma_{z,Avg}$, as a function of the difference $\varepsilon_{eq}-\varepsilon_N$. In **Figure 2.7 [36]** there is the relation between the stress's ratio in relation with the strain's differential for different materials.

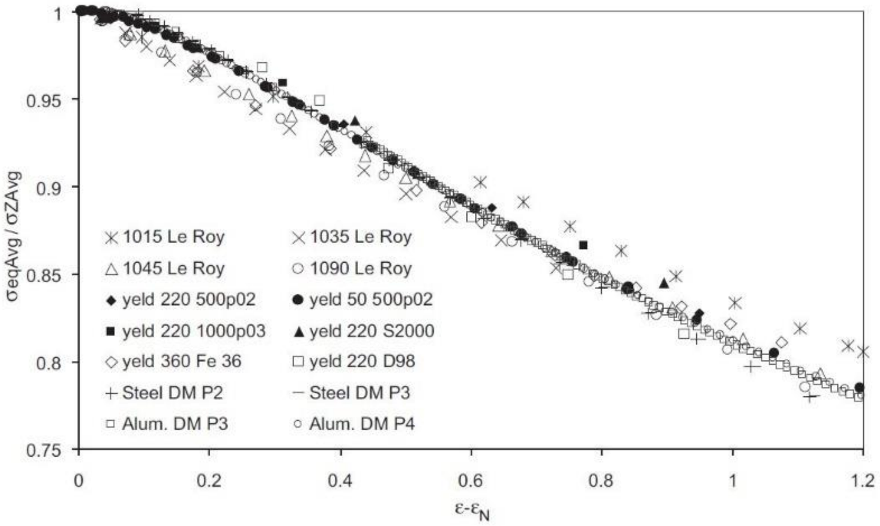

Figure 2.7: Evolution of the $\sigma_{eq,Avg}/\sigma_{z,Avg}$ ratio vs. reduced plastic strain

The trend of $\sigma_{eq,Avg}/\sigma_{z,Avg}$ can be approximated by the following relation [36]:

$$MLR(\varepsilon_{eq}-\varepsilon_N)=0.9969-0.6058(\varepsilon_{eq}-\varepsilon_N)^2+0.6317(\varepsilon_{eq}-\varepsilon_N)^3-0.2107(\varepsilon_{eq}-\varepsilon_N)^4$$

Notice that the MLR function is always equal to 1 in the pre-necking region, since the true stress coincides with the equivalent stress, and it is suitable for a variety of metals, not only steels. Considering the pre-necking phase, the MLR estimation model calculates the overall stress flow by means of the following expression **[37]**:

$$\sigma_{eq}=\begin{cases}K\varepsilon_{eq}^{n} & for\ (0<\varepsilon_{eq}\leq\varepsilon_N)\\ (S_0+S_1\varepsilon_{eq})*MLR_{\sigma}(\varepsilon_{eq}-\varepsilon_N) & for\ (\varepsilon_{eq}>\varepsilon_N)\end{cases}$$

The parameter S_1 is the value of the yield stress. Referring to the parameter S_0, notice that, for $\varepsilon_{eq} = \varepsilon_N$, the MLR function equals the approximated value of 1. This means that at the necking point, for continuity reasons, it must be verified that $K\varepsilon_{eq}^n = S_0 + S_1\varepsilon_{eq}$, from which it is easy to find the value of S_0 parameter. Similar to this model there is the Bridgman method, which is described in the following. Compared to Bridgman, which errors are in the range 5% – 13% **[38]**, the MLR methodology provides lower errors, in the range 3% - 5% [36] thanks to the fact that the MLR function requires less information with respect to the Bridgman method. In details, the MLR correction requires information on the true stress, while the Bridgman estimating model requires data on the specimen profile, radius of curvatures of its section and general dimensions of the cross section, information that leads to a complex evaluation of the true curve, with higher probabilities of errors and lack of precision. However, the Bridgman model, like for the MLR correction, is valid and reliable, and for this reason it is included in this project. The MLR estimations provided by Mirone [36] are done on three specimens of different steels, with length of 25 mm and cross section of 5 mm. The three different materials tested are Steel 1015, Steel 1045, and Steel 1090. To obtain the true curves, Finite element analyses have been performed by way of the MARC FE code, taking into account the typical non-linearities due to the material behaviour and the large displacement fields. **Figure 2.8** [36] shows the true curves obtained with the MLR correction compared to the engineering curves.

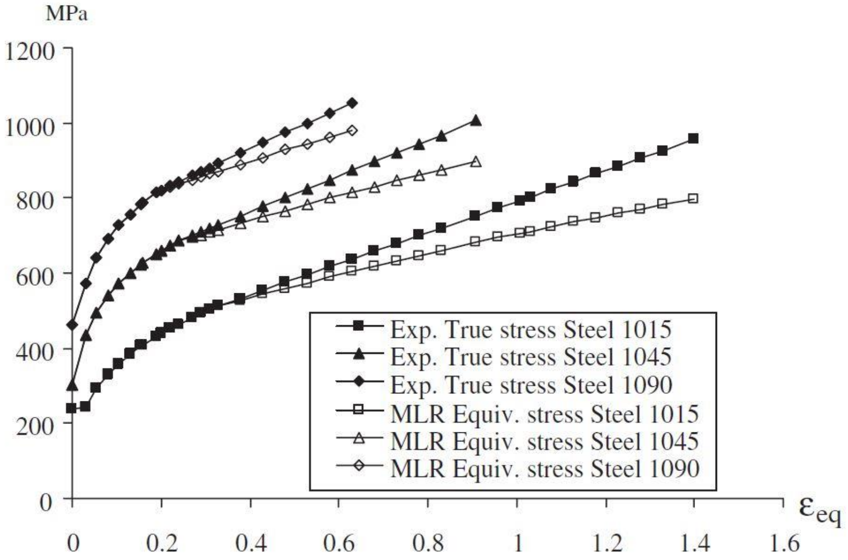

Figure 2.8: True curves of Steel 1015, Steel 1045, and Steel 1090

To improve the accuracy of damage predictions, the Rice and Tracey damage model has been used by [36] to monitor the stress flow by void growth. A detailed explanation of this damage model will be done further on in section 2.2. In addition, to have accurate measurements of the stress in the neck region of the specimen, the triaxiality factor (TF) is evaluated:

$$TF = \frac{\sigma_{z,Avg}}{\sigma_{eq,Avg}} - \frac{2}{3}$$

Figure 2.9 [36] shows the discrepancies between the values of the triaxiality factor obtained via Finite Element simulation, and the values of triaxiality obtained via MLR function.

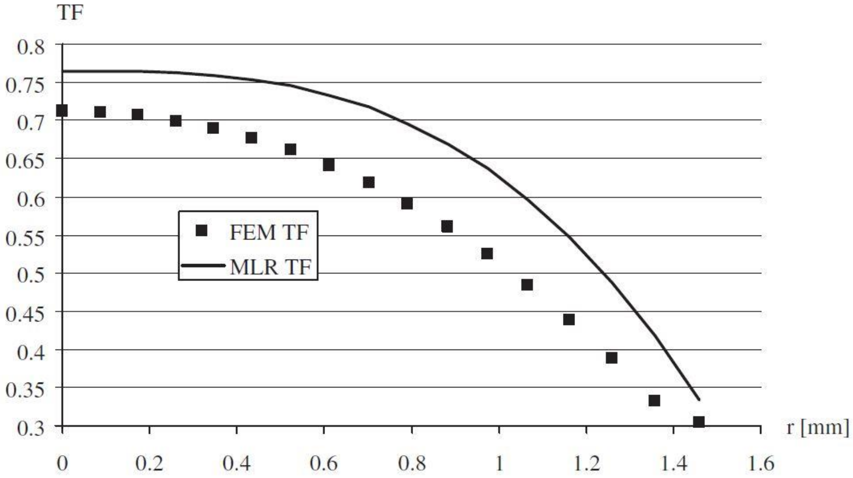

Figure 2.9: TF values from FEM and MLR function

The figure refers to the TF deviations of Steel 1015, which is the material that shows the biggest differences, with an error of about 10% in the neck centre region [36]. The reason of this divergence is probably due to the fact that the triaxiality factor is evaluated taking into account the average values of stresses and not the local ones. However, the errors are not so big, and its implementation in the Rice and Tracey model for sure improves the accuracy of the plastic behaviour estimation. The numerical results are in very good agreement with the experiments, exhibiting a maximum error lower than 3.5%, thus confirming that the adoption of the MLR method is well suitable for the post-necking stress– strain characterization of ductile materials.

2.1.6 Bridgman estimation

The Bridgman correction estimation model is similar to the MLR estimation method, although, as already said, more sensible to higher errors, but still a valid solution. Again, the Bridgman estimate is applied after the onset of the necking, while before this condition is still valid the power law relation. The Bridgman estimation model produces a continuous monotonically increasing curve which is prolonged up to the value of strain equal to 1. Using this model, it has been assumed that the starting point of this model coincides with the beginning of the plastic region. The determination of the stress by the Bridgman method is provided by the following equation [37]:

$$\sigma_{eq} = \begin{cases} K\varepsilon_{eq}^{n} & for\ (0 < \varepsilon_{eq} \leq \varepsilon_N) \\ B_0 + B_1\varepsilon_{eq} + B_2\varepsilon_{eq}^2 & for\ (\varepsilon_{eq} > \varepsilon_N) \end{cases}$$

The parameter B_1 is the yielding stress, the parameter B_2 is given by $B_2 = -B_1\varepsilon_{eq}$, and parameter B_0 is given by $B_0 = K\varepsilon_{eq}^{n} + B_2$, with $\varepsilon_{eq} = \varepsilon_N$.

La Rosa et al. [38] analysed the Bridgman methodology to test its validity and determine errors in the behaviour prediction after the onset of necking. The tests performed are on unnotched specimens of DP98, a variety of stainless steel, with length of 183.5 mm, curvature radius of 20 mm, and cross section width of 9 mm. By image acquisition and real test, the true curve has been obtained, and it is visible in **Figure 2.10** [38].

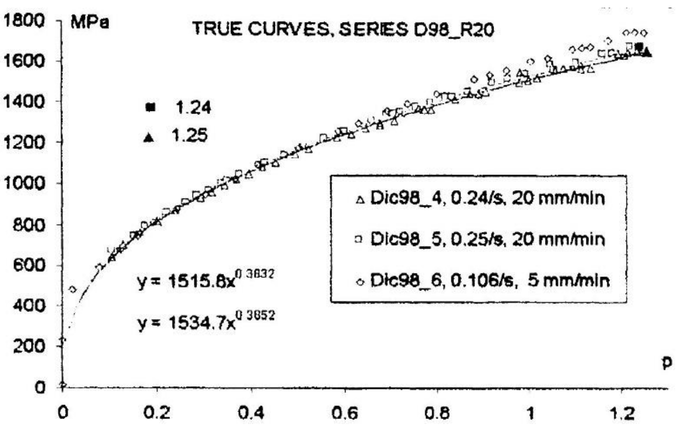

Figure 2.10: True curve for DP98 steel for different deformation velocities

The data points fall in a narrow range of interval, which means that the Bridgman solution provides a consistent evaluation. To verify that, another test on different specimens' geometry has been done. In **Figure 2.11** [38] there are the true curves obtained for the unnotched specimen, and for notch radius of 10 mm and 20 mm.

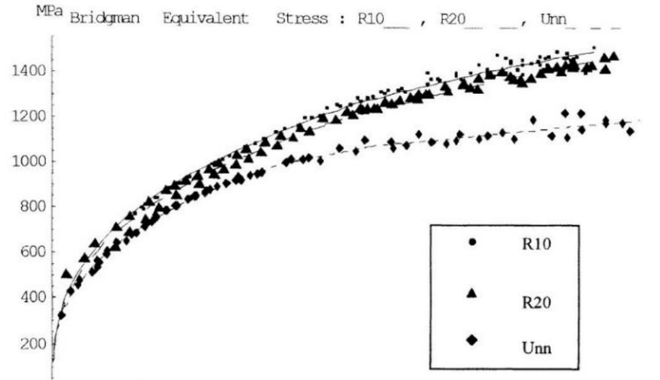

Figure 2.11: True and equivalent stresses vs equivalent plastic strain

From the figure it is clearly visible that the three curves are considerably different, meaning that the Bridgman estimating method highly depends on the geometry considered for the analysis. However, for the study carried by La Rosa et al, the curve related to the unnotched specimen has been chosen for the Finite Element simulations, making use of 6330 elements for the plastic strain analysis. The non-linear analysis, performed using MARC software, was conducted assuming constant dilatation, large displacement and finite strain plasticity, so that both geometric and material non-linearities were accounted for. True curves from FEM simulations are visible in **Figure 2.12** [38].

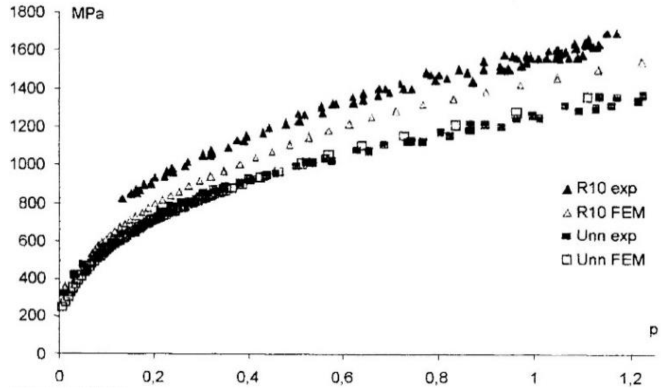

Figure 2.12: True curve obtained via FEM

The true curve obtained from FEM for the unnotched specimen is slightly higher than the curve obtained by experimental test, with errors of about 3%, while the one related to the 10 mm notched radius is about 15% lower than the experimental curve. The reason for this bigger difference in the notched specimens is probably due to the fact that the damage evolution model adopted was not adequate to evaluate the inside voids evolution that led to fracture. However, the Bridgman model has been proved to be not suitable to predict accurately the damage behaviour independently from geometry, since the model strictly depend on the particular geometry chosen. The true curve can be good approximated in case of unnotched geometries, but the post-necking analyses becomes easily unreliable.

2.2 The damage models

To understand how the damage models work, it is necessary to have a look at the theory behind them. Let’s consider a three-dimensional solid body in equilibrium under the action of external mass and surface forces. The only hypothesis made on the material that constitutes it is that the solid body is continuous, so the actions are not considered exchanged between particles and at the molecular size level. Cauchy's hypothesis is assumed to be valid, according to which the forces that exchange the parts of the body in an element’s infinitesimal surface are reducible to the resulting force applied in an internal point of the element itself. To examine the effects of the system of forces, one can imagine the body divided into two parts: in order that each part remains in equilibrium, it is necessary to apply a system of external forces distributed on the separation surface. This system of forces is equivalent to the action that the other part of the body was applying before separation (**Figure 2.13**).

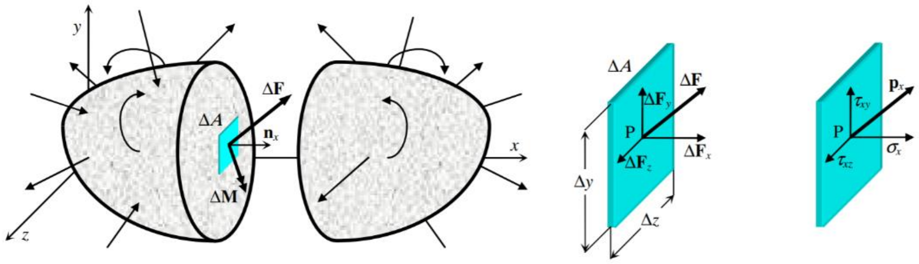

Figure 2.13: Internal forces acting on a surface element ΔA and centered at point P

If the sum **ΔF** of all the forces acting on the element ΔA and centered in P with coordinates **P** = P (x,y,z) is computed, it is possible to define three different traction vectors, $\boldsymbol{p}_x$, $\boldsymbol{p}_y$, $\boldsymbol{p}_z$, which normal directions are identified by $\mathbf{n}_x = [1\ 0\ 0]^T$, $\mathbf{n}_y = [0\ 1\ 0]^T$ and $\mathbf{n}_z = [0\ 0\ 1]^T$, which in turn define the vector **n**.

$$\boldsymbol{p}_i = \lim_{\Delta A \to 0} \frac{\Delta \boldsymbol{F}_i}{\Delta A}$$

Decomposing the sum of the forces into the x, y, and z direction it is possible to determine the normal stress acting along the x direction (σ_{xx}), and the two tangential stresses acting on y and z axes, τ_{xy} and τ_{xz}.

$$\sigma_{xx} = \lim_{\Delta A \to 0} \frac{\Delta F_x}{\Delta A}; \qquad \tau_{xy} = \lim_{\Delta A \to 0} \frac{\Delta F_y}{\Delta A}; \qquad \tau_{xz} = \lim_{\Delta A \to 0} \frac{\Delta F_z}{\Delta A}$$

So, combining these expressions together, the vectors p_x, p_y and p_z can be expressed as:

$$\boldsymbol{p}_x = [\sigma_x \quad \tau_{xy} \quad \tau_{xz}]^T; \qquad \boldsymbol{p}_y = [\tau_{yx} \quad \sigma_y \quad \tau_{yz}]^T; \qquad \boldsymbol{p}_z = [\tau_{zx} \quad \tau_{zy} \quad \sigma_z]^T$$

These nine components of stress, which can also be visible in **Figure 2.14 [39]**, are sufficiently enough to describe the tensional state in one point of the solid body.

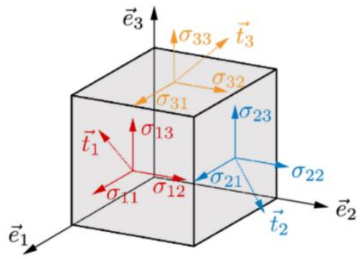

Figure 2.14: Stress state on an infinitesimal cube of material

These stress components are englobed together in a matrix that is called the *stress tensor* of the material:

$$\boldsymbol{\sigma} = \begin{bmatrix} \boldsymbol{p}_x & \boldsymbol{p}_y & \boldsymbol{p}_z \end{bmatrix} = \begin{bmatrix} \sigma_x & \tau_{yx} & \tau_{zx} \\ \tau_{xy} & \sigma_y & \tau_{zy} \\ \tau_{xz} & \tau_{yz} & \sigma_z \end{bmatrix}$$

Let's consider now a generic case, in other words let's take into account a generic direction n characterized by a normal stress σ_n. The tangential stress $\boldsymbol{\tau}_n$ is given by the difference between the vector $\boldsymbol{p}_n$ and the normal stress σ_n. In particular:

$$\boldsymbol{p}_n = \begin{bmatrix} p_{nx} \\ p_{ny} \\ p_{nz} \end{bmatrix} = \boldsymbol{\sigma n} = \begin{bmatrix} \sigma_x & \tau_{yx} & \tau_{zx} \\ \tau_{xy} & \sigma_y & \tau_{zy} \\ \tau_{xz} & \tau_{yz} & \sigma_z \end{bmatrix} \begin{bmatrix} n_x \\ n_y \\ n_z \end{bmatrix}$$

Having in mind this relation, the tangential stress can be evaluated as:

$$\boldsymbol{\tau}_n = \boldsymbol{\sigma n} - \sigma_n \boldsymbol{n} = (\boldsymbol{\sigma} - \boldsymbol{I}\sigma_n)\boldsymbol{n} = \boldsymbol{S}_n \boldsymbol{n}$$

I is the identity matrix, while $\mathbf{S}_\mathrm{n}$ is the matrix shown below:

$$\boldsymbol{S}_n = \boldsymbol{\sigma} - \boldsymbol{I}\sigma_n = \begin{bmatrix} \sigma_x - \sigma_n & \tau_{yx} & \tau_{zx} \\ \tau_{xy} & \sigma_y - \sigma_n & \tau_{zy} \\ \tau_{xz} & \tau_{yz} & \sigma_z - \sigma_n \end{bmatrix}$$

So, the tangential stress can be written as:

$$\boldsymbol{\tau}_n = \begin{bmatrix} \tau_{nx} \\ \tau_{ny} \\ \tau_{nz} \end{bmatrix} = \begin{bmatrix} \sigma_x - \sigma_n & \tau_{yx} & \tau_{zx} \\ \tau_{xy} & \sigma_y - \sigma_n & \tau_{zy} \\ \tau_{xz} & \tau_{yz} & \sigma_z - \sigma_n \end{bmatrix} \begin{bmatrix} n_x \\ n_y \\ n_z \end{bmatrix}$$

What has been obtained is the expression of the tangential stress in a generic direction.

The *principal directions* are the ones on which the tangential stresses are equal to zero, and so are the directions along which:

$$\boldsymbol{\tau}_n = \boldsymbol{S}_n \boldsymbol{n} = 0$$

which also means that:

$$\begin{bmatrix} \sigma_x - \sigma_n & \tau_{yx} & \tau_{zx} \\ \tau_{xy} & \sigma_y - \sigma_n & \tau_{zy} \\ \tau_{xz} & \tau_{yz} & \sigma_z - \sigma_n \end{bmatrix} \begin{bmatrix} n_x \\ n_y \\ n_z \end{bmatrix} = 0$$

In order to obtain solutions different from the obvious one, i.e. zero, it must be verified:

$$Det(\boldsymbol{S}_n) = 0$$

According to that, and developing the solution, it is possible to obtain the eigenvalues equation:

$$\sigma_n^3 - I_1 \sigma_n^2 + I_2 \sigma_n - I_3 = 0$$

I_1, I_2 and I_3 are the invariants of the matrix σ:

$$I_1 = \sigma_x + \sigma_y + \sigma_z$$

$$I_2 = \sigma_x \sigma_y + \sigma_y \sigma_z + \sigma_z \sigma_x - \tau_{xy}^2 - \tau_{yz}^2 - \tau_{zx}^2$$

$$I_3 = Det(\boldsymbol{\sigma}) = \sigma_x \sigma_y \sigma_z + 2\tau_{xy}\tau_{yz}\tau_{zx} - \sigma_x \tau_{yz}^2 - \sigma_y \tau_{zx}^2 - \sigma_z \tau_{xy}^2$$

The eigenvalue equation gives rise to a set of three real solutions, σ_1, σ_2 and σ_3. This set of tension defines the principal stresses, directed along the principal directions. If you choose a cartesian reference frame whose axes coincide with the principal directions in the chosen point of the solid, the matrix σ began:

$$\sigma = \begin{bmatrix} \sigma_x & 0 & 0 \\ 0 & \sigma_y & 0 \\ 0 & 0 & \sigma_z \end{bmatrix} = \begin{bmatrix} \sigma_1 & 0 & 0 \\ 0 & \sigma_2 & 0 \\ 0 & 0 & \sigma_3 \end{bmatrix}$$

The mathematical average of these principal stresses defines the hydrostatic stress σ_H, a variable used to define the triaxiality factor (TF) of a material:

$$\sigma_H = \frac{\sigma_x + \sigma_y + \sigma_z}{3} = \frac{1}{3} I_1$$

In the elastic field, if the Young's modulus **E** and the Poisson ratio **ν** of the material are known, it is possible to correlate stress and strain with the expression visible in the following:

$$\begin{Bmatrix} \varepsilon_x \\ \varepsilon_y \\ \varepsilon_z \\ \varepsilon_{xy} \\ \varepsilon_{xz} \\ \varepsilon_{yz} \end{Bmatrix} = \begin{bmatrix} \frac{1}{E} & -\frac{\nu}{E} & -\frac{\nu}{E} & 0 & 0 & 0 \\ -\frac{\nu}{E} & \frac{1}{E} & -\frac{\nu}{E} & 0 & 0 & 0 \\ -\frac{\nu}{E} & -\frac{\nu}{E} & \frac{1}{E} & 0 & 0 & 0 \\ 0 & 0 & 0 & G & 0 & 0 \\ 0 & 0 & 0 & 0 & G & 0 \\ 0 & 0 & 0 & 0 & 0 & G \end{bmatrix} \begin{Bmatrix} \sigma_x \\ \sigma_y \\ \sigma_z \\ \sigma_{xy} \\ \sigma_{xz} \\ \sigma_{yz} \end{Bmatrix}$$

where $G = \frac{E}{2(1+\nu)}$ is the shear modulus. According to the Von Mises criterion, the combination of stresses acting on the material can be equalled to one single stress acting on the point of the material considered. In other words, the combination of different stresses can be approximated by one single equivalent stress whose effects are the same of the original stresses applied:

$$\sigma_{eq} = \sqrt{\frac{1}{2}[(\sigma_1 - \sigma_2)^2 + (\sigma_1 - \sigma_3)^2 + (\sigma_2 - \sigma_3)^2]}$$

If this equivalent stress is equal to the yield stress of the material, the point considered is a yield point. At this point the triaxiality factor of the material can be defined:

$$TF = \frac{\sigma_H}{\sigma_{eq}}$$

In ductile materials, the fracture occurs due to propagation of microcracks, or coalescence of voids, already present inside the material or originated from plastic deformation, and the triaxiality factor defines the specific rupture that the material experiences. Indeed, the change in size of a vacuum just originated can be broken down into two parts: one attributable to variations in shape, linked to the single component of the deformation tensor, the other attributable instead to volume variations, linked to the equivalent plastic deformation and to the value of the triaxiality factor.

2.2.1 Wierzbicki – Xue damage model

Wierzbicki assumed that a fracture occurs when the accumulated equivalent plastic strain, modified by a function of the stress triaxiality and the deviatoric state parameter ξ, reaches a critical value. The fracture behaviour of this damage model is described as follow **[40]**:

$$\bar{\varepsilon_f} = C_1 e^{-C_2 \eta} - [C_1 e^{-C_2 \eta} - C_3 e^{-C_4 \eta}](1 - \xi^{1/n})^n$$

$$\eta = \frac{\sigma_H}{\sigma_{eq}}$$

$$\xi = \frac{27}{2} \frac{det(S_n)}{\sigma_{eq}^3}$$

where η is the triaxiality factor and $\bar{\varepsilon}_f$ is the strain at fracture. The variables C_1, C_2, C_3, C_4, and n are model parameters. Instead, the damage variable is defined as:

$$D = \int \frac{d\bar{\varepsilon}}{\bar{\varepsilon}_f(\eta, \xi)}$$

The Wierzbicki – Xue damage model assumes that a fracture occurs when the accumulated equivalent plastic strain, related with stress triaxiality η and deviatoric state parameter ξ, reaches the unity value. To better calibrate the model variables, the average values of η and ξ are evaluated as follow **[41]**:

$$\eta_{avg} = \frac{1}{\bar{\varepsilon}_f} \int_0^{\bar{\varepsilon}_f} \eta(\bar{\varepsilon}) d\bar{\varepsilon}$$

$$\xi_{avg} = \frac{1}{\bar{\varepsilon}_f} \int_0^{\bar{\varepsilon}_f} \xi(\bar{\varepsilon}) d\bar{\varepsilon}$$

Xue demonstrated that the most favourable fracture condition occurs in case of tension of round bars where the deviatoric state variable ξ equals the value 1, which corresponds to the highest value of ductility reached. The deviatoric state parameter ξ is very important since it describes the evolution of the ductility level of the material, which can be described by a family of elliptic functions:

$$\left(\frac{\Delta \bar{\varepsilon}_f}{\bar{\varepsilon}_f^{axi} - \bar{\varepsilon}_f^{pl}} \right)^{1/m} + \xi^{1/m} = 1$$

The graphical relationship between the fracture strain and the deviatoric state variable is shown in **Figure 2.15** [41].

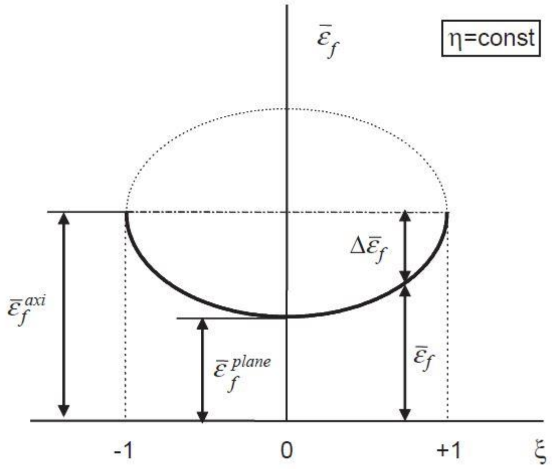

Figure 2.15: Dependence of $\bar{\varepsilon}_f$ with ξ

A practical application of the Wierzbicki – Xue damage model is provided by Šebek et al. [40], whose study analyses the Wierzbicki – Xue damage model in a cutting operation of steel AISI 1045. Specimen dimensions are 6 mm in diameter, and 30 mm gauge length. The test speed is 2 mm/min.

To predict the value of the strength coefficient and strain hardening exponent, the Hollomon model was used to fit the flow curve obtained from experimental tests. Beside tensile tests of smooth cylindrical specimen, there were conducted tensile tests of notched cylindrical specimens and biaxial tests of notched tube specimen. Using biaxial testing of the notched tube specimen, different stress states could be reached by different loading ratios. The quasi-static loading conditions used could be expressed as ratios of an axial and torsional loading components. Ratios –1, –0.5, 0, 0.5, 1, 4.2, and ∞ in mm/rad were chosen. The non-linear least square method was adopted to calibrate the fracture criteria model variables with their optimal value, and simulations were run on Abaqus software. Together with Wierzbicki – Xue, also the extended Mohr – Coulomb and the Bai and Wierzbicki models were analysed. According to the Mohr – Coulomb criteria, the fracture strain is given by [40]:

$$\bar{\varepsilon}_f = \left[\frac{K}{E_2}\left(\sqrt{\frac{1+E_1^2}{3}}\cos\left(\frac{\pi\vartheta}{6}\right) + E_1\left[\eta + \frac{1}{3}\sin\left(\frac{\pi\vartheta}{6}\right)\right]\right)\right]^{-\frac{1}{n}}$$

while the model proposed by Bai and Wierzbicki evaluates the fracture strain as [40]:

$$\bar{\varepsilon}_f = \left(\frac{1}{2}(D_1e^{-D_2\eta} + D_5e^{-D_6\eta}) - D_3e^{-D_4\eta}\right)\vartheta^2 + \frac{1}{2}(D_1e^{-D_2\eta} + D_5e^{-D_6\eta})\vartheta + D_3e^{-D_4\eta}$$

In **Figure 2.16** [40] it is possible to see the results of experimental and model predicted curves.

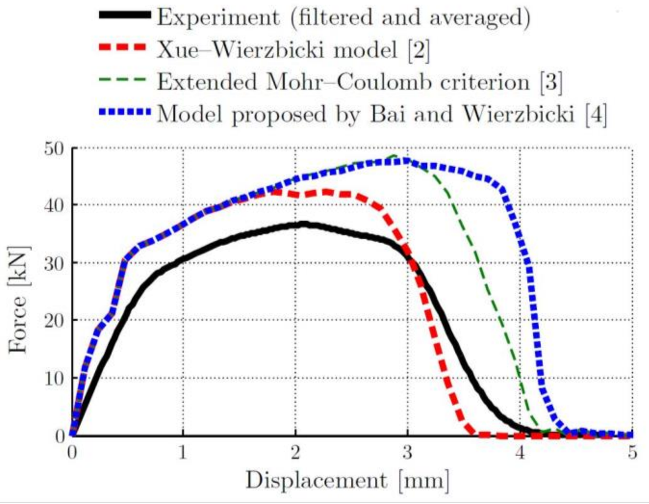

Figure 2.16: Experimental and simulated force-displacement curves

The closest prediction is provided by the Wierzbicki – Xue damage model, while the worst one by the Bai and Wierzbicki model. The possible cause of errors attributable to Bai and Wierzbicki model could be the poor shape of its fracture envelope in low stress triaxialities. For this reason, in this project only the Wierzbicki – Xue is principally described, and not the other ones listed in the figure.

2.2.2 GISSMO model

The GISSMO model (Generalized Incremental Stress State dependent damage MOdel) is used to combine the damage models for crashworthiness simulations and the models for localization and instability used for forming applications. Doing that will increase the accuracy in crashworthiness simulation and the more accurate the simulations are, fewer practical tests need to be carried out. GISSMO model is a damage mechanics model that uses a constitutive model to predict the uniformly plastic behaviour before necking. To be able to catch the unstable plastic behaviour after necking, a curve describing the onset of necking from experiments is iteratively used as a weighting function for the simulation since the stress state varies with plastic deformation. In crashworthiness simulations, the stress is usually represented by the stress triaxiality η:

$$\eta = \frac{\sigma_m}{\sigma_{VM}}$$

where σ_m is the mean stress and σ_{VM} is the Von Mises stress. A common assumption in metal sheets is to consider null the third principal stress, and so the Von Mises stress reduces to the root square of the sum between the first and second stresses squared, minus the product between the two stresses. In order to consider different strain paths, an incremental damage model function is introduced:

$$\Delta D = \frac{n}{\varepsilon_f} D^{\left(1-\frac{1}{n}\right)} \Delta\varepsilon_v$$

ε_f is the triaxiality dependent failure strain, while $\Delta\varepsilon_v$ is the notation for the incremental step in equivalent plastic strain. In order to simulate the instability of the material, the incremental formability intensity is introduced:

$$\Delta F = \frac{\Delta\varepsilon_v}{\varepsilon_{v,loc}}$$

Both the variables ΔD and ΔF are evaluated at every time step of the simulation, so they are calculated incrementally to consider every time the variation of the stress state. $\varepsilon_{v,loc}$ is defined as the equivalent plastic strain to localization, and is dependent of the triaxiality. F=0 corresponds to the undeformed material, and F=1 corresponds to the point where necking occurs. A damage threshold, D_{crit}, is defined either as a fixed value or as a function of the forming intensity at the actual state of deformation. When the damage reaches this curve for the actual triaxiality, the damage threshold will be stored for the actual element and the flow stress and the damage will be coupled.

The effective stress tensor is so corrected with this damage factor **[42]**:

$$\sigma_r = \sigma_n\left(1-\left(\frac{D-D_{crit}}{1-D_{crit}}\right)^m\right)$$

where m is called fading exponent. An application of the GISSMO model on a DP800 specimen will follow. The calibration of the model parameters is done by inverse method. To that end, the experimental result of six different specimens is used: one dog bone, one notched, and two shear-tension types. Their geometries are visible in **Figure 2.17** [42].

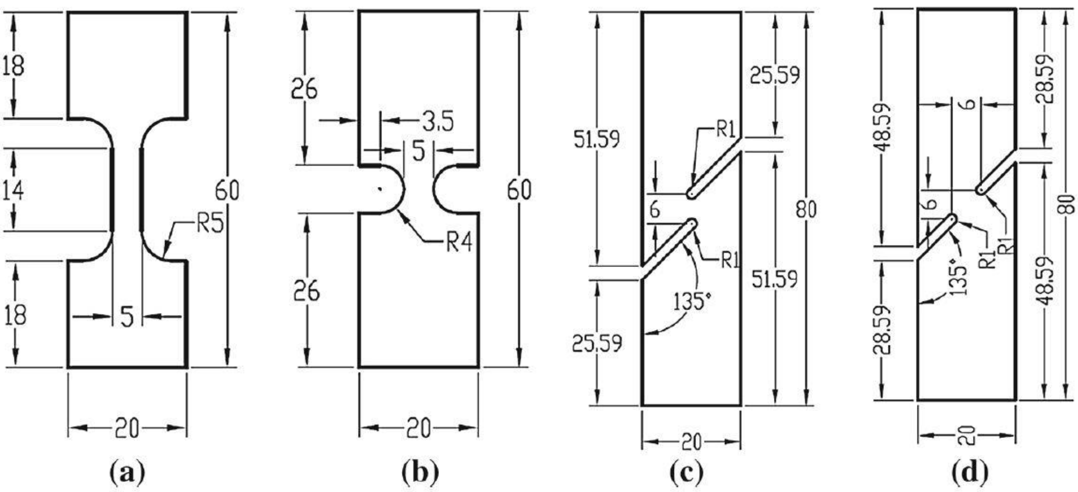

Figure 2.17: Geometries used for studying the GISSMO model

The specimens were cut from a material plate whose thickness was equal to 1.5 mm. In the present calibration, the damage and the fading exponent were identified as n = 2 and m = 2.5, respectively. Experiments have been conducted at constant room temperature, using a universal tensile testing machine in order to obtain the force displacement curves where the force has been measured by the load cell integrated in the testing machine. The displacement has been measured through a mechanical strain gauge fixed on the specimens. Different parametrized hardening curves have been used to properly match the experimental force – displacement curves. For the numerical simulations, the specimens have been discretized with linear shell elements of 0.5 mm size. Also, they have been carried out using the explicit mechanical solver of the commercial finite element code LS-DYNA. Just for having a reference, the GISSMO model has been compared also with the Gurson – Tvergaard – Needleman (GTN) damage model, which is described in the following pages. **Figure 2.18** shows the result of the tests.

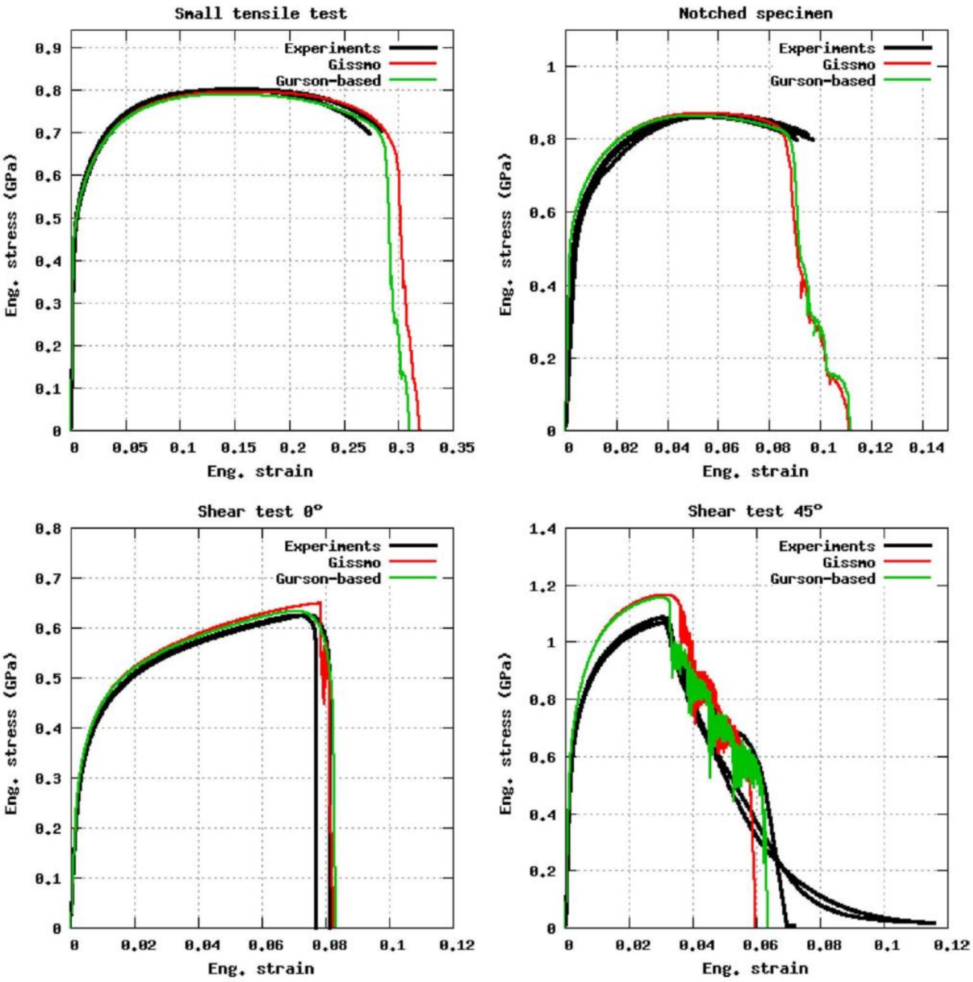

Figure 2.18: Simulation results with GISSMO model

The simulated curves reproduce accurately the experimental curves, with some exceptions on the shear test 45° specimen test, whose maximum force was overestimated by the simulation. The problem could be imputable to the fact that the second invariant of the plasticity model cannot accurately replicate the plastic straining process.

It is also interesting to have a look at the simulation output in terms of stress distribution on the specimens. This aspect is shown in **Figure 2.19** [42] where a prior-to-failure situation is evidenced with the correspondent virtual case obtained on software simulation. There is also the trend of the triaxiality as a function of the plastic strain reached for each type of specimen.

Dog bone

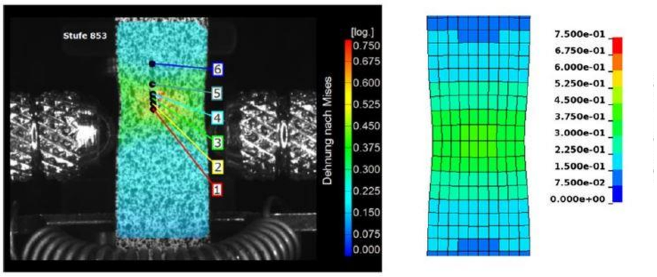

Notched

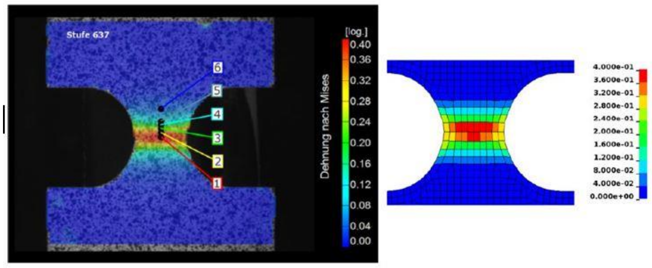

Shear 0°

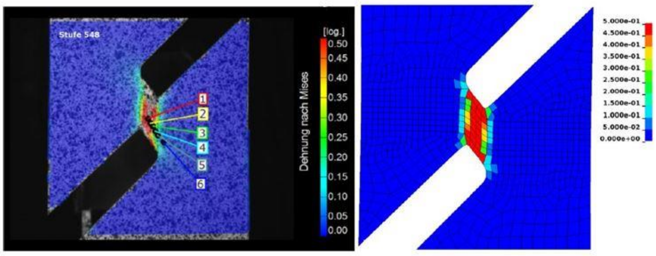

Shear 45°

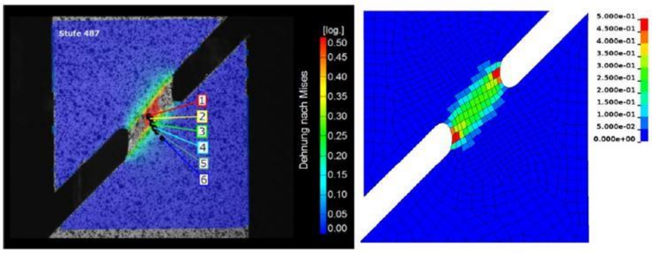

Figure 2.19: Prior-to-failure DIC vs FEM plastic strain distribution

The images of the deformed specimens are obtained via Digital Image Correlation technique. From the figure it is clearly visible that the simulated result obtained by virtual simulations are very close to the experimental result read by DIC. The problem seen before for the shear 45° test is repeated again. Looking at the figure, we can see how the stresses evaluated by virtual simulations are roughly halved with respect to the ones measured by Digital Image Correlation. Again, the cause can be imputable to the limitations of the plasticity model adopted. However, the agreement between simulation and experiment is reasonable, indicating that the material parameters used in the simulation are able to reproduce the material behaviour within a certain accuracy range. The GISSMO damage/failure model has been conceived aiming to be a reasonable compromise between the current findings in the specialized literature and the applicability in an industrial scenario for finite element simulations in forming and crash applications. Although it has some limitations, it is still a valid damage model to use in Automotive field.

2.2.3 Sancho – Cox damage model

The Johnson – Cook plastic deformation model evaluates the stress according to the expression below, in which also the effect of the temperature is considered **[43]**:

$$\bar{\sigma} = \left[A + B\bar{\varepsilon}_{pl}^{n}\right]\left[1 + C\ln\left(\frac{\dot{\bar{\varepsilon}}_{pl}}{\dot{\bar{\varepsilon}}_{0}}\right)\right]\left[1 - \left(\frac{T - T_{ref}}{T_m - T_{ref}}\right)^{m}\right]$$

where $\overline{\sigma}$ represents the von Mises equivalent stress, $\bar{\varepsilon}_{pl}^{n}$ the equivalent plastic strain, $\dot{\bar{\varepsilon}}_{pl}$ the equivalent plastic strain-rate, $\dot{\bar{\varepsilon}}_{0}$ the reference strain-rate, T the temperature, T_m the material melting temperature, T_{ref} the reference temperature and A, B, n, C and m the model parameters. The first term represents the isotropic plastic strain hardening, the second term the strain-rate hardening and the third term the temperature softening. This model can be extended to fracture according to the methodology proposed by Sancho, Cox et. al [43]. To represent the ductile fracture point of the hardening curve, the following formula is used:

$$\bar{\varepsilon}_{pl,f} = \left[D_1 + D_2\exp\left(D_3\eta\right)\right]\left[1 + D_4\ln\left(\frac{\dot{\bar{\varepsilon}}_{pl}}{\dot{\bar{\varepsilon}}_{0}}\right)\right]\left[1 + D_5\left(\frac{T - T_{ref}}{T_m - T_{ref}}\right)\right]$$

where $\overline{\varepsilon_{pl,f}}$ represents the fracture equivalent plastic strain, η the stress triaxiality, D_1, D_2, D_3, D_4 and D_5 the damage model parameters. To better evaluate the stress acting on the material, the damage model parameter D is introduced, and expressed as:

$$D = D_{cr}\left(\frac{\bar{\varepsilon}_{pl} - \varepsilon_{th}}{\bar{\varepsilon}_{pl,f} - \varepsilon_{th}}\right)^{\frac{m}{(\varepsilon_{pl,f})^{q}}}$$

D is calculated it is calculated incrementally, thus taking into account the variation of the stress state over time. It includes an exponent which depends on the stress state through the fracture equivalent plastic strain ($\overline{\varepsilon_{pl,f}}$) and on the material by means of the model parameters m and q, $\overline{\varepsilon_{pl}}$ represents the accumulated equivalent plastic strain, ε_{th} the threshold plastic strain and D_{cr} the critical damage. Fracture is considered to occur when the accumulated damage reached a critical value of D = 1, i.e. when $\overline{\varepsilon_{pl}} = \overline{\varepsilon_{pl,f}}$.

An interesting application of Johnson – Cook damage model is given by Ockewitz **[44]**, whose study involves the cited damage model and the GTN model (later described) to analyse the crash behaviour of aluminium automobile components. The mechanism of ductile rupture is described by three phases, which are void nucleation, void growth, and coalescence. The void growth depends not only on the equivalent plastic strain but also on triaxiality which is defined as the ratio of the mean stress to the von Mises effective stress. Therefore, damage behaviour of a component depends strongly on load type and on geometry. Also, the damage behaviour is influenced by the strain rate. Regarding the Johnson – Cook damage model, the fracture strain depends on triaxiality, strain rate, and temperature, and it is calculated as seen before in the previous page for $\bar{\varepsilon}_{pl,f}$. The temperature effect is not considered since the experiments are done at constant temperature. Failure occurs when the damage variable D reaches 1 as value. The Gurson – Tvergaard – Needleman damage model used as comparison is based on the following yield condition [44]:

$$\phi = \frac{\sigma_e^2}{\sigma_M^2} + 2q_1 f^* cosh\left(\frac{tr\sigma}{2\sigma_M}\right) - 1 - (q_1 f^*)^2 = 0$$

where σ is the macroscopic stress tensor, σ_e is the equivalent Von Mises stress, σ_M the actual yield stress, and f^* is a function of the void volume fraction f provided by:

$$f^*(f) = \begin{cases} f & if\ f < f_c \\ f_c + \dfrac{1/q_1 - f_c}{f_f - f_c}(f - f_c) & if\ f > f_c \end{cases}$$

f_f is the critical void volume fraction at the beginning of coalescence, while f_c is the critical void volume fraction at final rupture. The GTN damage model takes into account also the evolution equations for the porosity and the nucleation of new voids, but we will see further on this concept. The authors chosen the GTN model in particular because it is able to describe the porosity and its evolution as damage goes on. However, it has also a limitation, which consist in do not consider the shear action. The tests are performed on a vehicle bumper obtained via extrusion of aluminium profile (7000 alloy), and to have more homogeneous results different types of specimens have been used, visible in **Figure 2.20** [44].

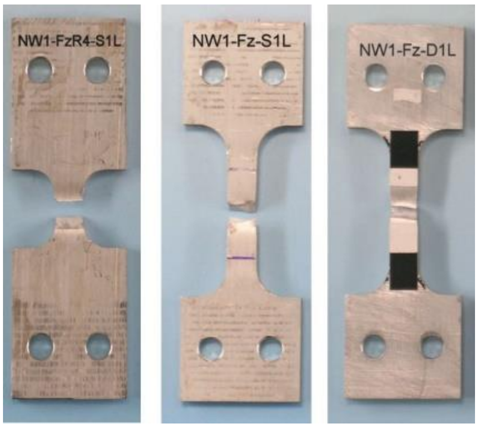

Figure 2.20: Notched (left), smooth static (centre) and smooth dynamic (right) specimens used for the tests

The static and dynamic name of the corresponding specimens refer to the application of static and dynamic loadings during the tensile and shear tests. **Figure 2.21** shows the measured nominal stress vs nominal strain curves obtained from tensile test, from different locations of the specimens along the bumper surface.

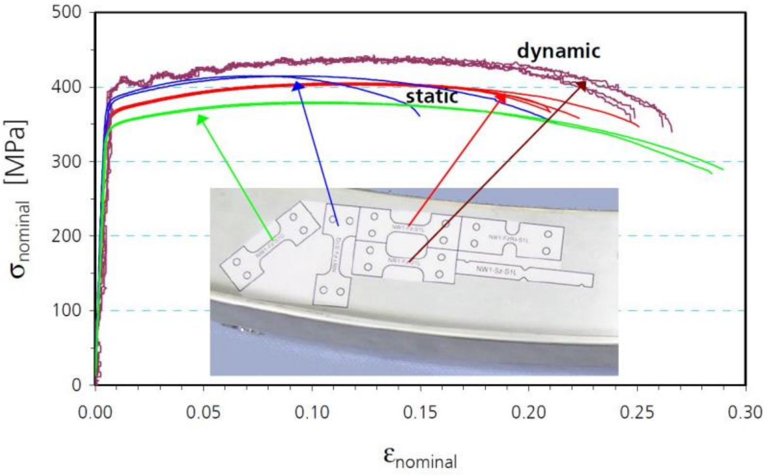

Figure 2.21: Nominal stress-strain curve for different specimens and specimen orientations

It can be notice that the position of the specimen on the bumper does not affect significantly the trend of the curve, while the curve is affected by the orientation of the specimen. The shear test equipment is shown in **Figure 2.22**.

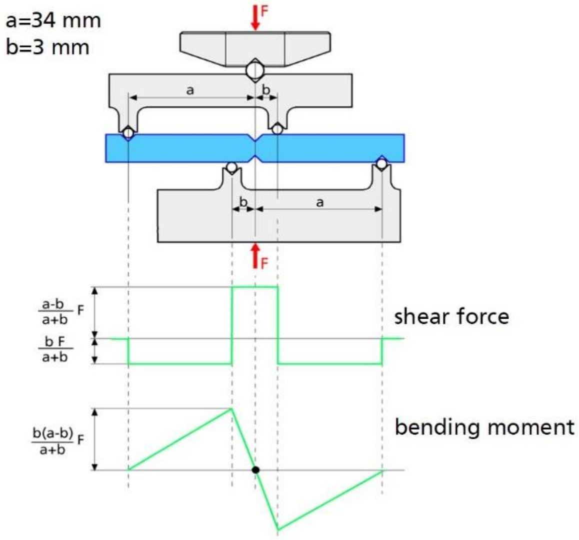

Figure 2.33: Shear test schematization

The test corresponds to an asymmetric four point bending with the cross section between the two notches loaded under pure shear. For the determination of the parameters D_1, D_2 and D_3 of the Johnson-Cook damage model the equivalent plastic strain at failure was evaluated from the experiments and simulations for different values of triaxialities (shear tests $\sigma_m/\sigma_e \approx 0$, smooth tension tests $\sigma_m/\sigma_e \approx 1/3$, notched tension tests $\sigma_m/\sigma_e \approx 0.5$). The parameters D_1, D_2 and D_3 were obtained by fitting a curve similar to the one visible in Figure 2.22 through these three points, while the parameter D_4 was set to zero, in the sense that the dependence of fracture strain on strain rate was not accounted for.

The parameters for the Gurson – Tvergaard – Needleman (GTN) damage model are selected from literature and from simulation of tensile test on smooth specimens, since they are not independent from each other. The variables related to porosity are selected by comparing porosity properties of similar materials. The finite element models used for the determination of the Gurson parameters consist of shell elements, with an element length of 0.5 mm, whereas the element length in the model of the bumper is about 5 mm. **Figure 2.23** shows the result of the shear test, comparing the experimental output with the outputs provided by both the damage models.

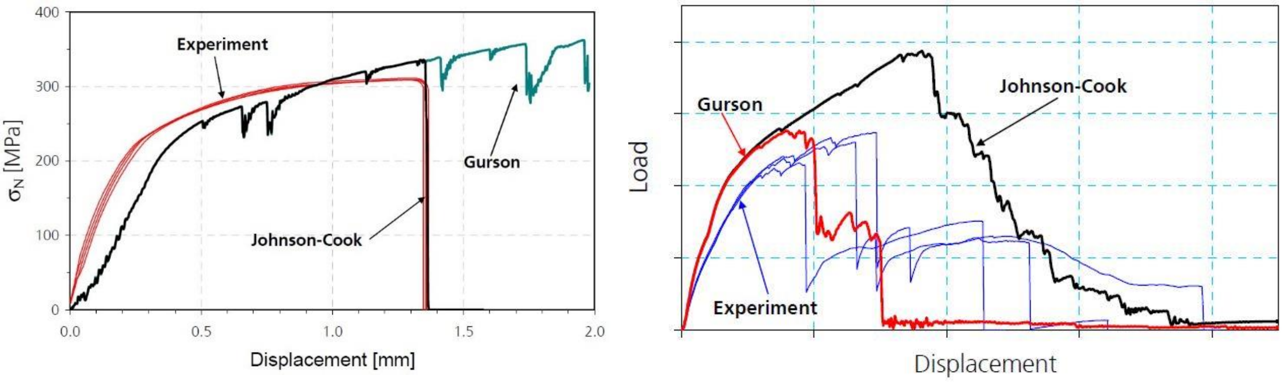

Figure 2.23: Experimental and simulation results for shear test (left) and bending test (right)

From the graphs it is possible to see how the models reacted with respect to the experimental conditions. Concerning the shear test, the Johnson – Cook model approximate quite well the experimental curve, predicting the fracture in the same point at which the fracture occurred in the experiment. The GTN model, instead, predict a more ductile material. On the other hand, passing to the bending test, it is possible to see how, this time, the Johnson – Cook damage model deviates with respect the reality, and how the GTN model, instead, predict well the fracture process. This difference is more clearly visible in **Figure 2.24** [44].

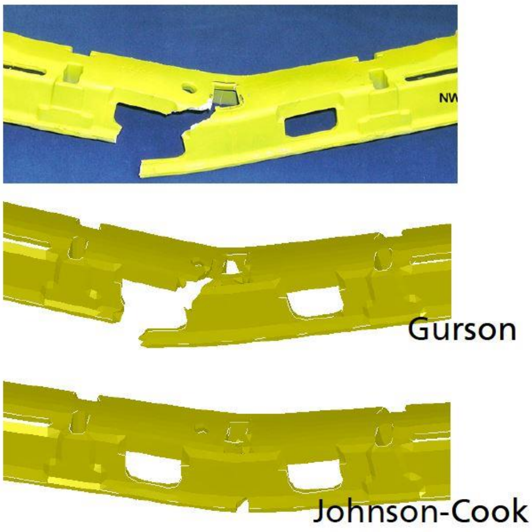

Figure 2.24: Comparison between the predicted fracture and the real case

The simulation with the Johnson - Cook damage model predicted cracking in the middle of the component section, whereas the fracture pattern calculated with the Gurson model is in very good agreement with the experiments. The difference between these two models lies in the fact that the Johnson – Cook damage model parameters underestimate the damage for high values of triaxiality, and a higher precision in the damage predicting behaviour requires specific laboratory tests that are not available for the high triaxiality values reached at failure. On the contrary, the GTN model parameters are valid also for high values of triaxiality without the need of further experiments.

In conclusion, both the damage models are reliable for analysing the crashing behaviour of metals, and they are used in different applications, since the GTN model has limitations in predicting shear failures.

2.2.4 Kim – Yoon damage model

The two researchers of the Department of Mechanical and Automotive Engineering at the Seoul National University **[45]** proposed different damage models based on simple criterions, such as principal plastic strain, equivalent plastic strain, maximum shear strain, and strain energy.

Principal plastic strain damage model

This damage model criterion defines that the damage is initiated when the principal plastic strain is greater than a certain critical value D_{max}. Mathematically, the principal plastic strain damage model is defined as:

$$D = \begin{cases} 0 & \left(\varepsilon_1 \leq \varepsilon_{1f,ini}\right) \\ \dfrac{D_{\max}}{\left(\varepsilon_{1f,\max} - \varepsilon_{1f,ini}\right)^M}\left(\varepsilon_1 - \varepsilon_{1f,ini}\right)^M & \left(\varepsilon_{1f,ini} < \varepsilon_1 < \varepsilon_{1f,\max}\right) \\ D_{\max} & \left(\varepsilon_{1f,\max} \leq \varepsilon_1\right) \end{cases}$$

where $\varepsilon_1$is the principal plastic strain, $\varepsilon_{1f,ini}$ is the principal plastic strain at which damage initiates, $\varepsilon_{1f,max}$ is the maximum principal plastic strain at which the damage value reaches the maximum value D_{max}, and M is the exponent that controls the damage evolution process.

Figure 2.25 [45] shows how the damage variable changes according to the other parameters of the model.

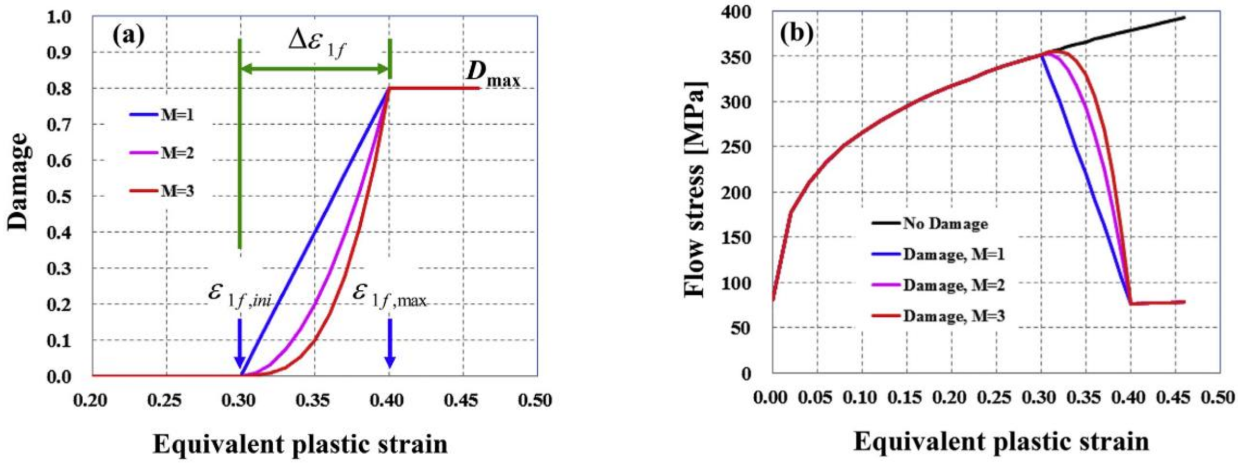

Figure 2.25: Different trends of damage and flow stress

When the exponent M is equal to 1, the damage variable behaves completely linearly, making possible problems during simulations on plastic behaviour prediction. This value of the exponent changes also the behaviour in the flow stress trend. In order to have smoother variations in both the fields, value of M of 2 or 3 are suggested, and their effect is visible in the figure.

Equivalent plastic strain damage model

This damage model criterion defines that the damage is initiated when the equivalent plastic strain is greater than a certain critical value D_{max}. Mathematically, the principal plastic strain damage model is defined as:

$$D = \begin{cases} 0 & \left(\bar{\varepsilon} \leq \bar{\varepsilon}_{f,ini}\right) \\ \dfrac{D_{\max}}{\left(\bar{\varepsilon}_{f,\max} - \bar{\varepsilon}_{f,ini}\right)^{M}} \left(\bar{\varepsilon} - \bar{\varepsilon}_{f,ini}\right)^{M} & \left(\bar{\varepsilon}_{f,ini} < \bar{\varepsilon} < \bar{\varepsilon}_{f,\max}\right) \\ D_{\max} & \left(\bar{\varepsilon}_{f,\max} \leq \bar{\varepsilon}\right) \end{cases}$$

D is damage, D_{max} is the maximum damage value, $\bar{\varepsilon}$ is the equivalent plastic strain, $\bar{\varepsilon}_{f,ini}$ is the equivalent plastic strain at which damage initiates, $\bar{\varepsilon}_{f,max}$ is the maximum equivalent plastic strain at which the damage value equals the maximum value D_{max}, and M is the exponent that has the same meaning as seen in the previous case.

Maximum shear strain damage model

This model defines the damage as initiated and accumulated when maximum shear strain is greater than a certain critical value D_{max}. This model is written as:

$$D = \begin{cases} 0 & \left(\gamma_m \leq \gamma_{mf,ini}\right) \\ \dfrac{D_{\max}}{\left(\gamma_{mf,\max} - \gamma_{mf,ini}\right)^M}\left(\gamma_m - \gamma_{mf,ini}\right)^M & \left(\gamma_{mf,ini} < \gamma_m < \gamma_{mf,\max}\right) \\ D_{\max} & \left(\gamma_{mf,\max} \leq \gamma_m\right) \end{cases}$$

γ_m is the maximum shear strain, $\gamma_{mf,ini}$ is the maximum shear strain over which damage initiates, $\gamma_{mf,max}$ is the maximum shear strain at which the damage value reaches the maximum value D_{max}, and M is the exponent that has the same meaning as that of the principal plastic strain damage model.

Strain energy damage model

This model defines the damage as initiated and accumulated when the equivalent stress is greater than a certain critical value. In this model, damage is accumulated by means of strain energy.

$$dD = \begin{cases} 0 & \left(\overline{\sigma} \leq \overline{\sigma}_{f,ini}\right) \\ \dfrac{\overline{\sigma}}{\overline{\sigma}_{f,ini}\left(\overline{\varepsilon}_{f,\max} - \overline{\varepsilon}_{f,ini}\right)}d\overline{\varepsilon} & \left(\overline{\sigma}_{f,ini} < \overline{\sigma} \text{ and } D < D_{\max}\right) \\ 0 & \left(D_{\max} \leq D\right) \end{cases} \qquad D = \int dD$$

$\bar{\sigma}$ is the equivalent stress, $\bar{\sigma}_{f,ini}$ is the initial critical equivalent stress over which damage initiates, $\bar{\varepsilon}_{f,ini}$ is the equivalent plastic strain, and $\bar{\varepsilon}_{f,max}$ is the strain increment from damage initiation to maximum damage.

The Kim – Yoon damage model has been tested on AA6022-T4 aluminium alloy steel with a tensile test, on software Abaqus CPFEM (Crystal Plasticity Finite Element Method). The CPFEM methodology allows to study the plastic behaviour by the change in movement, orientation, and dimensions of the crystal which made the internal structure of the material examined. For analysing the stress concentration from the orientation mismatch, the element size should be smaller than a grain size. As a consequence, a very high number of elements is needed for a satisfactory level of precision, and for this reason the interest domain of observation has been reduced to what is strictly necessary, as visible in **Figure 2.26** [45]. In the same figure, it is possible to see also the way in which the specimen has been subdivided for the FEM analysis.

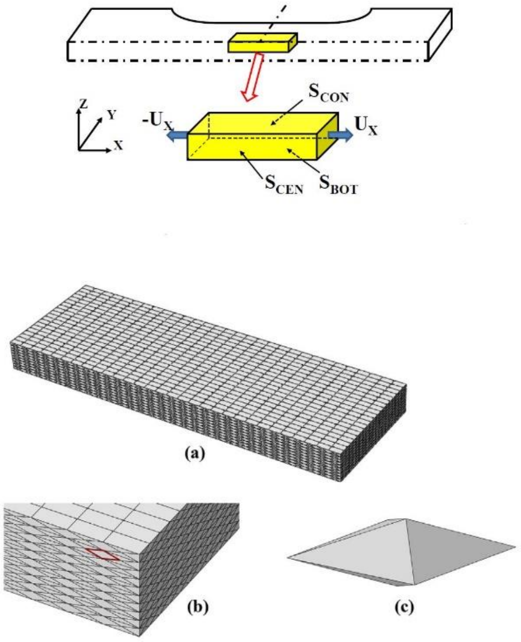

Figure 2.26: Specimen domain and elements geometry

The selected domain is 6.0 mm in length, 2.0 mm in width, and 0.5 mm in thickness. Aluminium alloy sheet thickness is assumed to be 1.0 mm, and a half thickness is chosen considering symmetry to increase the number of elements without negatively affecting the execution time and effort of the simulation. Average grain size is about 0.05 mm. Before implementing the damage mode, it is necessary to obtain the true curve. To this aim, the stress-strain curve has been approximated by using the following expression [45]:

$$\sigma = 479.9(\varepsilon + 0.001)^{0.258}$$

The result of this fitting technique is shown in **Figure 2.27**.

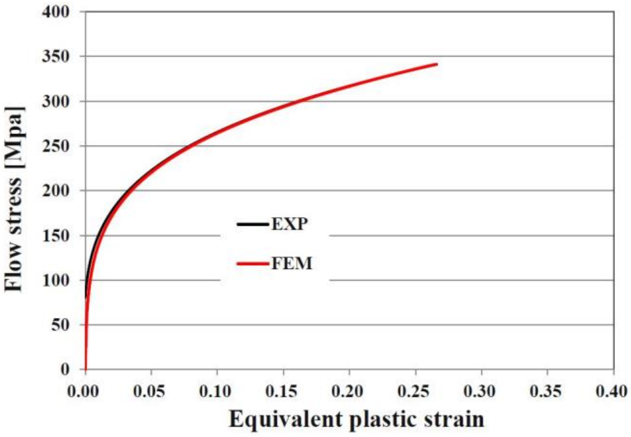

Figure 2.27: Experimental vs fitted stress – strain curve

The FEM curve has been obtained by the CPFEM methodology, and it in a very good relation with the experimental curve. To obtain the optimal values of the damage model parameters, the fitting procedure is repeated for all the variants of the damage model we have seen before. **Figure 2.28** [45] shows the final results of the load – displacement curve.

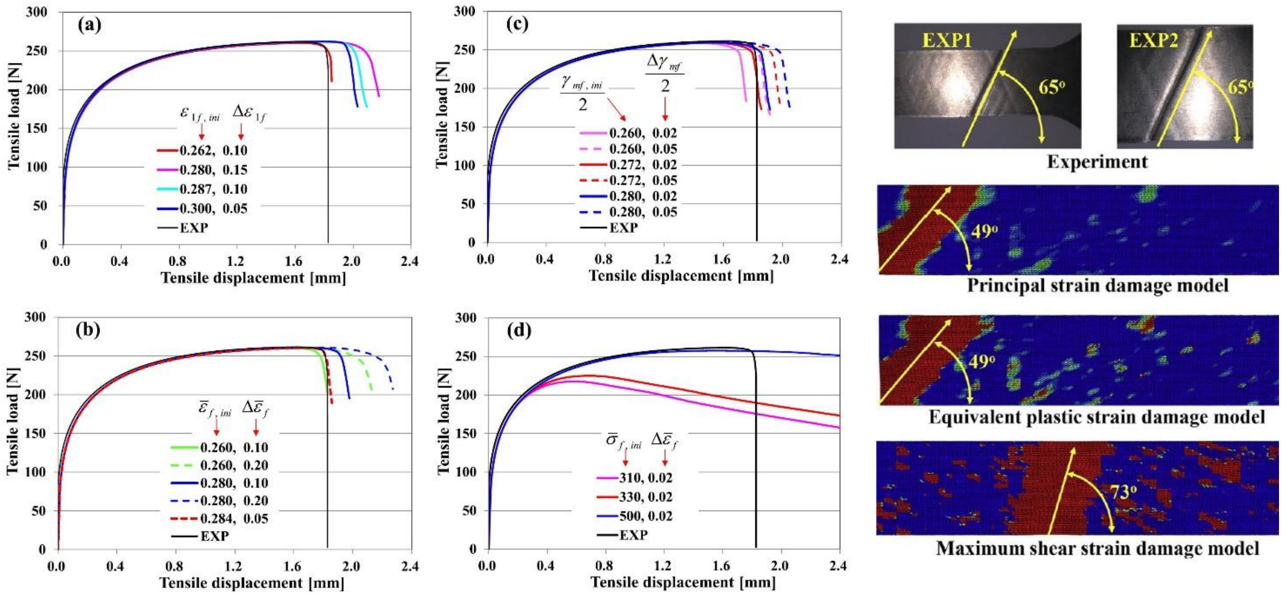

Figure 2.28: Load – displacement curves for various values of damage parameters and predicted fracture: (a) principal strain damage model, (b) equivalent plastic strain damage model, (c) maximum shear strain damage model, (d) equivalent strain energy damage model

A small variation of the parameter's values can lead to high changes, particularly for the equivalent strain energy damage model case. In this last case, the fracture is not predicted. According to the obtained results, the final parameters have the following values:

Principal strain damage model

$$\varepsilon_{1f,ini} = 0.262 \quad \varepsilon_{1f,max} = 0.362 \quad D_{max} = 0.8 \quad M = 2$$

Equivalent plastic strain damage model

$$\bar{\varepsilon}_{f,ini} = 0.284 \quad \bar{\varepsilon}_{f,max} = 0.334 \quad D_{max} = 0.8 \quad M = 2$$

Maximum shear strain damage model

$$\gamma_{mf,ini} \,/\, 2 = 0.272 \quad \gamma_{mf,max} \,/\, 2 = 0.292 \quad D_{max} = 0.8 \quad M = 2$$

The combination of these values produces the fracture paths visible in the same figure. Experiments registered a fracture path inclined of 65° with respect to the longitudinal axis of the specimen, and the maximum shear strain damage model is the one which provides the nearest results, with an inclination of 73°, and with an error of 12%. The principal strain damage model and the equivalent plastic strain damage model gives the same result, i.e. a cracking inclination of about 49°, that corresponds to 25% of error.

Although the necking direction is characterized by some errors, the predictions made by CPFEM and the described damage models are still good. The accuracy can be improved by considering real grain shape and grains interaction, although the void nucleation, growth, and coalescence phenomena were well described by the proposed methodology. As seen also from the figures, the strain energy damage model is not able to describe accurately the necking behaviour, and this is the only limitation of the Kim – Yoon damage model. As a result, the CPFEM with the use of the described damage models, is suitable to be implemented in the analysis of necking behaviour and necking direction.

2.2.5 Gurson – Tvergaard – Needleman (GTN) damage model

In a homogeneous metal model, the total deformation usually doesn't affect the volume change, because the plastic part of the deformation is dominant with respect to the elastic one. Otherwise, in a microstructure model containing voids, volume can globally change, due to the local plastic flow arising around the voids boundary. Consequently, the microstructure response to an imposed global strain will be a stress curve with a softening, nevertheless the material matrix be constituted by a metal with a hardening behaviour. Contemporarily, the voids grow until the global load carry capability becomes negligible. This model is able to explain the local strength decrease during the fracture process of ductile metals in the intermediate phase between the nucleation and the coalescence of voids. In other words, in the void growth model the number of voids is kept constant.

The Gurson – Tvergaard – Needleman damage model is based on a definition of a small cubic cell of material, specifically called Representative Volume Element (RVE). In particular, the RVE of the material is considered as a cubic volume with a single void, existing before the material is stressed. The model assumes that the materials contain voids that grow under positive hydrostatic stresses. The initial void volume fraction f_0 should be chosen as the equivalent volume fraction corresponding to the physical distribution of voids or defects inside the RVE. In other words, while in a single cell it is highly probable to have multiple voids, this damage model considers the same cell which has, inside, a single void which is equivalent to all the voids realistically present.

The GTN damage model constitutive law describes the material behaviour as **[46]**:

$$\phi\left(\sigma_{eq}, \sigma_m, \bar{\sigma}, f\right) = \left(\frac{\sigma_{eq}}{\bar{\sigma}}\right)^2 + 2q_1 f cosh\left(\frac{3q_2\sigma_m}{2\bar{\sigma}}\right) - (1 + q_3 f)^2 = 0$$

where σ_{eq} is the Von Mises equivalent global stress, σ_m is the global hydrostatic stress, $\bar{\sigma}$ is the current matrix flow stress, f is the voids volume fraction, and q_1, q_2 and q_3 are the Tvergaard correction coefficients, which take into account the hardening of the material during its deformation. The increment of the variable values of q_i increases the effects of void volume fraction, that translates into decrement of tensile strength. **Figure 2.29 [47]** shows the effects of changes in q_1 and q_2.

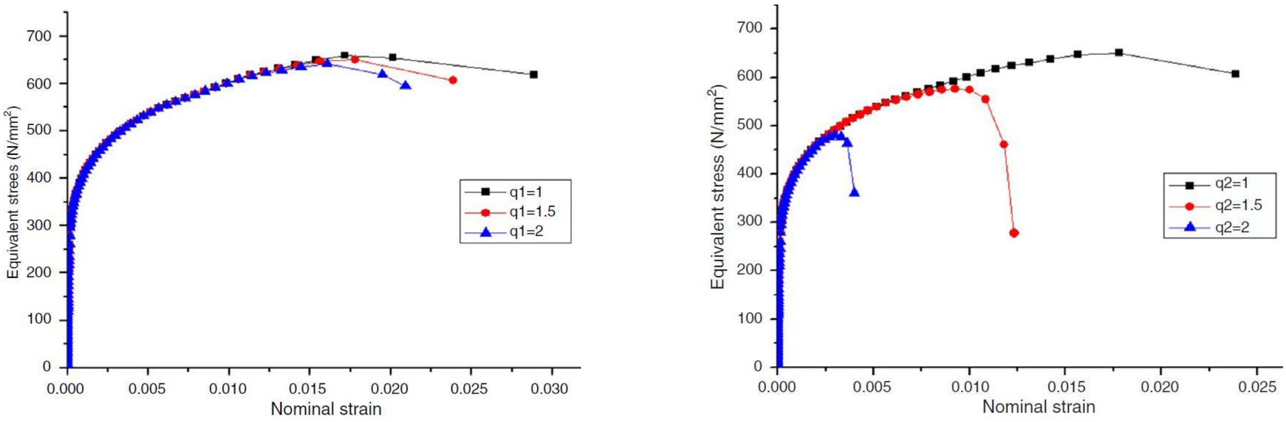

Figure 2.29: Influence of q_1 and q_2 on the stress – strain diagram

As we can see, the q_1 variable does not affect the linear region of the diagram. Lower values of this parameter lead to an increment of the deformation the material is able to sustain, with increasing values of stress reached. In particular, decreasing the value of q_1 of 50%, an increment in deformation of about 26%. In other words, when q_1 is higher than unity, the plastic limit is reached for lower values of stresses. The biggest effects are provided by the parameter q_2, whose changes in its value drastically modify the yield limit, reducing it always more consistently as the value of q_2 goes further from 1. Optimal values of these GTN parameters have been proved to be q_1=1.5, q_2=1, and q_3=q_1^2=2.25 [47].

The voids volume fraction is described by the following relation:

$$\begin{cases} f = f_c \qquad if \qquad f^* \leq f_c \\ f = f_c + \dfrac{\left(\dfrac{1}{q_1}\right) - f_c}{f_f - f_c}(f^* - f_c) \qquad if \quad f^* > f_c \end{cases}$$

where f^* is the damage parameter, f is the void volume fraction, f_c is the voids' volume ratio at the beginning of coalescence and f_f is the voids' volume ratio when fracture occurs. In other words, the parameter f_c characterizes the beginning of void nucleation, while the parameter f_f denotes the final failure. The linear behaviour of the material is not affected by changes in value of the parameter f_c. The f_c value influences the fracture position of the equivalent stress–nominal strain curve of notched specimens. Higher f_c values can lead to earlier failure of the specimen while the slope of all the curves after fracture initiation is constant; therefore, its mechanical properties are affected and weakened, that is resulted in the rapid degradation of the load and voids initiation for low loads. The only effect that parameter f_c provides is to increase the falling speed of the load in the fracture region. **Figure 2.30** shows the effects of a change in value of f_c parameter on the stress – strain diagram.

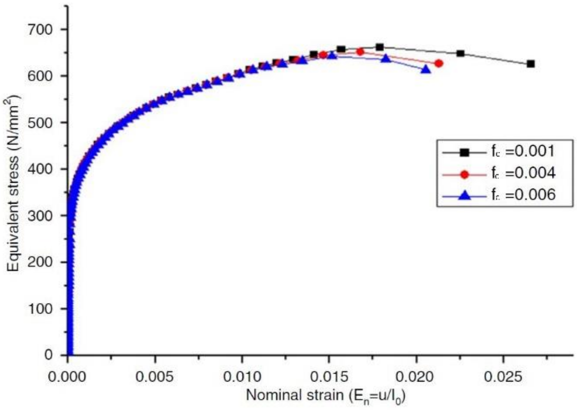

Figure 2.30: Influence of f_c on the stress – strain diagram

An interesting application of the Gurson – Tvergaard – Needleman damage model is provided by Xu Y. and Qian C. **[48]**, which study are aimed at verify the reliability and precision of the GTN damage model by tensile tests on round steel bars used as a reinforcement in concrete elements. The steel bars have a diameter of 12 mm, and length of 100 mm. The true curve of the steel used in the reinforcement bars is visible in **Figure 2.31** [48]. The ductile fracture occurs from nucleation, growth, and coalescence of microvoids, which dynamics and evolution during the deformation is described by the GTN damage model. In particular, this evolution can be described by the following expression: $\dot{f} = \dot{f}_{growth} + \dot{f}_{nucleation}$. In this relation, the first term represents the growth rate of existing voids, while the second one describes the nucleation of voids as deformation proceeds. The terms are evaluated as:

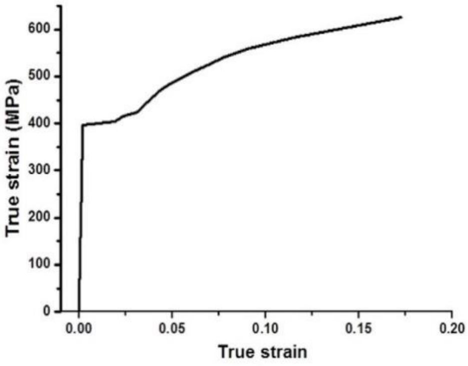

Figure 2.31: True curve of steel bar

$$\dot{f}_{growth} = (1-f)\dot{\varepsilon}_{kk}^{p}$$

$$\dot{f}_{nucleation} = \frac{f_N}{S_N\sqrt{2\pi}} exp\left[-\frac{1}{2}\left(\frac{\varepsilon_0^p - \varepsilon_N}{S_N}\right)^2\right]\dot{\varepsilon}_0$$

$\dot{\varepsilon}_{kk}^{p}$ is the plastic hydrostatic strain, S_N and ε_N are the standard deviation and mean value of the plastic strain distribution, while ε_0^p is the equivalent plastic strain of matrix material, since the steel bars are reinforcement and are inserted into a matrix to strengthen its properties. The values of S_N and ε_N have been arbitrarily chosen 0.1 and 0.3 respectively [48]. The Finite Element analysis are carried out on Abaqus software. **Figure 2.32** shows the specimen geometry (on the left), the boundary conditions (in the middle), and the meshing geometry and dimension (on the right) of the steel bar used for the simulation tests.

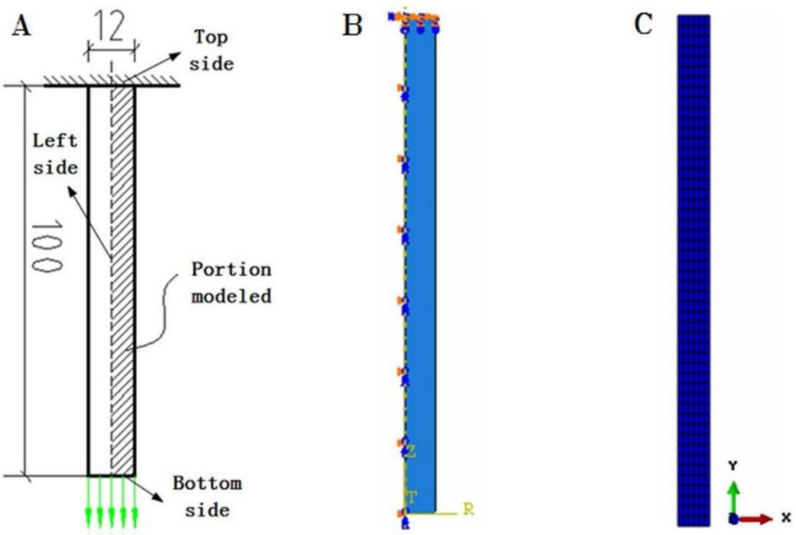

Figure 2.32: Steel tensile specimen used for tests

The boundary conditions applied are x-direction symmetry, and so half specimen has been modelled, together with constraints on x axis movements, and no rotation about y and z axes. The displacement was applied to the bottom side of the model to obtain the deformations desired. The meshing elements are axisymmetric quadrilateral elements. The tests are done in order to predict the plastic behaviour and to detect differences in case of changes in values of the GTN damage model parameters. **Table 3** [48] shows the value of the GTN damage model parameters adopted in the corresponding simulations.

Experiment	q_1	q_2	f_c	f_f	σ_y	σ_t
#1	1.5	1.0	0.015	0.25	387.85	517.23
#2	2.5	1.0	0.020	0.20	377.40	492.40
#3	3.5	1.5	0.015	0.20	360.47	422.80

Table 3: GTN damage model parameters

The variables σ_y and σ_t represents, respectively, the yield and tensile strength predicted by the Gurson – Tvergaard – Needleman damage model. The change in values of these variable lead to consistent modifications in the stress – strain diagram. In particular, the simulations proved that an increment of q_1 variable, which takes into account the hardenability function, leads to a reduction of both the yield and the tensile strengths. Furthermore, the effects of the failure parameters are negligible with respect to the effects generated by the constitutive parameters q_i. In **Figure 2.33** it is possible to see the different fracture pattern obtained with a different set of constitutive and fracture parameters.

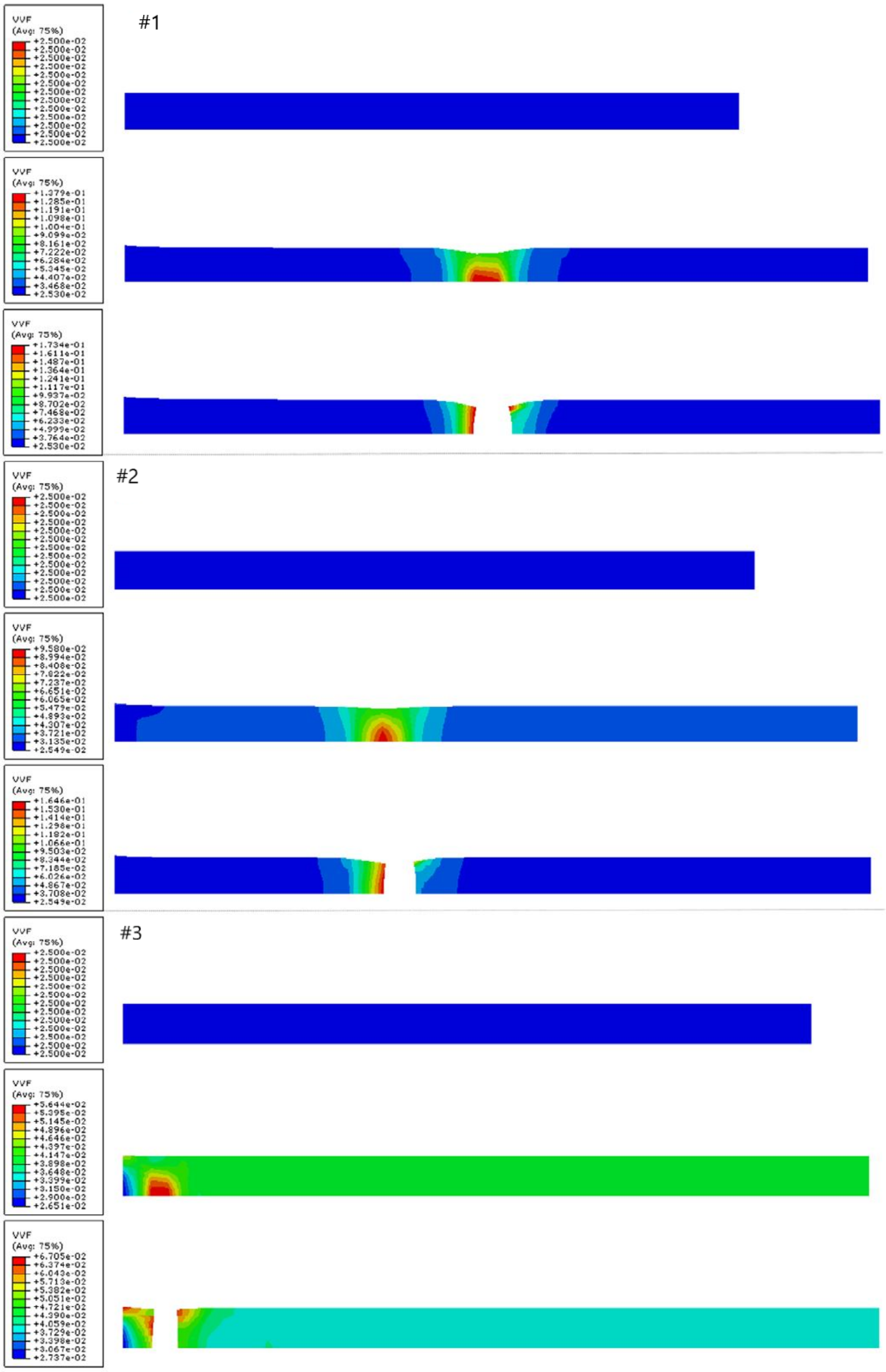

Figure 2.33: Different fracture patterns obtained in the tests

We can easily notice how the necking region is moving to the top of the specimen as the constitutive parameters are increased in value, and how, at the same time, the common cup-cone fracture shape becomes always more linear and flatter. So, the necking zone moves upwards gradually and the fracture pattern changes from toughness to brittleness, and this consequence can be seen in **Figure 2.34**, which evidences the effects of the three experiments on the nominal stress- strain curve of the initial steel bar.

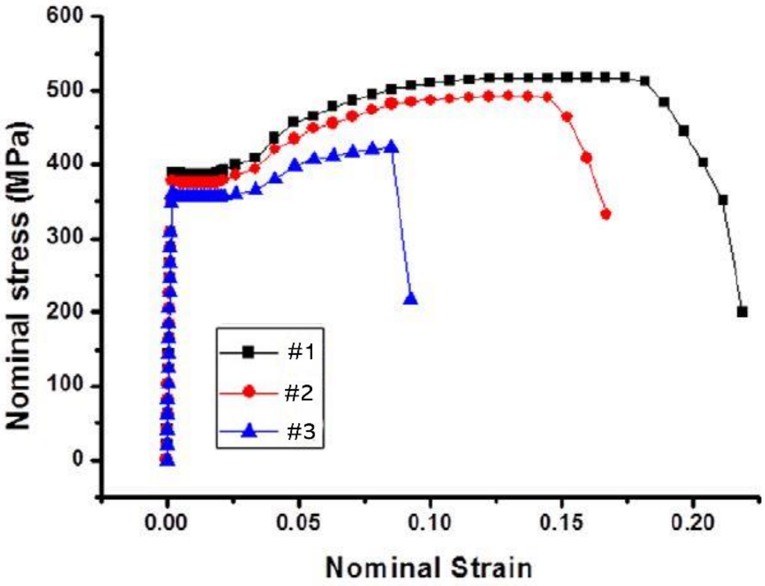

Figure 2.34: Experimental calculated nominal stress – strain curves

The Gurson – Tvergaard – Needleman damage model proves that the major effects on plastic behaviour prediction are given according to that order: $q_1 > q_2 > f_f > f_c$ for yield strength, and $q_1 > q_2 > f_c > f_f$ for tensile strength. Small values of constitutive parameters result in larger elongations.

To conclude, it has been shown that the GTN damage model parameter is a valid methodology to be used for plastic behaviour estimation. It is characterized by high precision, and different fracture patterns can be obtained by setting different values of constitutive parameters, so the GTN damage model is suitable to be adopted in different cases to analyse different plastic behaviours.

Chapter 3 – Real case application

This chapter focuses on the description of the procedure followed to evaluate the mathematical models that has been used to represent the mechanical behaviour of the materials, and to verify the validity of the same models. The tests have been carried on dog bone, or smooth, specimens. The necessary data are obtained from these physical tests, and with the use of the Digital Image Correlation (DIC) technique. This method will be further described in more detail; however, it is a technique that consent to register every deformation instant at which the material is subjected. Subsequently, a comparison between the tests for each geometry is done, to evaluate the specimen which behaves better, and this will be taken as reference for the further steps of the project. This reference specimen is then use to determine the true stresses and the true strains, that allow to further study the damaging behaviour of the material considered. In particular, we are interested in evaluating the plastic behaviour, after the onset of the necking, by the use of mathematical models. Within these models, and more generally in whatever model it is used, it is fundamental to respect the necking constraints, according to which the derivative of the stress with respect to the strain at the necking point has to be equal, or at least similar, to the value of the stress at the necking point. This condition is needed to perform the software simulations correctly, since without that constraint the onset of necking is initiated where it shouldn't. When the mathematical model is correctly implemented, it is ready to be used in the software simulations. Indeed, this mathematical model will be the input of the virtual tests. From now on, the text describes the followed procedure by taking the QP1180 steel as a reference example. Another section will take into account the results achieved for all the materials analysed.

3.1 Specimens geometry

The dog bone geometry is shown in **Figure 3.1**.

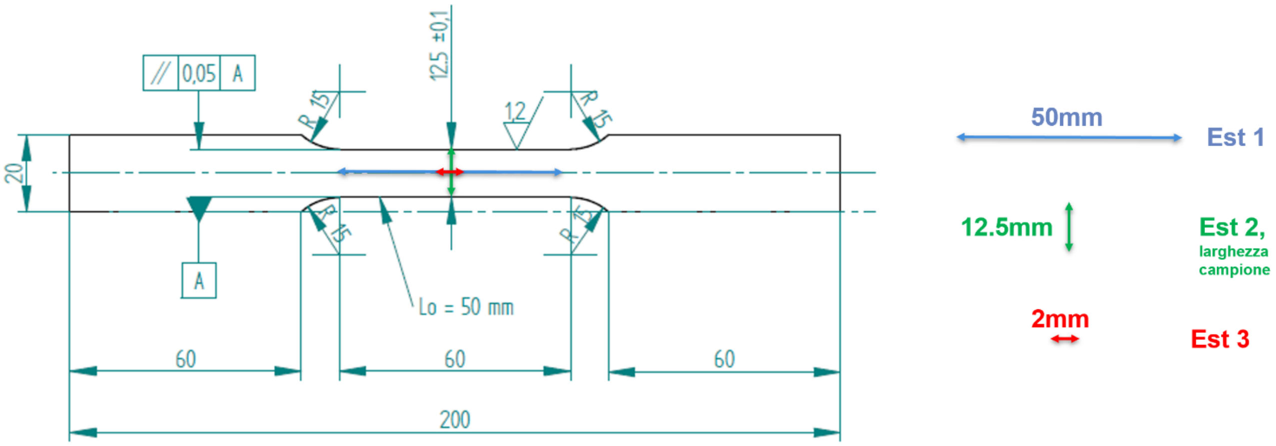

Figure 3.1: Dog bone geometry

For each specimen, a set of virtual extensometers is fixed, in order to measure the local deformations in the most stressed areas. The first extensometer (the blue one), that in the smooth geometry is long 50 millimetres, is placed longitudinally, as well as the third extensometer (the red one), which is aimed at evaluated, with more precision, very specific deformations, in very restricted zones of the specimen. The second extensometer (the green one) is place transversally, to measure the restriction of the middle section of the specimen during the longitudinal elongation. Those extensometers measure the strains on the specimen at the correspondent level of stresses, and what we obtain is the engineering curve of the mechanical behaviour of the specimen. As we will see later on, the engineering curve has to be transformed into a true curve, simply by the application of a mathematical formula. This action is needed because the engineering curve does not consider the effective, or instantaneous, length and area of the specimen along the deformation, but only the initial ones, so the results are not very precise as those obtained in the true curve. A specific specimen geometry has its value of triaxiality. The triaxiality is defined as the ratio between the average, or hydrostatic stress, and the Von Mises equivalent stress. The hydrostatic stress is simply the average between the three principal stresses found according to the Von Mises approach.

$$\text{Triaxiality Factor (TF)} = \frac{\sigma_m}{\sigma_{eq}} = \frac{\frac{1}{3}(\sigma_{11} + \sigma_{22} + \sigma_{33})}{\sqrt{\frac{(\sigma_{11} - \sigma_{22})^2 + (\sigma_{22} - \sigma_{33})^2 + (\sigma_{33} - \sigma_{11})^2 + 6(\sigma_{12}^2 + \sigma_{23}^2 + \sigma_{31}^2)}{2}}}$$

The stress triaxiality is very important for the running of the virtual simulations, since it allows to consider a three-dimensional loading condition which is more similar to what happens in reality. The dog bone specimen has the lowest value of triaxiality, which is around 0.33, and the reason of its lowest value is due to the fact that the loads are monoaxially distributed.

3.2 Digital Image Correlation (DIC)

Digital Image Correlation (DIC) is the non-invasive technique used to extract the necessary data from the tensile tests performed on the three types of specimens. Because Digital Image Correlation is a non-contact technique that is independent of the material being tested or the length-scale of interest, it can be used in a wide variety of applications to investigate and characterize the deformation of solids, both in 2D and 3D. The bidimensional technique uses one camera only, which measures deformations that lie in a plane, that means that the specimen has to be planar. The biggest limit of the two dimensions methodology is attributable to the monocular vision of the single camera, known also as cyclopean vision, for the fact that the camera is not able to determine the size of the object tested. Due to this inconvenient, a 200% deformation of the specimen produces the same image as if the tested element was moved to one-half its original distance from the visual sensor of the camera. This is why there's the constraint of having a planar specimen, as well as the need to maintain the object at the same distance from the camera for the entire testing time **[49]**. In the three-dimensional approach, two or more cameras are used to evaluate the deformations, which can go outside the deformation plane considered in the 2D case. There are also 3D techniques called volumetric, which measures not only the deformations of the surface points, but also the deformations of the points inside the solid body analysed. Whatever is the applied case, before the measurements it is necessary to calibrate the camera lens. This step is fundamental to let the software adjust the images, to prevent the images distortion. The Digital Image Correlation technique overcomes the limits of the traditional way of stresses and strains measurements made by the classic strain gauges. The strain gauges are placed in the interested section of the specimen, and measures the variation in length of the material. The limit is that all the data related to the post-necking condition are lost, and a precise evaluation of the plastic behaviour is not possible to achieve. The Digital Image Correlation bases its measurements on the comparison between an image, or better if called *frame*, taken as reference, and another frame taken at a different instant in time. Each frame registered by the cameras is a set of pixels, every one of which is defined by a specific numeric code that represents the brightness level, if the picture is black and white, or the colour. The level of deformation is defined by the movement, and change in brightness, of the pixels, thru the intervention of a specific mathematical algorithm. To allow the surface elements of the specimen to be more visible by the cameras, the specimen is sprayed with a white paint, and then some small particles of black paint (called *speckles*) are applied on it randomly, but uniformly, all along the length, or at least all along the interested section. The movement of these speckles from the reference image to the observed, or actual one, defined the strains to which the specimen is subjected. The dimension of the black dots is very important for the precision of the final results. The best way to do the Digital Image Correlation process is to disperse the dots in order to have surface coverage of about 50% white and 50% black. Since the tracking of single points from image to image is very difficult to implement, those single points are considered inside a matrix of other points, that is called *subset*. So, the measurements of the deformations are done by tracking the movements of these subsets, as shown in **Figure 3.2 [50]**.

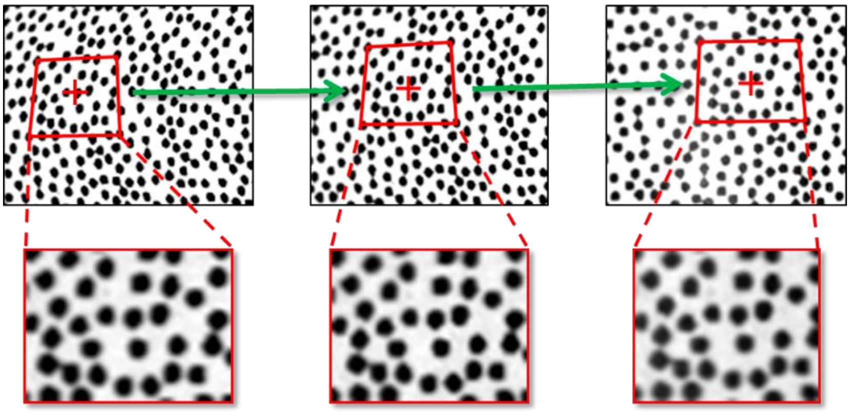

Figure 3.2: Movement of speckles in different frames

Each subset, as said before, is described by a specific code, which identifies the brightness level of each pixel of the subset. Usually, the cameras for Digital Image Correlation are based on 8 bits, so the black is represented with the code 0 (zero) and the white with the code 255, so the extremes of the 8-bit range. When the subset moves, also the numerical code moves inside the subset matrix, as depicted in **Figure 3.3 [51]**, where the 5x5 subset is represented by the red square.

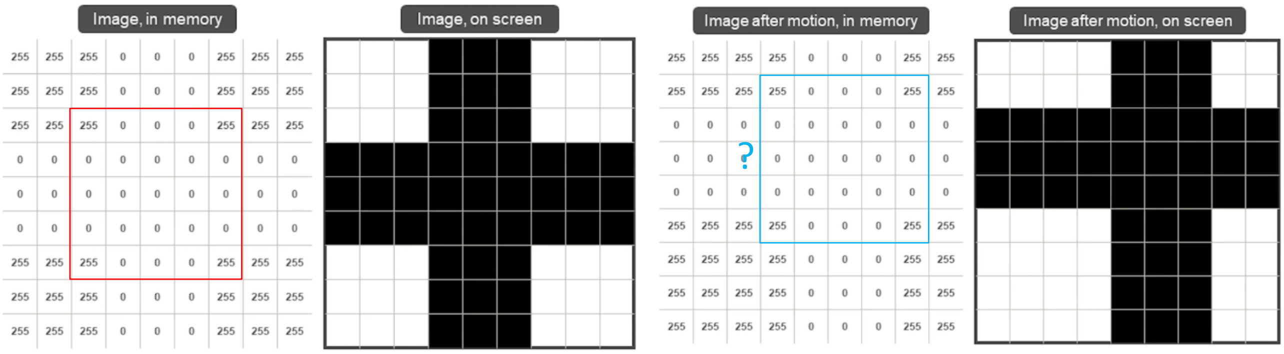

Image, in memory

255	255	255	0	0	0	255	255	255
255	255	255	0	0	0	255	255	255
255	255	255	0	0	0	255	255	255
0	0	0	0	0	0	0	0	0
0	0	0	0	0	0	0	0	0
0	0	0	0	0	0	0	0	0
255	255	255	0	0	0	255	255	255
255	255	255	0	0	0	255	255	255
255	255	255	0	0	0	255	255	255

Image after motion, in memory

255	255	255	255	0	0	0	255	255
255	255	255	255	0	0	0	255	255
0	0	0	0	0	0	0	0	0
0	0	?	0	0	0	0	0	0
0	0	0	0	0	0	0	0	0
255	255	255	255	0	0	0	255	255
255	255	255	255	0	0	0	255	255
255	255	255	255	0	0	0	255	255
255	255	255	255	0	0	0	255	255

Figure 3.3: Subset definition

In order to find the correct position of the subset in the following frame, a proper correlation function **C** is used (see the next page), which is based on the sum of the squared differences (SSD) of the pixel values. The smaller is the value of the sum of the squared differences, the better is the correlation. The process is repeated until the subset has been identified, that in other words means to find the lowest value of the SSD, which in the ideal case it is zero. However, in reality, the images are affected by noise, so it would be highly improbable that the image is perfectly described by combination of 0 and 255 only. The white would be not perfectly white, and the same happens for the black, so the image taken by the camera will be characterized by the presence of other numerical codes, such as 254, 253 and similar for white variations, and 1, 2 and similar for black variations.

n is the dimension of the subset

(n=5 in Figure 3.5)

Pixel value at (x+i, y+j)

Pixel coordinates, reference image

Image after motion

$$C(\overline{x,y},u,v)=\sum_{i,j=-n/2}^{n/2}\left[I(\overline{x+i,y+j})-I^{*}(\overline{x+u+i,y+v+j})\right]^{2}$$

[51]

Displacement from reference image

Image before motion

Pixel value at (x+u+i, y+v+j)

So, the path followed by the Digital Image Correlation technique is the one that provides, from the reference image to the next one and so on, the lowest value of the correlation function. The 3-dimensional Digital Image Correlation technique uses two sensors for the acquisition of the images, overcoming in this way the problem related to the monocular vision of the single camera. The recovering of the three-dimensional structure of the environment using two imaging sensors is called *stereo-triangulation*. This process requires to define the intersection point of the optical rays of the two cameras, in order to place correctly the specimen used for the tests. In turn, this operation requires the adequate calibration of the optical system. One important parameter that has to be properly calibrated is the stereo angle. The stereo angle is the angle formed by the optical rays of the cameras. Smaller stereo-angles lead to better in-plane displacement accuracy, at the cost of increased out-of-plane uncertainty. Alternatively, larger stereo-angles lead to better out-of-plane displacement accuracy, at the cost of increased in-plane uncertainty. This relationship between stereo-angle and uncertainty is also affected by the focal length of the lens. Shorter focal length lenses require a larger stereo-angle to obtain the same out-of-plane uncertainty as longer focal length lenses. The stereo-angle also affects the useable DOF. With smaller stereo-angles, the test piece will remain in focus in both cameras over a larger range of out-of-plane motions. Conversely, with larger stereo-angles, the allowable out-of-plane motion to keep the test piece in focus is reduced.

Another factor to choose carefully is the time frame. Increasing the time frame allows to have more precise measurements of the deformations, since more small movements of the subsets can be captured. Usually, the time frame set for the experiments is the maximum available of the cameras.

Concerning the resolution of the images, a higher resolution of course improves the quality, but also requires higher storage capacity, higher memory usage, and higher time requires for the transfer of images and data.

Variables such as lightning and exposition of the camera have also to be taken into account, particularly for the ability of detecting the brightness levels of the pixels of the subsets.

3.2.1 The extracted data

When the Digital Image Correlation equipment is properly calibrated, the tensile tests on the specimens can start. For every geometry of the specimens, the data extracted from the machine used to perform the tensile tests are the test time and the correspondent level of force achieved. The two types of data are combined together to obtained a graph of the force as a function of the testing time, until the failure of the specimen is reached. In this way we obtain a time-load dependency relation. The rupture time can be found by zooming the section of the graph in which the loads have a decreasing trend. At the same time, also information coming from the Digital Image Correlation are provided. In particular, there are information on the stress applied to the specimen and the correspondent level of strain reached on all the strain gauges. Also, there are also data about the frame rate of the camera, the camera registration time, and the correspondent time the test machine. These data are then collected together to perform the stress-strain analysis, and a graph with stress on the ordinate axis e strain on the abscissa axis is obtained, to draw the engineering curve of the material. The engineering curve of the material is computed for each strain gauge applied to the specimen. The time-load and the stress-strain analyses are done, and the graphs obtained are compared together to find which one of the three specimens is the most suitable one to be chosen as reference. To plot the graphs related to the time-load and stress-strain relationships, it is necessary to register the dimensions of the specimens. In **Figure 3.4** are shown summary information related to the geometry of the second dog bone specimen for QP1180 steel, included the information related to the failure.

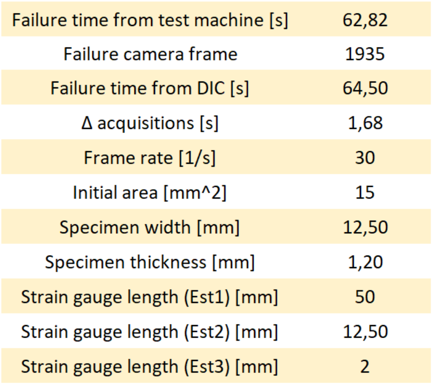

Failure time from test machine [s]	62,82
Failure camera frame	1935
Failure time from DIC [s]	64,50
Δ acquisitions [s]	1,68
Frame rate [1/s]	30
Initial area [mm^2]	15
Specimen width [mm]	12,50
Specimen thickness [mm]	1,20
Strain gauge length (Est1) [mm]	50
Strain gauge length (Est2) [mm]	12,50
Strain gauge length (Est3) [mm]	2

Figure 3.4: Summary data of second dog bone specimen

From the tensile test machine, it is possible to plot the diagram related to the time-load relationship (**Figure 3.5** and **Figure 3.7**). The data related to the failure of the object, in particular the failure time, can be found by zooming in the diagram in the area in which the load has a decreasing trend.

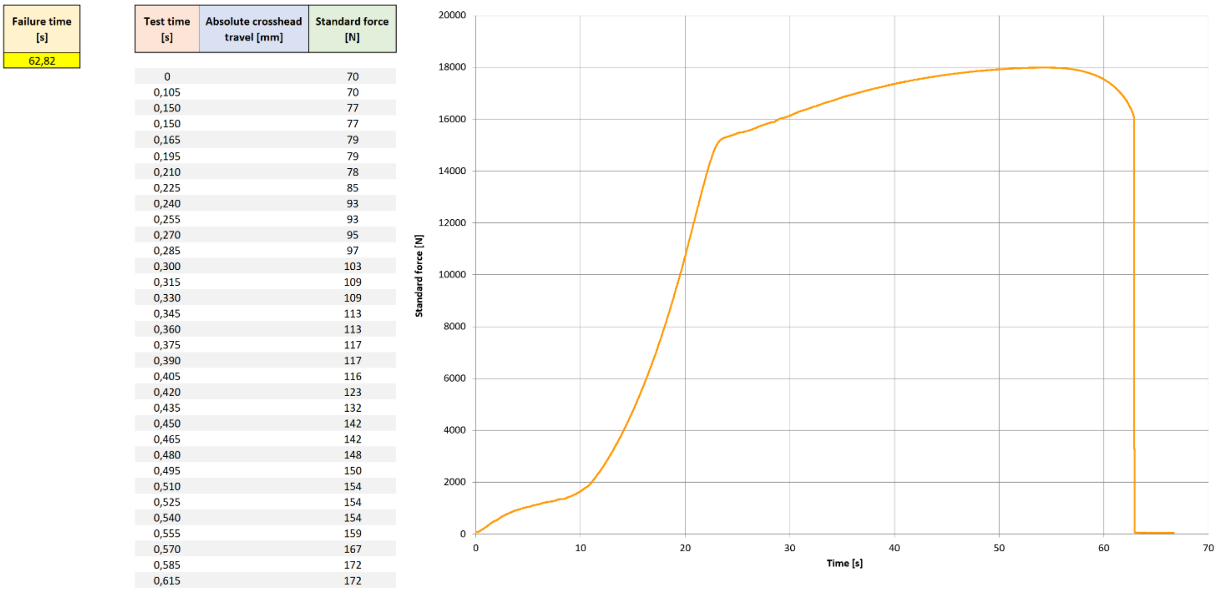

Failure time [s]
62,82

Test time [s]	Absolute crosshead travel [mm]	Standard force [N]
0		70
0,105		70
0,150		77
0,150		77
0,165		79
0,195		79
0,210		78
0,225		85
0,240		93
0,255		93
0,270		95
0,285		97
0,300		103
0,315		109
0,330		109
0,345		113
0,360		113
0,375		117
0,390		117
0,405		116
0,420		123
0,435		132
0,450		142
0,465		142
0,480		148
0,495		150
0,510		154
0,525		154
0,540		154
0,555		159
0,570		167
0,585		172
0,615		172

Figure 3.5: Time-load relationship of the second dog bone specimen

The tensile tests provide, as already said, information about the strains applied on the strain gauges, that in the Excel file are identified as **Eps x EST1**, **Eps y EST2**, and **Eps x EST3**. The first row of the table in **Figure 3.6** represents the failure data of the specimen, and the diagram obtained is the engineering curve of the material, i.e. the stress-strain relationship.

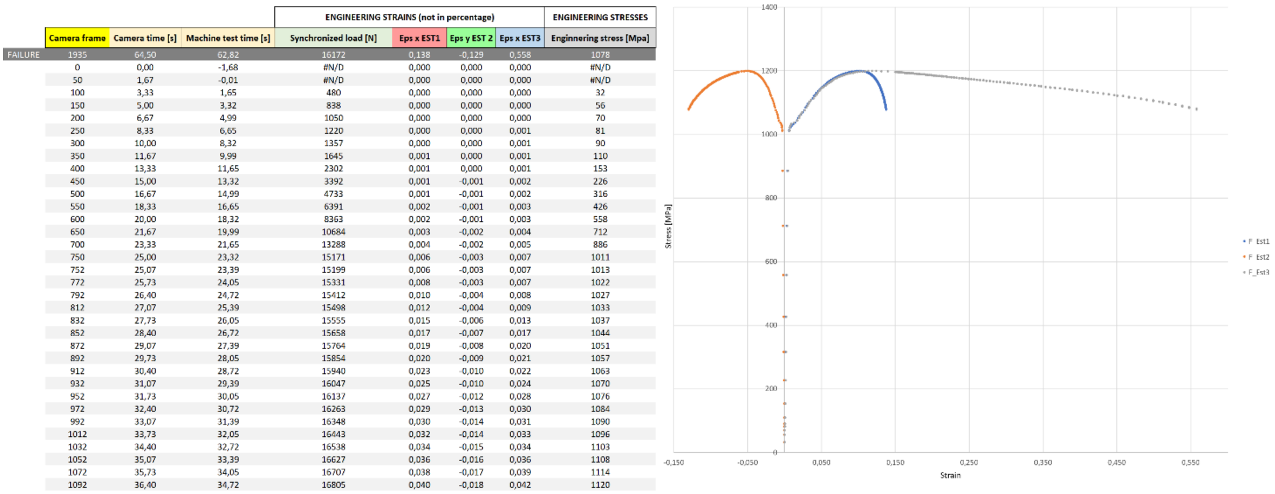

				ENGINEERING STRAINS (not in percentage)				ENGINEERING STRESSES
	Camera frame	Camera time [s]	Machine test time [s]	Synchronized load [N]	Eps x EST1	Eps y EST 2	Eps x EST3	Enginnering stress [Mpa]
FAILURE	1935	64,50	62,82	16172	0,138	-0,129	0,558	1078
	0	0,00	-1,68	#N/D	0,000	0,000	0,000	#N/D
	50	1,67	-0,01	#N/D	0,000	0,000	0,000	#N/D
	100	3,33	1,65	480	0,000	0,000	0,000	32
	150	5,00	3,32	838	0,000	0,000	0,000	56
	200	6,67	4,99	1050	0,000	0,000	0,000	70
	250	8,33	6,65	1220	0,000	0,000	0,001	81
	300	10,00	8,32	1357	0,000	0,000	0,001	90
	350	11,67	9,99	1645	0,001	0,000	0,001	110
	400	13,33	11,65	2302	0,001	0,000	0,001	153
	450	15,00	13,32	3392	0,001	-0,001	0,002	226
	500	16,67	14,99	4733	0,001	-0,001	0,002	316
	550	18,33	16,65	6391	0,002	-0,001	0,003	426
	600	20,00	18,32	8363	0,002	-0,001	0,003	558
	650	21,67	19,99	10684	0,003	-0,002	0,004	712
	700	23,33	21,65	13288	0,004	-0,002	0,005	886
	750	25,00	23,32	15171	0,006	-0,003	0,007	1011
	752	25,07	23,39	15199	0,006	-0,003	0,007	1013
	772	25,73	24,05	15331	0,008	-0,003	0,007	1022
	792	26,40	24,72	15412	0,010	-0,004	0,008	1027
	812	27,07	25,39	15498	0,012	-0,004	0,009	1033
	832	27,73	26,05	15555	0,015	-0,006	0,013	1037
	852	28,40	26,72	15658	0,017	-0,007	0,017	1044
	872	29,07	27,39	15764	0,019	-0,008	0,020	1051
	892	29,73	28,05	15854	0,020	-0,009	0,021	1057
	912	30,40	28,72	15940	0,023	-0,010	0,022	1063
	932	31,07	29,39	16047	0,025	-0,010	0,024	1070
	952	31,73	30,05	16137	0,027	-0,012	0,028	1076
	972	32,40	30,72	16263	0,029	-0,013	0,030	1084
	992	33,07	31,39	16348	0,030	-0,014	0,031	1090
	1012	33,73	32,05	16443	0,032	-0,014	0,033	1096
	1032	34,40	32,72	16538	0,034	-0,015	0,034	1103
	1052	35,07	33,39	16627	0,036	-0,016	0,036	1108
	1072	35,73	34,05	16707	0,038	-0,017	0,039	1114
	1092	36,40	34,72	16805	0,040	-0,018	0,042	1120

Figure 3.6: Engineering curve of the second dog bone specimen

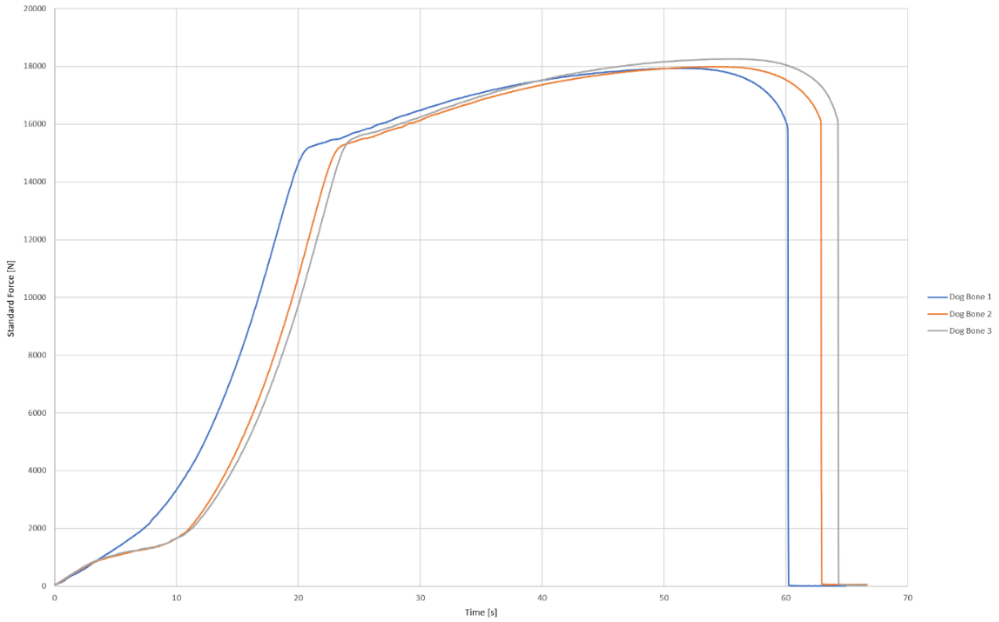

Figure 3.7: Dog bone specimens' behaviours in the time-load diagram

It is possible to note the great different in the trends of specimens 2 and 3 with respect to the first one. The last two dog bone specimens have similar behaviours, although a slight difference near the failure region. On the other way, the first specimen has a too far behaviour both in the elastic and in the plastic regions. Maybe the presence of impurities, or other defects inside the reticular structure, may have caused different reactions to same loads applied. Or, furthermore, the problem can be attributed to the sliding of the grips on the specimen during the execution of the tensile test. Strictly related to this time-load analysis, the specimen 1 is, with no doubts, excluded to be the one to take as reference. Since the other two specimens are very close to each other, it is necessary to perform the stress-strain analysis, to verify if the trend between the two is maintained, or if there are new divergences. **Figure 3.8** translates graphically these words. The figure in the next page represents the three engineering curves of all the three strain gauges of the second dog bone specimen. We can see now that what specimen 1 did in the time-load diagram is now replaced by the behaviour of specimen 3. The third specimen has a different plastic trend with respect to the other two specimens, and this difference increases as the testing time, and so the load, and hence the strain, increases. So, having in mind the two comparisons done in **Figure 3.7** and **Figure 3.8**, we can notice that the dog bone specimen 2 is the one which tends to remain between the trend of specimen 1 and the trend of specimen 3, so we can say that the trend of specimen 2 represents the average behaviour of the dog bone specimens. In other words, the dog bone specimen 2 is chosen as the reference specimen.

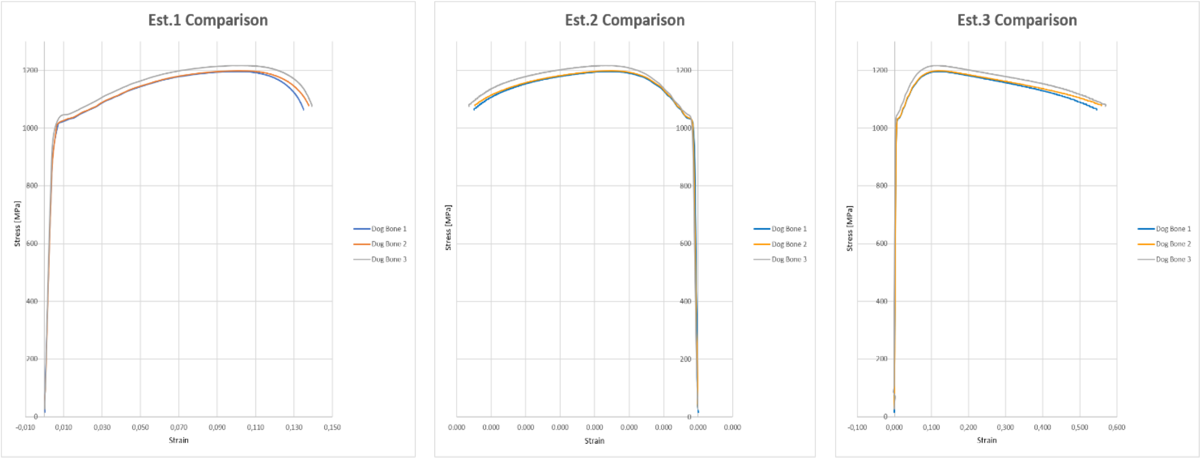

Figure 3.8: Dog bone specimens' behaviours in the stress-strain diagram

3.3 Engineering curve and True curve

The value of stresses and strains registered during the tensile tests are engineering stresses and engineering strains, so the curve stress-strain that is obtained is the engineering curve. An example is shown in **Figure 3.9** [52].

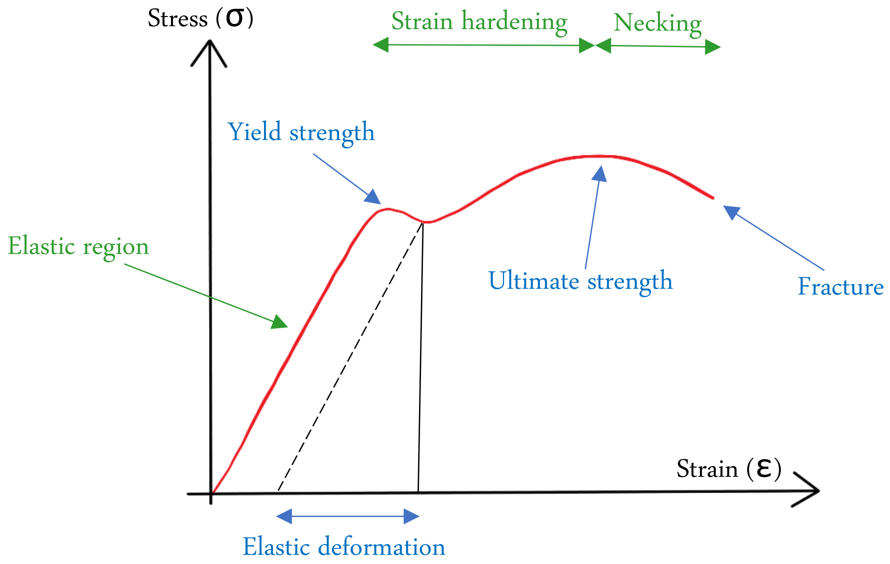

Figure 3.9: Example of an engineering curve from a tensile test

In a generic tensile test, the material is firstly subjected to an elastic and reversible elongation, which does not produce permanent deformations in the structure. Based on the type of material, the elastic region could be linear, such as the one in the figure, or not linear. In the linear case, the strains are proportional to the stresses, and their ratio is the elastic modulus of the material, also called Young modulus (E). In that linear region, the stress-strain relationship is ruled by the Hooke law ($\sigma = E * \varepsilon$). The elastic deformation continues until the maximum elastic elongation level, and so the yield stress, is reached. At this point, the material strength could drop, and the yielding process occurs. The plastic deformation is divided in two effects. The strain hardening effect goes from the onset of the yielding to the highest point of the engineering curve. In this phase, the strains increase as the load continues to go up, and the material strength increases as well. This strengthening effect occurs because of the dislocation movements and dislocation generation within the crystal structure of the material. The area of the specimen is continuously decreasing, but the biggest effects manifest when the highest point of the curve is reached, that coincides with the onset of the necking phenomenon. At this point, the area of the specimen starts to drastically reduce in a specific area, and the material undergoes to a drastic elongation, which prosecutes until the fracture.

The engineering stress is the ratio between the load and the initial area of the specimen, while the engineering strain is the ratio between the variation in length of the specimen with respect to its initial length. Initial area and initial length are always considered for the calculations of stresses and strains, and this is a limiting factor of the engineering curve. In particular, it is assumed that the area does not change.

$$\sigma_{\mathrm{engr}} = \frac{F}{A_0} \quad ; \quad \varepsilon_{\mathrm{engr}} = \frac{\Delta l}{l_0}$$

The engineering curve has to be corrected with the actual area, and the actual length of the specimen. In this way, more precise evaluations are done, and the curve obtained is the true curve.

$$\sigma_{\mathrm{true}} = \frac{F}{A_{\mathrm{eff}}} \quad ; \quad d\varepsilon_{\mathrm{true}} = \frac{dl}{l}, \quad \varepsilon_{true} = \int d\varepsilon_t$$

The mathematical relationships that allow to pass from engineering variables to true variables are the following ones **[53]**:

$$\sigma_{\mathrm{true}} = \sigma_{\mathrm{engr}} * (1 + \varepsilon_{\mathrm{engr}})$$

$$\varepsilon_{\mathrm{true}} = \mathrm{LN}(1 + \varepsilon_{\mathrm{engr}})$$

These formulas are valid before the necking condition, because after that point triaxiality state is present. After the onset of the necking, it is necessary to evaluate stresses and strains with 2D or 3D plastic model. This model bases its evaluations on the true stresses and on the true strains. See **Figure 3.10** **[54]** to see the difference between engineering curve and true curve.

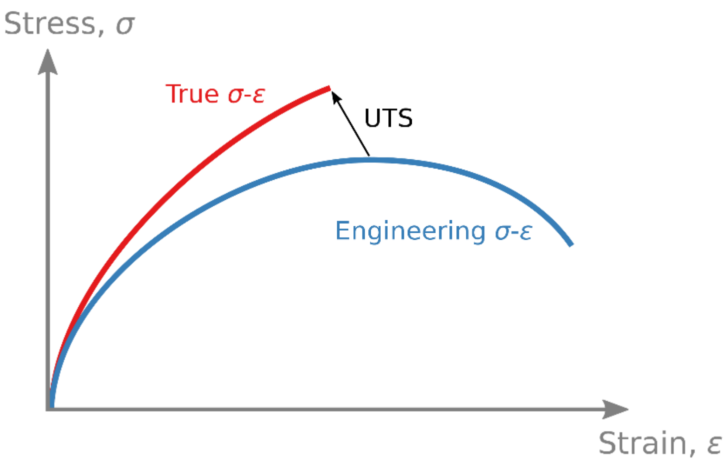

Figure 3.10: Engineering curve and true curve

The true curve is always a monotonically increasing function, and it is used to represent the stress-strain behaviour of the material up to a strain equal to 1, that means 100% of its deformation. In the elastic region, the true curve is identical to the engineering curve. After the necking point, the value of stresses and strains on the true curve are evaluated with a 3D plastic deformation model, also including a mathematical damage model. Since the true stresses and strains are identical to the engineering stresses and strains in the elastic region, the elastic deformation is not considered in the true curve, which has its starting point coinciding

Specimen 2 data up to necking		
ε engr	σ engr	
0,00000	0	Pt 1
0,00002	0	
0,00014	32	
0,00011	56	←
0,00021	70	
0,00030	81	←
0,00041	90	
0,00053	110	←
0,00073	153	
0,00101	226	
0,00137	316	←
0,00182	426	
0,00238	558	←
0,00310	712	
0,00415	886	Pt 1
0,00642	1011	Pt 2
0,00649	1013	←
0,00808	1022	
0,01019	1027	←
0,01224	1033	
0,01465	1037	Pt 2
0,01676	1044	
0,01854	1051	
0,02026	1057	
0,02260	1063	
0,02468	1070	
0,02690	1076	
0,02860	1084	
0,03013	1090	
0,03185	1096	
0,03410	1103	
0,03612	1108	
0,03827	1114	
0,04012	1120	
0,04195	1125	
0,04349	1131	
0,04545	1136	
0,04739	1141	
0,04957	1145	
0,05155	1149	
0,05369	1153	
0,05570	1157	
0,05754	1161	
0,05952	1165	
0,06132	1168	
0,06338	1172	
0,06533	1175	
0,06742	1177	
0,06965	1180	
0,07179	1182	
0,07385	1184	
0,07615	1187	
0,07822	1189	
0,08052	1191	
0,08261	1192	
0,08493	1193	
0,08704	1195	
0,08938	1196	
0,09153	1197	
0,09395	1198	
0,09612	1198	
0,09850	1199	
0,10104	1199	
0,10338	1199	
0,10605	1199	

with the yielding initiation point. So, referring to the followed procedure, all the data extracted from the testing machine which are after the necking point are eliminated, since they have to be evaluated with a damage model. These data are engineering data. Subsequently, the elastic deformation has to be neglected, hence the values of strains are subtracted by the elastic deformation visible in **Figure 3.9**. As already said, the elastic deformation is evaluated with the Hooke law, so the plastic component of the strain is determined by the following mathematical formula:

$$\varepsilon_{\mathrm{engr\ (plastic)}} = \varepsilon_{\mathrm{engr}} - \frac{\sigma_{\mathrm{engr}}}{\mathrm{E}}$$

At this point, we have values of stresses and strains that go from the yielding point, i.e. the beginning of plastic deformation, to the necking condition. When the plastic region is reached, the strains become positive. The initial point of the plastic true curve is identified by the value of plastic strain equal to zero and its correspondent value of stress, and it's highly probable that in the data now obtained there's no presence of an exact zero value of plastic strain. To find the maximum value of stress which corresponds to a plastic strain equal to zero, or yielding point, it is necessary to do an interpolation between the elastic zone and the plastic region. To do that, a graph is drawn, by taking some data in the elastic region and some data in the plastic region. After that, the two relative tendency lines are plotted, and their equations are put in evidence. The solution of this system of equations corresponds to the intersection point, hence the initial point of the true curve.

Let's have a look at how the true curve for the QP1180 steel has been determined. In the table on the left you can see the selected engineering data points up to the necking condition, highlighted in red. These points represent the points of the engineering curve, so the engineering strains and the engineering stresses. To find the initial point of the true curve, these points have to be subtracted of the elastic part, obtaining the data points visible in the table on the next page.

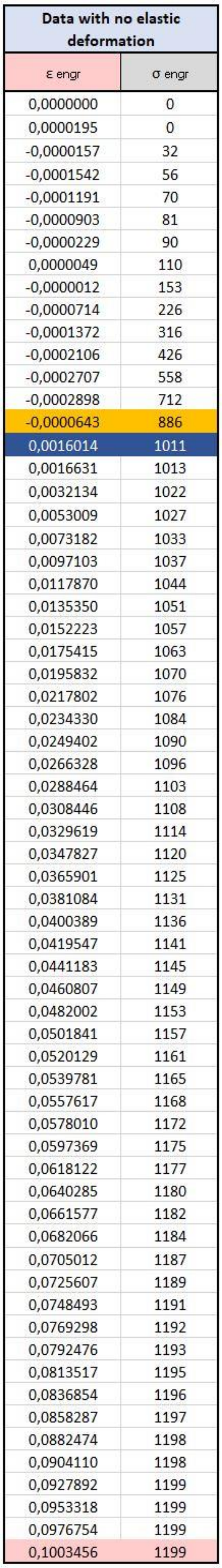

Data with no elastic deformation	
ε engr	σ engr
0,0000000	0
0,0000195	0
-0,0000157	32
-0,0001542	56
-0,0001191	70
-0,0000903	81
-0,0000229	90
0,0000049	110
-0,0000012	153
-0,0000714	226
-0,0001372	316
-0,0002106	426
-0,0002707	558
-0,0002898	712
-0,0000643	886
0,0016014	1011
0,0016631	1013
0,0032134	1022
0,0053009	1027
0,0073182	1033
0,0097103	1037
0,0117870	1044
0,0135350	1051
0,0152223	1057
0,0175415	1063
0,0195832	1070
0,0217802	1076
0,0234330	1084
0,0249402	1090
0,0266328	1096
0,0288464	1103
0,0308446	1108
0,0329619	1114
0,0347827	1120
0,0365901	1125
0,0381084	1131
0,0400389	1136
0,0419547	1141
0,0441183	1145
0,0460807	1149
0,0482002	1153
0,0501841	1157
0,0520129	1161
0,0539781	1165
0,0557617	1168
0,0578010	1172
0,0597369	1175
0,0618122	1177
0,0640285	1180
0,0661577	1182
0,0682066	1184
0,0705012	1187
0,0725607	1189
0,0748493	1191
0,0769298	1192
0,0792476	1193
0,0813517	1195
0,0836854	1196
0,0858287	1197
0,0882474	1198
0,0904110	1198
0,0927892	1199
0,0953318	1199
0,0976754	1199
0,1003456	1199

In this way, the elastic part of the curve is represented by negative values, while the plastic part of the curve is represented by positive values. The change between negative and positive values locates the initial point of the true curve, i.e. the yielding point. It is that point which defines the yellow and blue blocks data selection of the previous page, which in turn allow to represent the engineering curve with two lines with different slope. The intersection point between the two tendency lines defines the initial point of the true curve, as visible in **Figure 3.11**. The second point of the true curve is represented by the blue line in the data set on the left, and all the other values below it are all the remaining points.

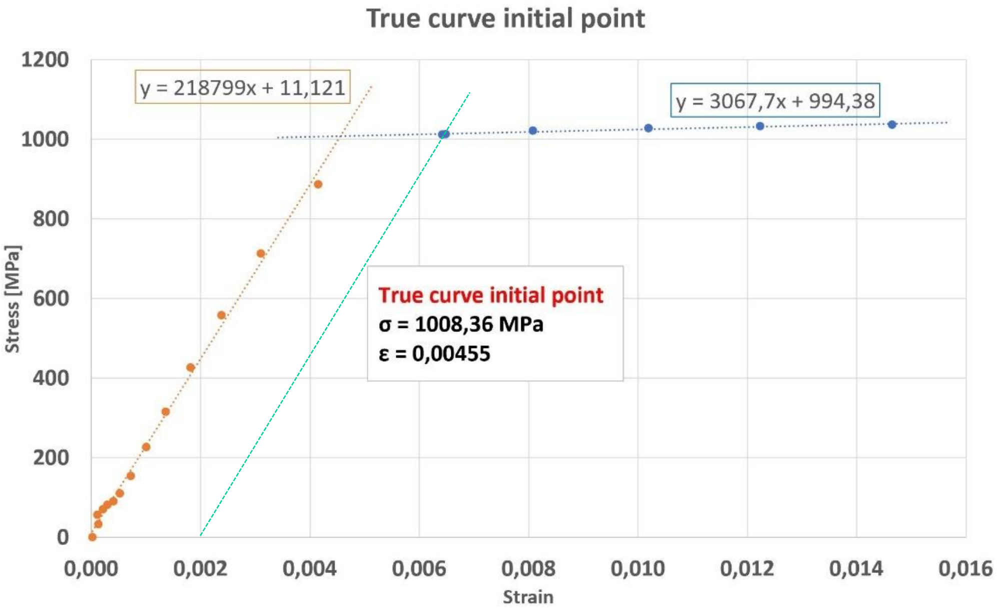

Figure 3.11: Evaluation of the true curve initial point

As can be seen, the initial point is set for σ = 1008.36 MPa and ε = 0.00455, hence the first point of the true curve corresponds to σ = 1008.36 MPa and ε = 0. The classical method of the yielding offset at 0.2% is not preferred here because of potential problems that could arise during the execution of the tensile tests. If the specimen slips in the grips, or if there is extensometers slippage, there could be non-linearities or discontinuities in the stress – strain curve, and the 0.2% offset method could lead to an erroneous evaluation of the yield strength.

Having found the first point of the true curve, it is necessary to transform the engineering value of stresses and strains into the correspondent true values. This can simply be achieved by applying the mathematical relation at page 70 which relates the engineering values to the true values. Finally, the true curve can be plotted. In **Figure 3.12** you can see the true curve obtained for the QP1180 steel.

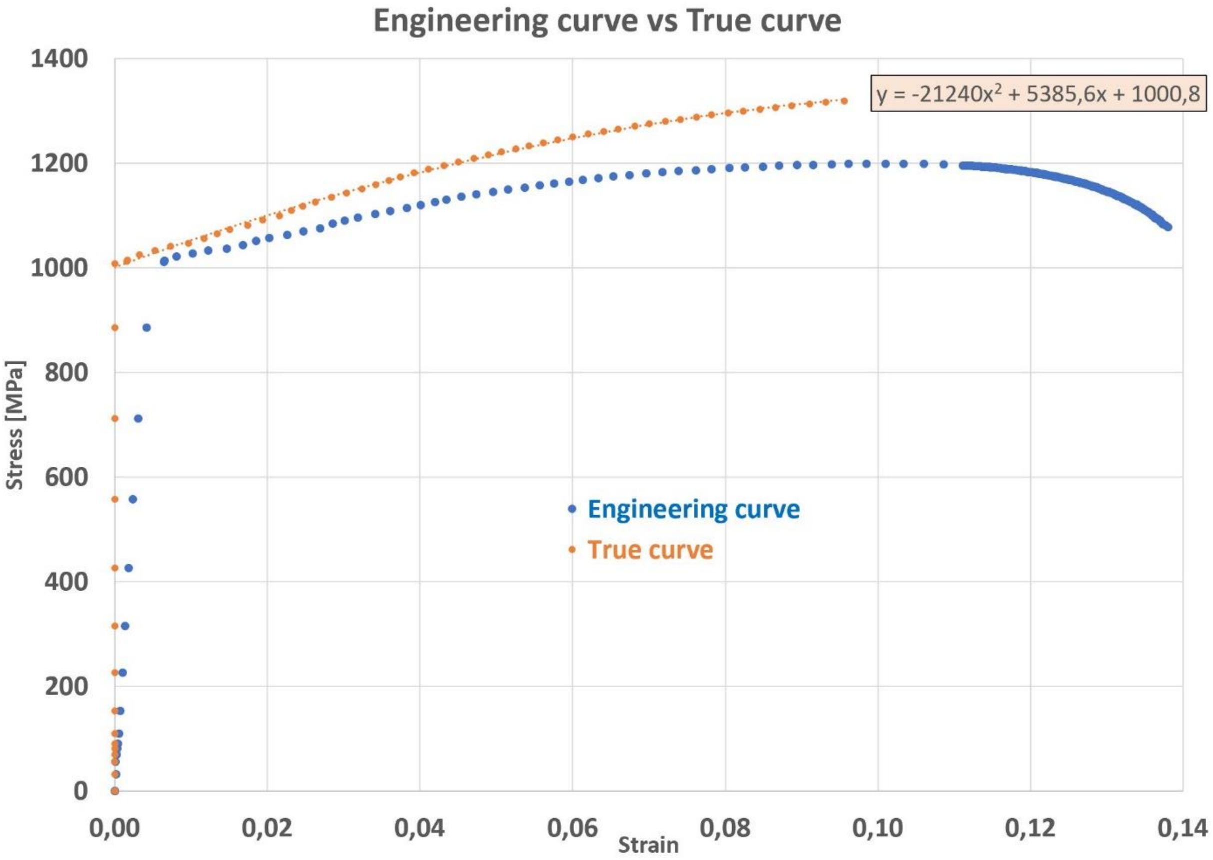

Figure 3.12: True curve obtained for QP1180 steel

Now, to evaluate the plastic behaviour after the necking point and to perform the virtual simulations, it's necessary to fit the true curve so obtained with the estimating mathematical models described in chapter 2.

3.4 Results

In this chapter we will see the application of the true curve estimation models previously described in Chapter 2. The aim of this implementation is to discover which is the model which best approximates the behaviour of the true curve obtained from experimental data. Also, it is needed to have an idea on how each model describes the material behaviour after the onset of the necking condition. The curves have been obtained and optimized by the Sum of Squared Residuals (SSR) method. In particular, the mathematical formulation adopted to obtain the best approximated curve is here expressed:

$$SSR = \sum_{i=1}^{n} (y_i - x_i)^2$$

in which n is the total amount of the data set of the estimated curve, y_i is the value of stress from the true curve, and x_i is the value of stress obtained from the estimation model used. The aim is to find the best values of the models' parameters able to minimize the SSR variable. To do that, the solver of Excel has been used. It requires to select the value of the SSR variable, and to select the parameters in the approximation model to find their optimum combination.

The curve fitting procedure is essential for the software virtual simulations. It requires monotonically increasing functions for performing the Finite Element simulations, and they are provided by the models described so far. These increasing monotonically curves avoid the oscillations of the stresses that can be registered during the real test execution, and which can cause problems or errors during the FEM simulations.

The application of the estimation models is firstly done for the reference material, the QP1180 steel, and then for other materials, to verify the correctness of execution and validity of the models adopted. In particular, the other steels considered are the DP980 Usiminas, the QP980 Baosteel, and the TBC1180 Thyssen.

3.4.1 QP1180 steel

The QP1180 steel is suitable for automotive applications, since they have excellent mechanical properties and guarantee high safety in case of crashes.

Table 4 [55] shows the general composition of QP steel, **Table 5** [55] the mechanical characteristics of QP1180.

C	Mn	Si	Al	P	S
0.15 – 0.30	1.5 – 3.0	1.0 – 2.0	0.02 – 0.06	<0.015	<0.01

Table 4: General chemical composition of QP steels

Yield strength [MPa]	Tensile strength [MPa]	Elongation [%]
990	1180	20 (min)

Table 5: Mechanical properties of QP1180 steel

Hollomon law

In **Figure 3.13** it is possible to see the estimation of the true curve made by the Hollomon law model in relation with the true curve itself. The curve has been obtained by the optimal combination of $\boldsymbol{K} = 1565{,}9\ MPa$ and $\boldsymbol{n} = 0{,}082$. As it's visible, the estimation is not so well precise, since the deviations are particularly high in the initial part of the curve. In detail, the points of the estimated curve reach a maximum data divergence of 13.8% in the positive region, i.e. where the estimated curve is positioned above the true curve, and a maximum data divergence of about 9.0% in the negative region, i.e. where the estimated curve is positioned under the true curve. The percentage values of data divergence have been found by evaluating the difference, point by point, between the estimated stress value and the true stress value, then these differences have been divided by the true curve data interval, defined by the difference between the maximum true stress value and the minimum true stress value. The Hollomon curve has a different trend, clearly visible in the figure, which does not precisely replicate the trend of the true curve.

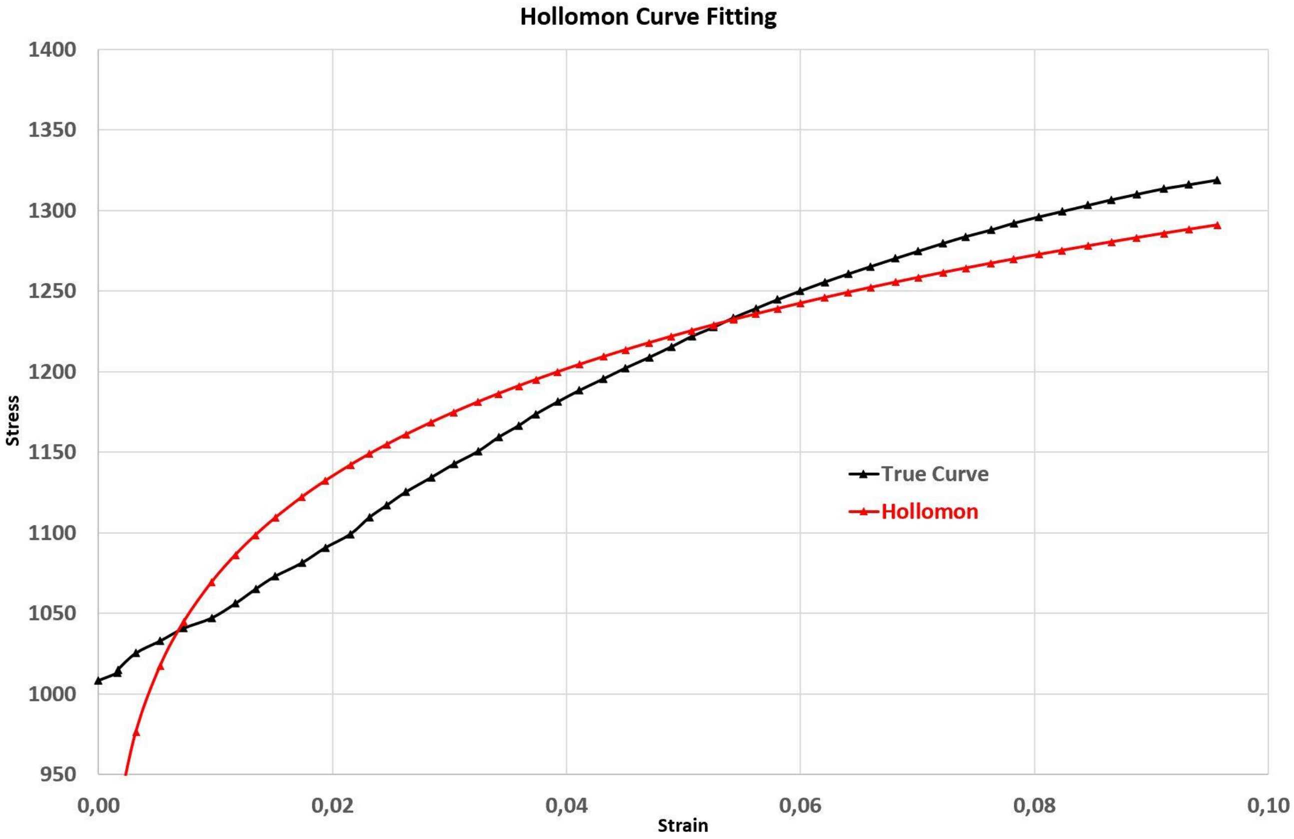

Figure 3.13: Estimated curve obtained by the Hollomon model

Ludwik model

The minimization of the SSR variable for the Ludwik model is achieved for $\boldsymbol{K} = 1814{,}0\ MPa$, $\boldsymbol{n} = 0{,}702$ and $\boldsymbol{A} = 988{,}7\ MPa$.

The Ludwik estimated curve is better than the Hollomon estimated curve. In this case, the stresses evaluated from the Hollomon model are added by a specific constant, which optimum value is determined by the solver of Excel. As it is visible in **Figure 3.14**, the points obtained from the Ludwik model are visibly nearer to the true curve in both the positive and negative regions, with respect to the points obtained from the Hollomon model. Also, the data divergences are reduced, stopping at a value of about 6.0% in both the regions.

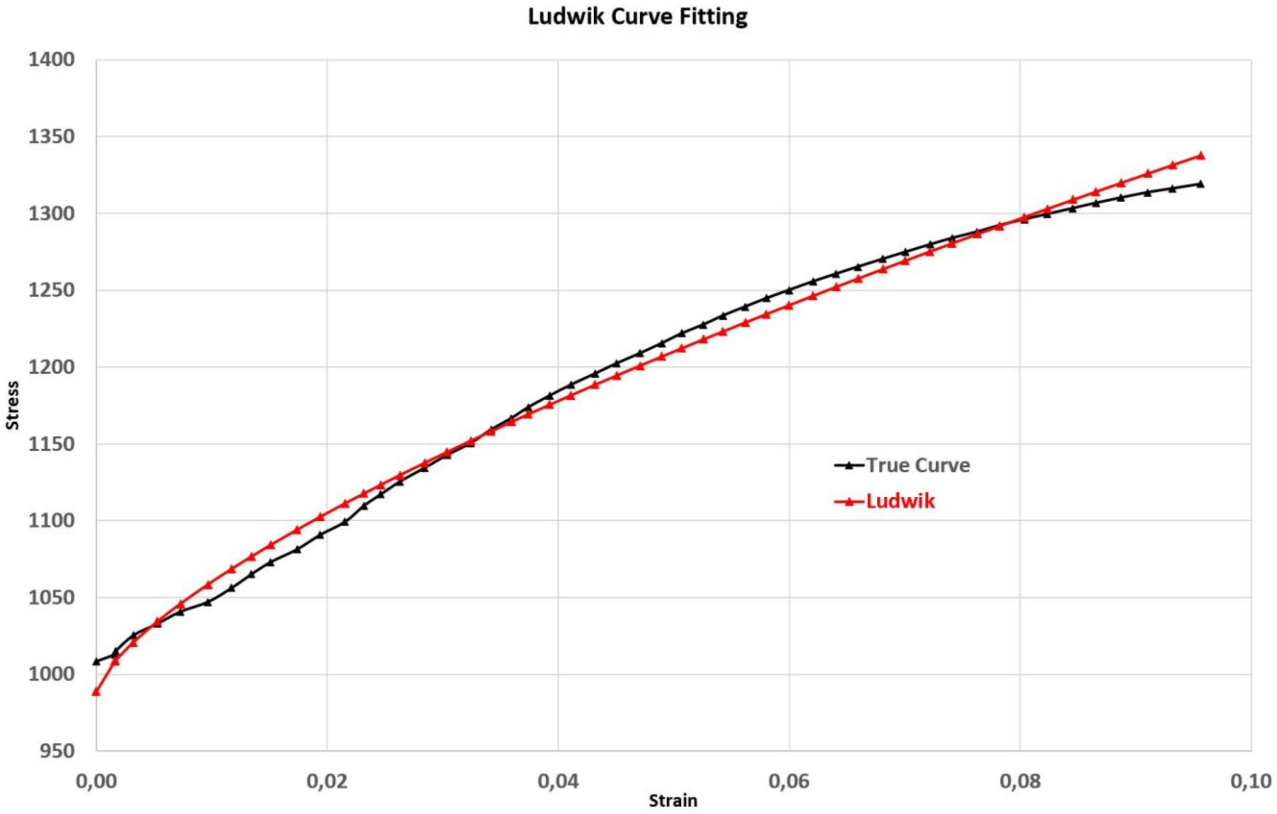

Figure 3.14: Estimated curve obtained by the Ludwik model

El Magd estimation

The parameters of the El Magd model are $\boldsymbol{A} = 987{,}2\ MPa$, $\boldsymbol{\beta_1} = 0{,}5\ MPa$, $\boldsymbol{\beta_2} = 12{,}0$ and $\boldsymbol{K} = 480{,}5\ MPa$. The El Magd estimated curve is way more precise with respect to the ones seen so far. It could seem, looking at **Figure 3.15**, that this model is the better one able to nearly perfectly suits the true curve. With respect to all the other models, the El Magd formulation is characterized by the lowest data divergence, which is half the data divergence registered in the Ludwik estimating model, and so about 2.9% in both the positive and negative regions.

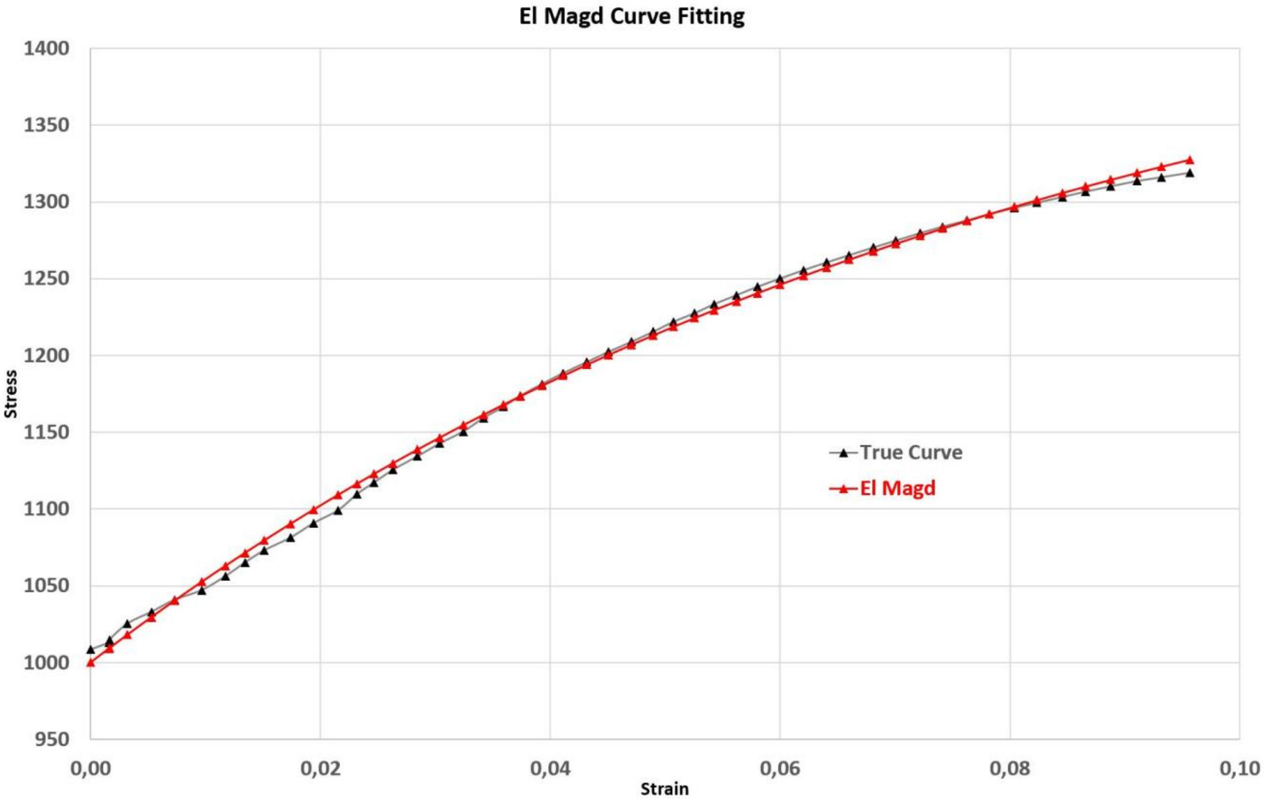

Figure 3.15: Estimated curve obtained by the El Magd model

Swift & Voce estimation

The Swift & Voce estimated curve is similar to the El Magd estimated curve. In particular, it has been obtained by assigned $\boldsymbol{\alpha} = 0{,}75$, so the greatest contribution is provided by the Swift component. Its parameters are $\boldsymbol{K} = 1657{,}3\ MPa$, $\varepsilon_0 = 0{,}033$ and $n = 0{,}149$, while the Voce parameters are $\boldsymbol{k_0} = 1001{,}2\ MPa$, $\boldsymbol{Q} = 1034{,}7\ MPa$ and $\boldsymbol{\beta} = 10{,}5$. The trend is nearly identical, but near the necking region the stresses are higher in the Swift and Voce curve with respect to the ones of the El Magd curve (see **Figure 3.16**). Indeed, the data divergence is oscillating around 3%, like happens in the El Magd model, while in the necking area the divergence is set at about 4.6%.

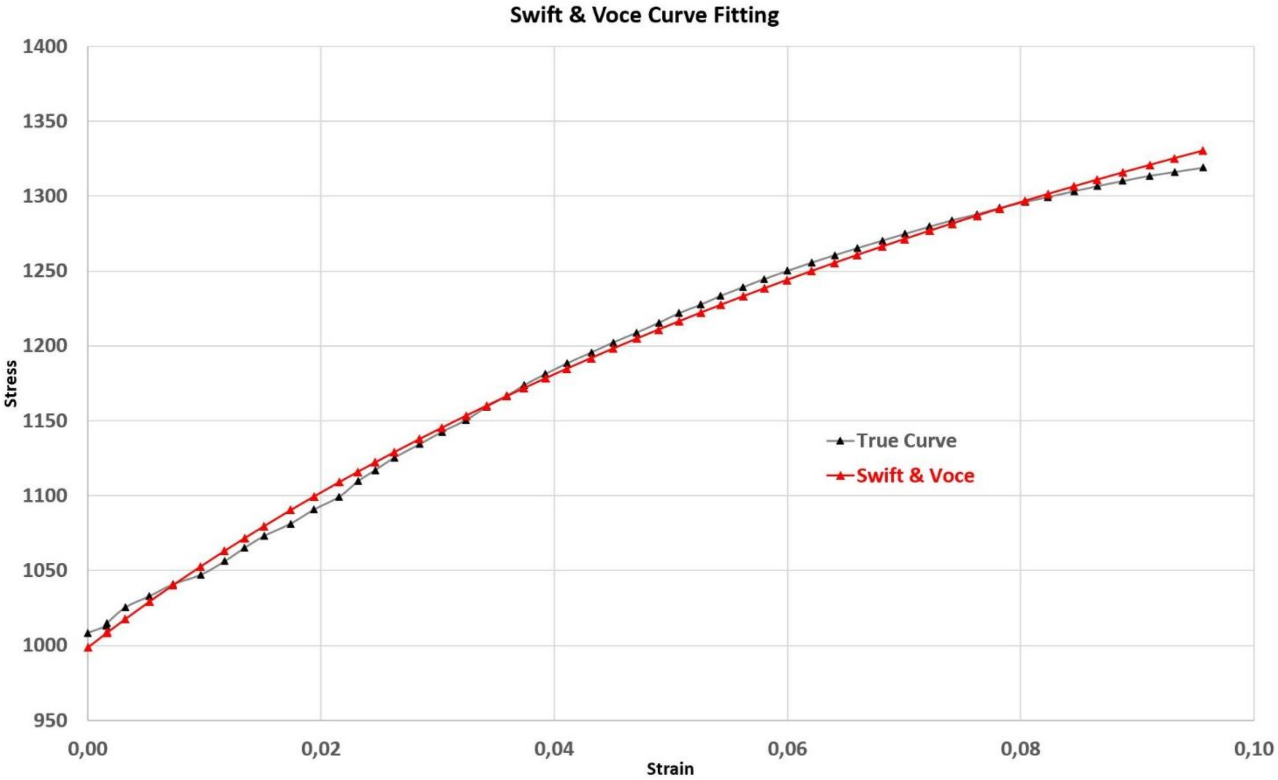

Figure 3.16: Estimated curve obtained by the Swift & Voce model

MLR estimation

The MLR estimation methodology is principally used for estimating the material behaviour after the necking condition, to values of strain up to 100% of deformation. The parameters for the post-necking analysis are $\boldsymbol{S_0} = 1194{,}6\ MPa$ and $\boldsymbol{S_1} = 1008{,}4\ MPa$. As can be seen in the description of section 2.4.5, this estimation model is applied after the strain at necking is reached. Before this point, the Hollomon law is valid, and so the approximation of the true curve is the same obtained from the Hollomon law, and the same are also the values of the model parameters. Consequently, the deviations reach values up to 14% in the positive region, and about 9% in the negative region. The graph of the true curve compared to the estimated curve is not reported, since it is the same as the one that appears in **Figure 3.13**. Instead, what is important is the after-necking behaviour described by this methodology, and it can be seen in the following page in **Figure 3.17**.

Bridgman estimation

For the Bridgman estimation model, the situation is the same as the one seen for the MLR estimation model. The Bridgman estimation model establish the behaviour of the steel after the onset of the necking phenomenon, while the points in the pre-necking area are establish, again, by the Hollomon prediction model. The variables for the post-necking behaviour are $\boldsymbol{B_0} = 1194{,}6\ MPa$, $\boldsymbol{B_1} = 1008{,}4\ MPa$ and $\boldsymbol{B_2} = -96{,}4\ Mpa$. In **Figure 3.17** it is possible to notice of the Bridgman methodology, compared to all the other ones, could be the least precise and reliable one, since a not well continuous trend of the stress can be found through the optimization method of the Sum of Squared Residuals. Also, the curvature of the line is very little rounded, with a prevalence of a nearly linear trend.

To conclude, **Figure 3.17** summarizes the post-necking behaviour of the QP1180 steel obtained by all the different estimation models previously described. It can be notice that the El Magd and Swift and Voce estimating models are the best ones, because they provide the lowest data divergences with respect to the data points of the true curve. However, the El Magd model seems to be the most precise one, since its points remain at the lowest distance to the true curve with respect to what happen in all the other estimating models. Notice also how the El Magd and Swift and Voce models provides curves which start very near to the true curve, while the Hollomon and Ludwik models present some strain divergence, particularly for the former-

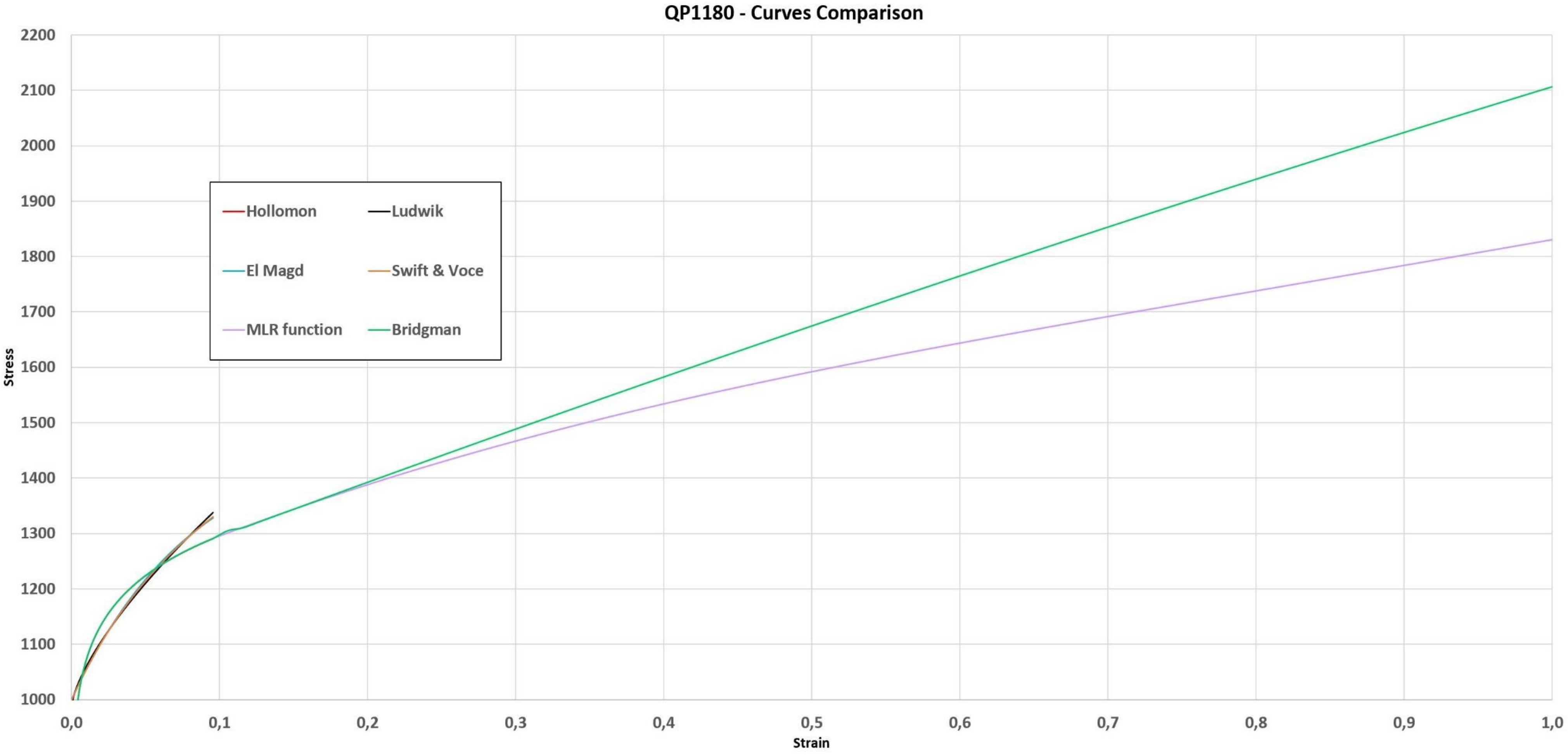

Figure 3.17: Post-necking behaviour of QP1180 steel with the different estimation models

3.4.2 DP980 Usiminas

Usiminas is a leading producer of flat steels in the Americas, providing a wide variety of commercial steels, included the last generation of Advanced High Strength Steels (AHSS). The one chosen for our analysis is, indeed, the DP980. The DP abbreviation stands for Dual Phase, the specific class of steels described in Chapter 1. The term dual phase is related to steel microstructure, which is predominantly formed by islands of a hard martensitic phase, dispersed in a ferrite matrix. The presence of these constituents, and their respective volumetric fractions in the microstructure, directly influences the mechanical properties of these steels. This structure provides excellent ductility, high strain hardening, (WH effect – work hardening) and painting cure (BH effect – bake hardening effect). The DP980 is especially recommended in the automotive industry for structural and reinforcement parts, providing weight reduction through thickness reduction. They have exceptional impact absorption capacity due to their high ductility/resilience. However, the lower mechanical grades can be applied in cover panels of vehicles with noteworthy denting resistance. **Table 6 [56]** and **Table 7** [56] show, respectively, the chemical and mechanical properties of DP980. **Figure 3.6** graphically summarizes the approximations of the true curve obtained with all the models, while **Figure 3.18** compares the post-necking behaviour of all the different estimation models.

C	Mn	Si	P	S
0.23 (max)	3.30 (max)	2.00 (max)	0.09 (max)	0.04 (max)

Table 6: Chemical composition of DP980 Usiminas

Yield strength [MPa]	Tensile strength [MPa]	Elongation [%]
550 – 730	980 (min)	8 (min)

Table 7: Mechanical properties of DP980 Usiminas

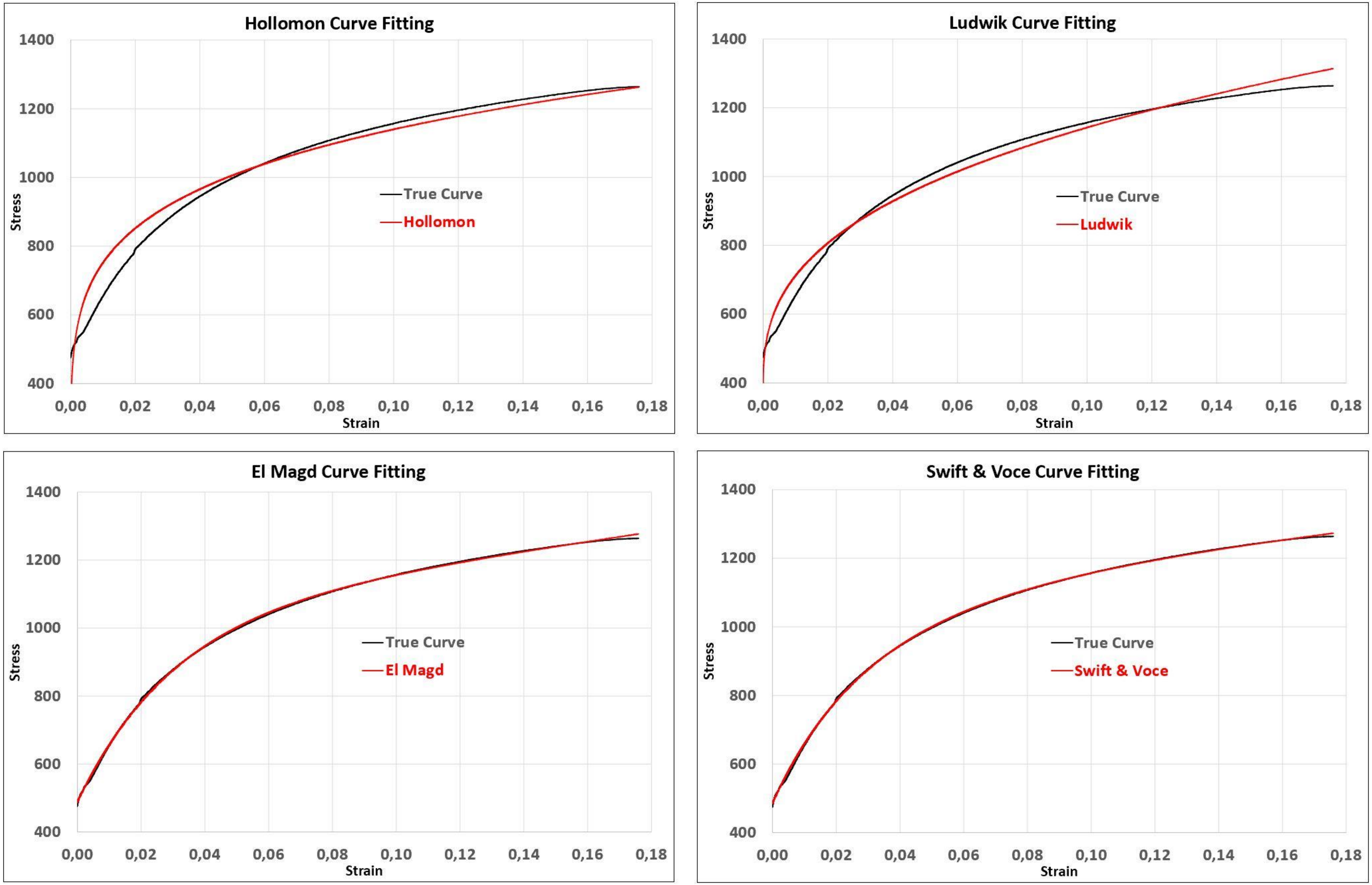

Figure 3.18: Estimated curves for the DP980 Usiminas steel

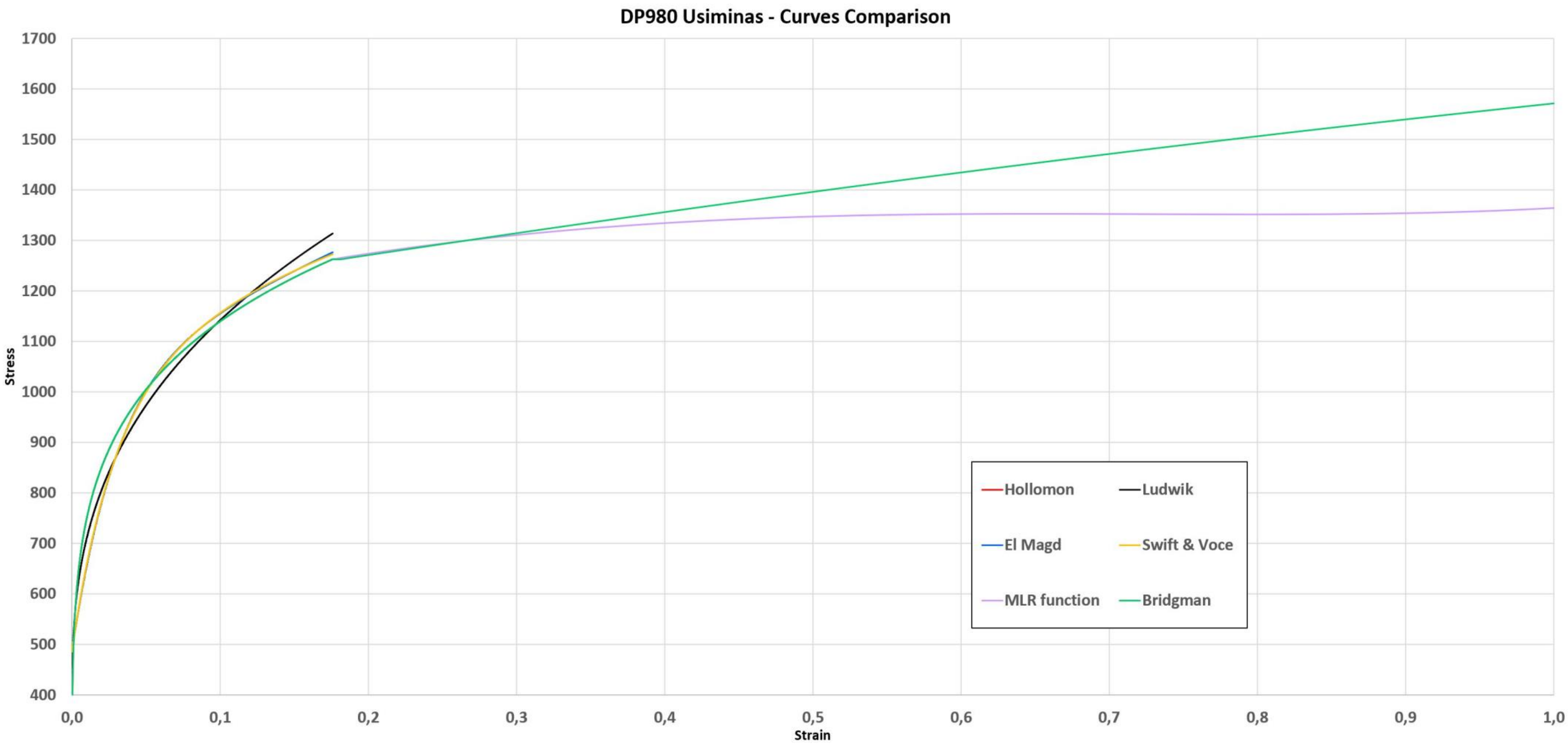

Figure 3.19: Post-necking behaviour of DP980 Usiminas steel with different estimation models

Before giving an overall discussion on the results, now are reported all the values of the models' variables.

The **Hollomon** curve has been drawn by the combination of $\boldsymbol{K} = 1731{,}1\ MPa$ and $\boldsymbol{n} = 0{,}182$.

The **Ludwik** curve has been obtained by using $\boldsymbol{K} = 1749{,}5\ MPa$, $\boldsymbol{n} = 0{,}356$ and $\boldsymbol{A} = 371{,}3\ MPa$.

The **El Magd** model variables are $\boldsymbol{A} = 475{,}1\ MPa$, $\boldsymbol{\beta_1} = 1344{,}2\ MPa$, $\boldsymbol{\beta_2} = 32{,}8$, and $\boldsymbol{K} = 554{,}6\ MPa$.

The **Swift and Voce** curve has been obtained by assigning $\boldsymbol{\alpha} = 0{,}70$, so giving to the Swift component more importance. Its parameters are $\boldsymbol{K} = 1941{,}1\ MPa$, $\boldsymbol{\varepsilon_0} = 0{,}017$, and $\boldsymbol{n} = 0{,}252$.
The Voce related parameters are $\boldsymbol{k_0} = 2{,}3\ MPa$, $\boldsymbol{Q} = 1251{,}2\ Mpa$ and $\boldsymbol{\beta} = 35{,}6$.

For the post-necking analysis, the **MLR** curve is characterized by $\boldsymbol{S_0} = 1179{,}0\ MPa$ and $\boldsymbol{S_1} = 476{,}0\ Mpa$, while the **Bridgman** curve is set for $\boldsymbol{B_0} = 1179{,}0\ MPa$, $\boldsymbol{B_1} = 476{,}0\ MPa$ and $\boldsymbol{B_2} = -83{,}8\ MPa$.

The El Magd and the Swift and Voce estimating models are the ones able to best fit the true curve although, contrarily to what seen for the QP1180, the Swift and Voce law is the most precise between the two. Indeed, you can see in Figure 3.18 how the deviation from the true curve, near the necking region, is slightly lower in the Swift and Voce model than in the El Magd model.

The Ludwik model provides the similar trend seen previously in the QP1180 steel, with some positive and negative deviations along the true curve, while the Hollomon models provides an improved behaviour with respect to the previous case. Now, the estimated curve is located nearer to the true curve, although some positive divergence remains in the initial section, but this is a characteristic of the Hollomon model.

Looking now at Figure 3.19, it is visible how the Hollomon model and the Swift and Voce model provides very similar behaviours in the post-necking region, although their approximations in the pre-necking region are completely different. Same considerations for the MLR function model, which is based on the Hollomon model. Instead, despite the very similar approximations between the El Mag and Swift and Voce models, their behaviours in the post-necking region are very different. The continuous reduction of estimated stress as the strain increases is much less pronounced in the El Magd model, which registers a value of stress up to 2400 N with respect to about 1700 N registered by the Swift and Voce model, at 100% of deformation. Similar consideration is valid also for the Ludwik estimating model, where the higher estimated stresses in the post-necking area can be easily predicted by looking at the true curve approximation in Figure 3.18. Final consideration is made on the Bridgman estimating method. The pre-necking approximation is the same as the Hollomon approximation, but the post-necking behaviour provides the lowest value of estimated stresses among all the other observed estimating models.

3.4.3 QP980 Baosteel

Baosteel Group Corporation is a Chinese company specialized in the production of carbon steel, stainless steel, and advanced special steel, widely applicable in many industrial sectors, such as automobile, household appliances, petrochemical, machinery, energy, transportation, metalwork, and aeronautics. Concerning the automotive applications, the QP980 steel is suitable for automotive safety parts and structural parts with complex shapes. 980MPa grade QP steel is the first "world –first" selling product of Baosteel. At present, it has been commercially supplied for the manufacturing of the parts of many domestic models, such as B-pillar reinforcement, A-pillar reinforcement and hinge pillar reinforcement. This B-pillar reinforcement is located between the side wall outer plate and the B-pillar inner panel, which is an important part of the B-pillar, which could improve the strength and impact performance of the B-pillar. Generally, the B-pillar reinforcements are made of HSS or UHSS sheets with high formability. The A-pillar is the main part supporting the structure of the vehicle between the engine compartment and the cockpit, and it is a fundamental component for passengers' protection. For the A-pillar inner, the QP980 steel can well meet the formability requirements, and improve the strength of the part, the rigidity of the A-pillar, the weight reduction, vision blind area reduction, and the driving safety.

Table 8 [57] and **Table 9** [57] show, respectively, the chemical and mechanical properties of QP980. **Figure 3.20** graphically summarizes the approximations of the true curve obtained with all the models, while **Figure 3.21** compares the post-necking behaviour of all the different estimation models.

C	Mn	Si
0.25 (max)	2.50 (max)	2.00 (max)

Table 8: Chemical composition of QP980 Baosteel

Yield strength [MPa]	Tensile strength [MPa]	Elongation [%]
650 – 800	980 (min)	20 (min)

Table 9: Mechanical properties of QP980 Baosteel

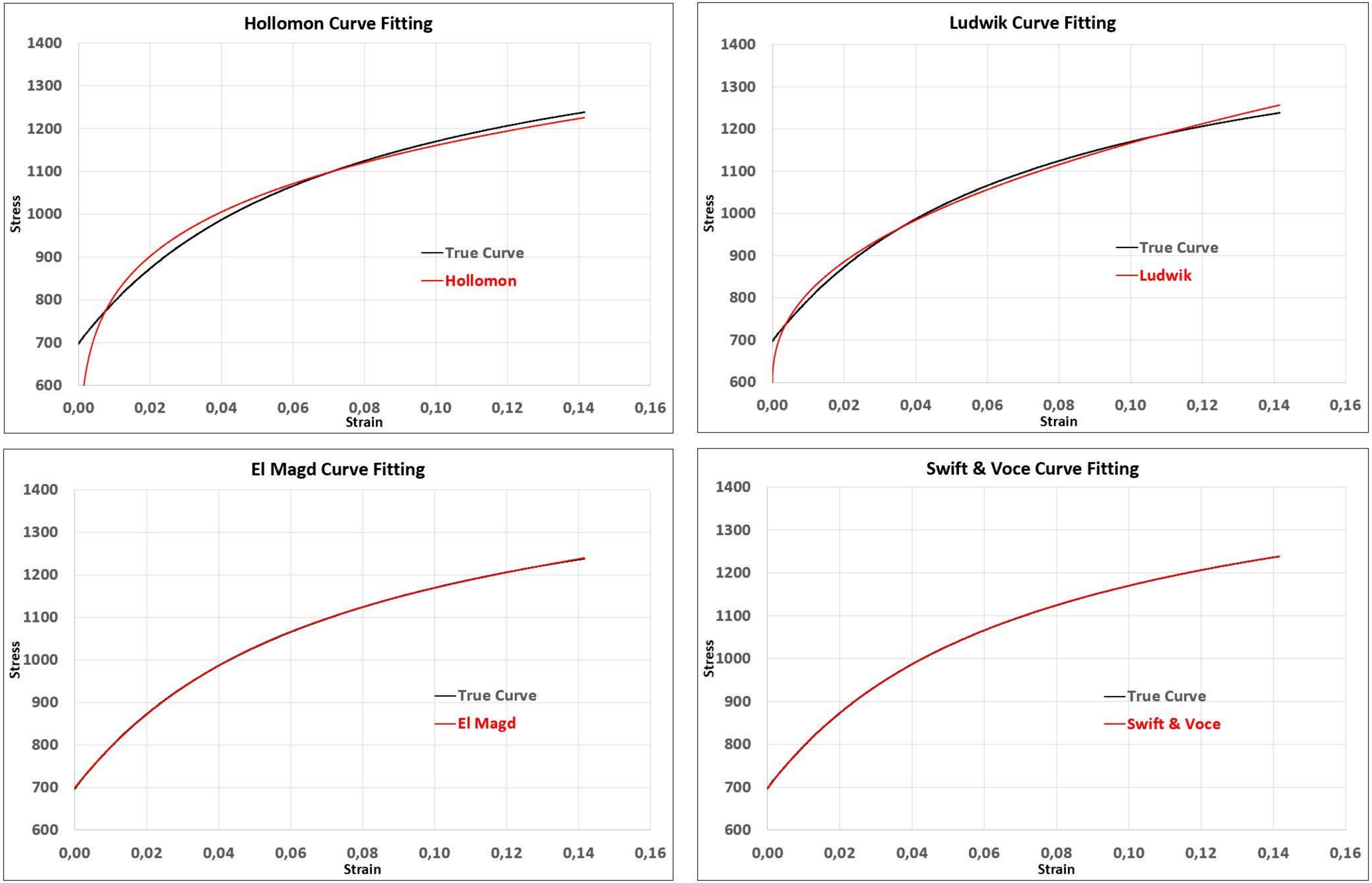

Figure 3.20: Estimated curves for the QP980 Baosteel

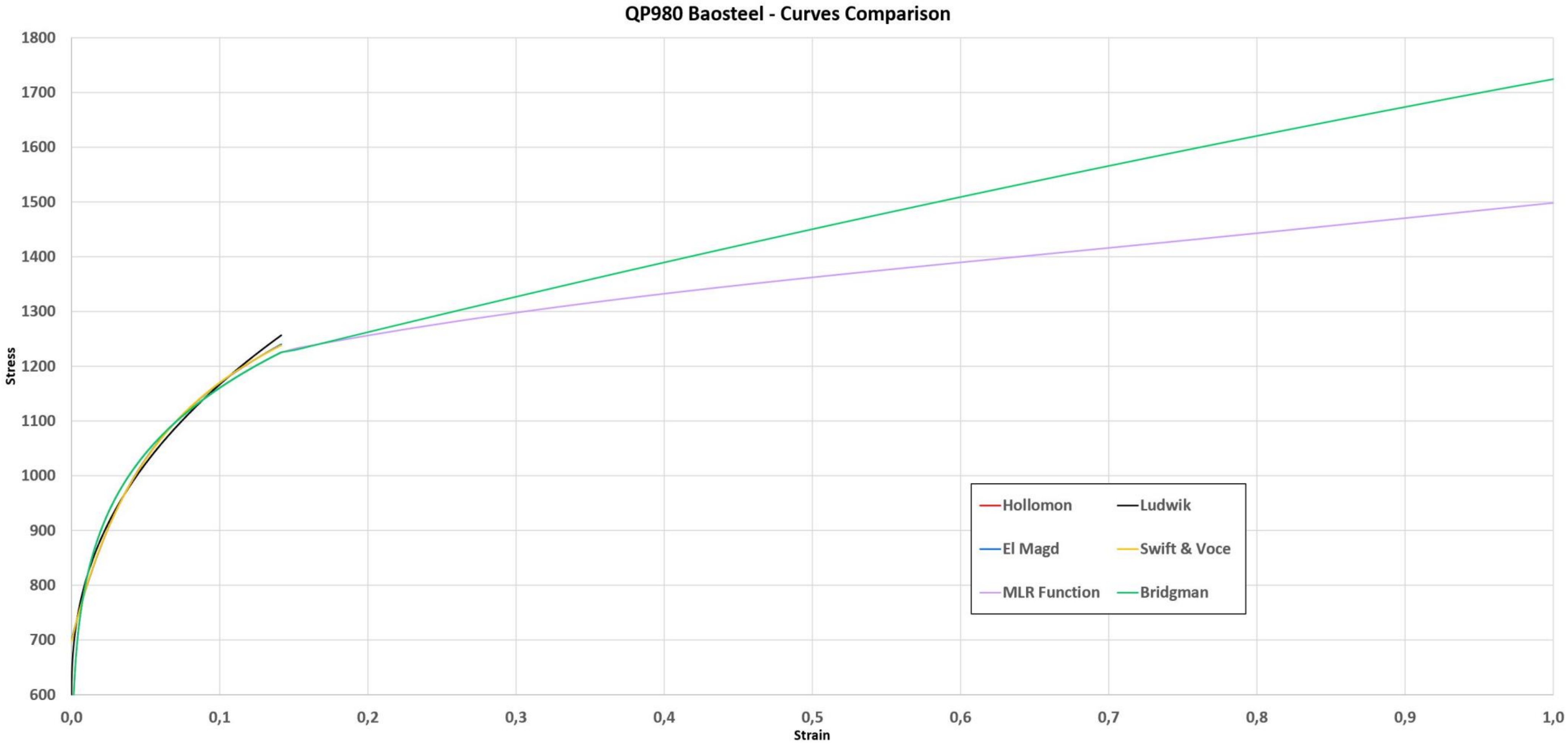

Figure 3.21: Post-necking behaviour of QP980 Baosteel steel with different estimation models

The **Hollomon** curve has been drawn by the combination of $\boldsymbol{K} = 1665{,}0\ MPa$ and $\boldsymbol{n} = 0{,}157$.

The **Ludwik** curve has been obtained by using $\boldsymbol{K} = 1503{,}3\ MPa$, $\boldsymbol{n} = 0{,}418$ and $\boldsymbol{A} = 592{,}8\ MPa$.

The **El Magd** model variables are $\boldsymbol{A} = 687{,}9\ MPa$, $\boldsymbol{\beta_1} = 1202{,}1\ MPa$, $\boldsymbol{\beta_2} = 24{,}7$, and $\boldsymbol{K} = 381{,}6\ MPa$.

The **Swift and Voce** curve has been obtained by assigning $\boldsymbol{\alpha} = 0{,}70$, so giving to the Swift component more importance. Its parameters are $\boldsymbol{K} = 1828{,}8\ MPa$, $\boldsymbol{\varepsilon_0} = 0{,}019$, and $\boldsymbol{n} = 0{,}208$.

The Voce related parameters are $\boldsymbol{k_0} = 460{,}1\ MPa$, $\boldsymbol{Q} = 787{,}0\ Mpa$ and $\boldsymbol{\beta} = 22{,}3$.

For the post-necking analysis, the **MLR** curve is characterized by $\boldsymbol{S_0} = 1141{,}9\ MPa$ and $\boldsymbol{S_1} = 696{,}1\ Mpa$, while the **Bridgman** curve is set for $\boldsymbol{B_0} = 1126{,}9\ MPa$, $\boldsymbol{B_1} = 696{,}1\ MPa$ and $\boldsymbol{B_2} = -98{,}6\ MPa$.

A very small correction for the S_0 parameter was required to avoid discontinuities in the trend of the curve.

If compared to the DP980 Usiminas steel, the Hollomon estimating model is better able to fit the true curve. It is possible to see how the positive deviations are still present, as a characteristic feature of the model, but they are halved. However, this improvement is counterbalanced by a worse approximation near the necking region, where you can see that the estimated curve remains under the true curve, while in the DP980 Usiminas steel the curves practically coincide.

Again, the trend of the Ludwik estimated curve is similar to the other previously seen, although it is possible to notice how the overall approximation is characterized by lower data deviations with respect to the true curve. The positive divergence near the necking area is still present, but this is the characteristic feature of the Ludwik estimating model.

The El Magd and Swift and Voce estimated curve proved again to be the best models. Their approximations are very good and nearly coincide with the true curve. The only thing that can be noticed is the very slightly higher estimated stresses of the El Magd model with respect to the Swift and Voce model, at the very last section of the true curve. In other words, the Swift and Voce curve is more precise than the El Magd curve, thus favouring the former to be the best fitting model so far.

Looking at Figure 3.21, we can do the same observations done in the previous case of the DP980 Usiminas steel. The maximum estimated stresses at 100% of deformations are lower, but the stress differences at same value of strain between all the models is more or less the same. An important difference is imputable to the trend of the MLR estimating method, which in that case is way more similar to the Bridgman estimated curve.

3.4.4 TBC1180 Thyssen

The TBC1180 Thyssen steel is one of the complex-phase steels produced by Thyssenkrupp Steel, one of the major and leading suppliers of advanced and high-grade steels, operating also in the automotive field. Particularly in this sector, Thyssenkrupp steels has a wide range of steels, such as deep drawing steels, high-strength steels, dual-phase steels, complex phase steels and others. One of the steels analysed is the TBC1180, a complex-phase steel. Complex-phase steels are particular types of steels which improve at best the forming properties of the material. Complex Phase steels gain their strength through extremely fine grain size and micro structure containing small amounts of martensite, pearlite and retained austenite, embedded in a ferrite-bainite matrix. High gra6in refinement is achieved by precipitation of micro alloying elements, such as Niobium (Nb), Titanium (Ti), or Vanadium (V). Complex-phase steels have a higher minimum yield strength in comparison with dual phase steels of identical tensile strengths. When compared to dual-phase steels, complex-phase steels have a much higher yield strength to tensile strength ratio. Complex-phase steels have high work hardening capability at low strain, high fatigue strength, high energy absorption, wear resistance and bake hardening potential. Compared with conventional dual-phase steels in the same strength class, these complex-phase grades offer improved hole expansion and bendability, with higher yield strength. This property profile also makes the new TBC1180 grade attractive for use in crash-relevant structural parts of vehicles. Generally, complex-phase steels find applications in body structure, suspensions, and chassis components.

Table 9 [58] and **Table 10** [58] show, respectively, the chemical and mechanical properties of TBC1180. **Figure 3.22** graphically summarizes the approximations of the true curve obtained with all the models, while **Figure 3.23** compares the post-necking behaviour of all the different estimation models.

C	Mn	Si	P	S	Al
0.20 (max)	2.60 (max)	0.80 (max)	0.08 (max)	0.015 (max)	0.015 – 2.00

Table 9: Chemical composition of TBC1180 Thyssen

Yield strength [MPa]	Tensile strength [MPa]	Elongation [%]
900 – 1070	1180	-

Table 10: Mechanical properties of TBC1180 Thyssen

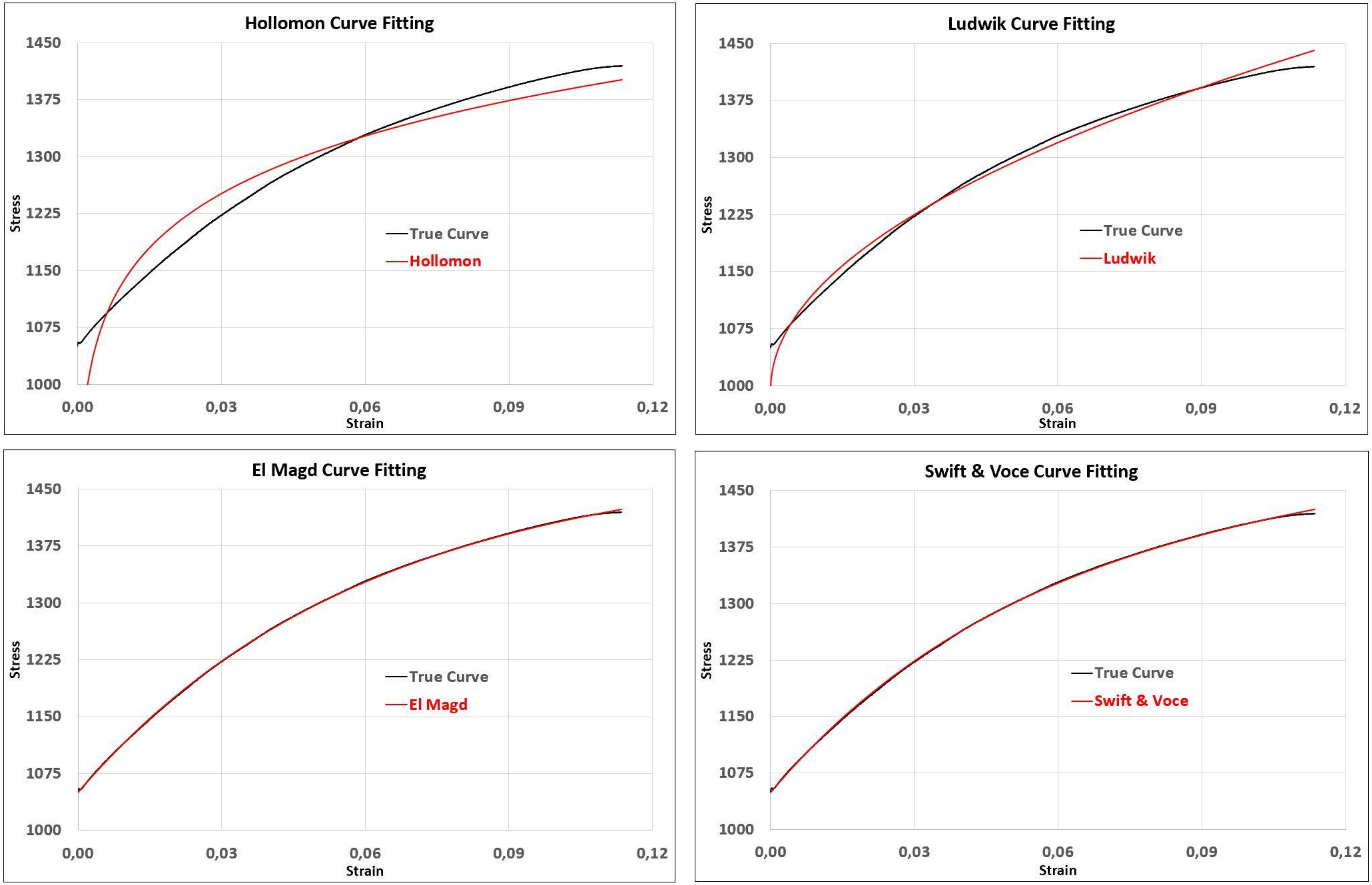

Figure 3.22: Estimated curves for the TBC1180 Thyssen

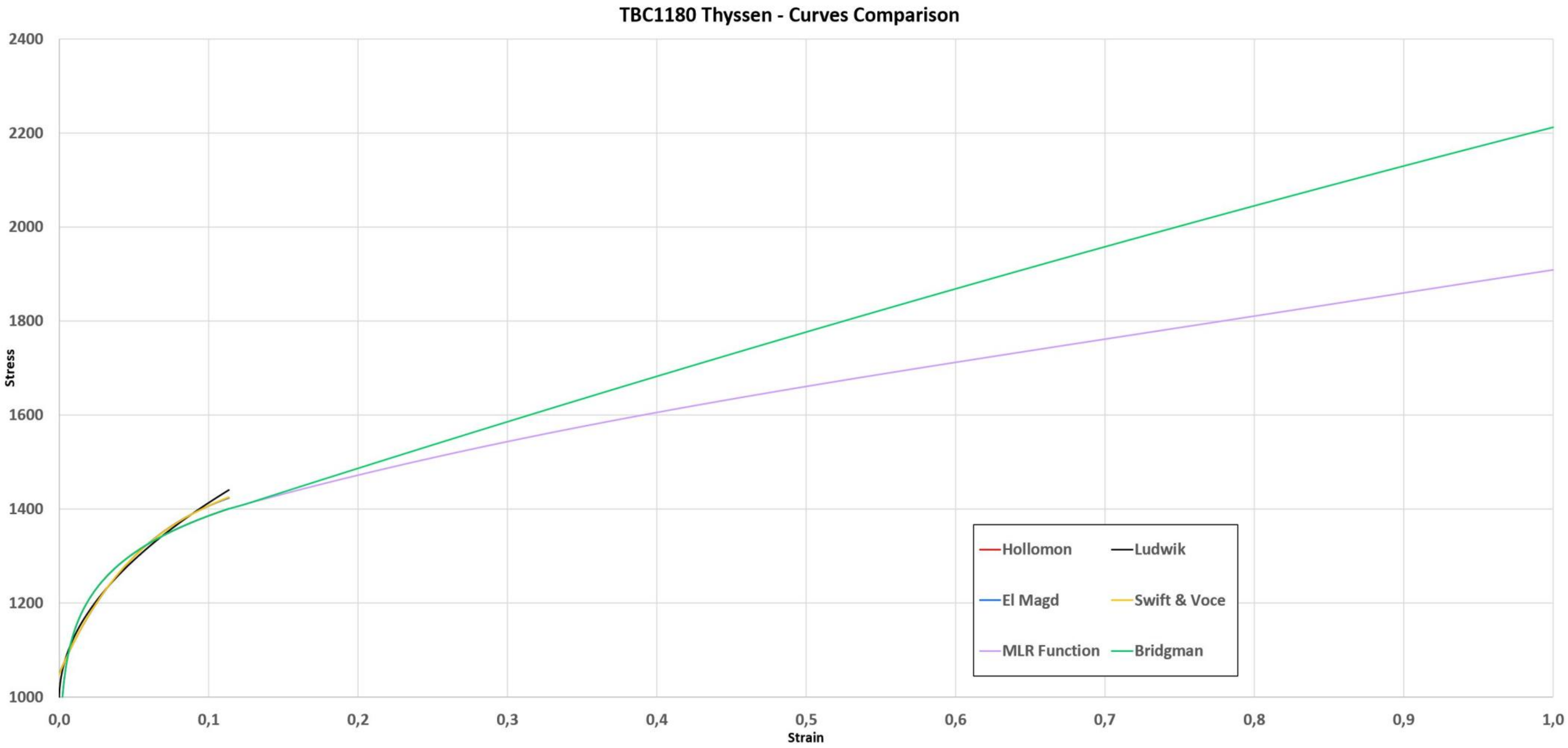

Figure 3.23: Post-necking behaviour of TBC1180 Thyssen steel with different estimation models

The **Hollomon** curve has been drawn by the combination of $\boldsymbol{K} = 1685{,}3\ MPa$ and $\boldsymbol{n} = 0{,}085$.

The **Ludwik** curve has been obtained by using $\boldsymbol{K} = 1312{,}0\ MPa$, $\boldsymbol{n} = 0{,}496$ and $\boldsymbol{A} = 994{,}5\ MPa$.

The **El Magd** model variables are $\boldsymbol{A} = 1037{,}9\ MPa$, $\boldsymbol{\beta_1} = 93{,}2\ MPa$, $\boldsymbol{\beta_2} = 17{,}2$, and $\boldsymbol{K} = 423{,}4\ MPa$.

The **Swift and Voce** curve has been obtained by assigning $\boldsymbol{\alpha} = 0{,}75$, so giving to the Swift component more importance. Its parameters are $\boldsymbol{K} = 785{,}5\ MPa$, $\boldsymbol{\varepsilon_0} = 0{,}146$, and $\boldsymbol{n} = 0{,}368$.

The Voce related parameters are $\boldsymbol{k_0} = 3033{,}5\ MPa$, $\boldsymbol{Q} = 1377{,}1\ Mpa$ and $\boldsymbol{\beta} = 19{,}8$.

For post-necking analysis, the **MLR** curve is characterized by $\boldsymbol{S_0} = 1291{,}3\ MPa$ and $\boldsymbol{S_1} = 1050{,}3\ Mpa$, while the **Bridgman** curve is set for $\boldsymbol{B_0} = 1281{,}3\ MPa$, $\boldsymbol{B_1} = 1050{,}3\ MPa$ and $\boldsymbol{B_2} = -119{,}3\ MPa$.

A very small correction for the S_0 parameter was required to avoid discontinuities in the trend of the curve.

For the TBC1180 Thyssen steels we can do similar considerations as seen so far. While the Hollomon model seems to provide a quite good fit for the DP980 Usiminas and for the QP980 Baosteel steels, in this case the model provides a very bad approximation of the true curve, with consistent data divergencies both in the positive and negative regions, similar to the ones visible in the QP1180 steel in Figure 3.13. The same happens for the Ludwik estimating model, with higher divergences in the necking zone.

Concerning the El Magd and Swift and Voce models, they are again valid choices for the true curve approximation, but notice that the El Magd model originates a very similar trend seen also for the QP1180 steel, while in that case it's the El Magd model that provides the lowest values of estimated stresses.

Conclusions

We have seen in this thesis which are the damage models used to estimate the fracture initiation process on the material, and the most common estimating models used to predict the post-necking behaviour of a steel. Both of them are implemented together to test and study the plastic behaviour of the material under examination. The procedure followed to know the validity of damage and plastic behaviour estimating models is shown in the diagram below.

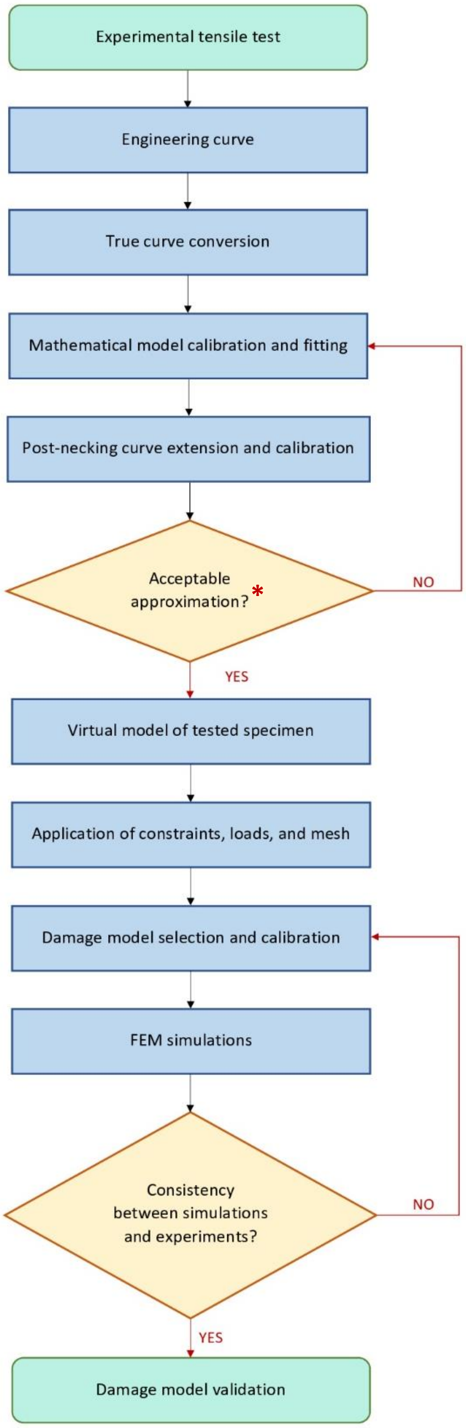

* The acceptable approximation is not only referred to the precision of the fitted curve, but also to the coherence with respect to flow plasticity theory, isotropy and anisotropy characteristics, and yielding point.

The mathematical model for true curve needs different fitting repetitions in order to be quite similar to the true curve obtained from the engineering curve. To this aim, the minimization of the sum of squared residual method has been applied. In the case in which this methodology still does not provide a satisfactory approximation, the model variables should be manually set. If also this way does not provide a good result, the model should be rejected and replaced with a more effective one. Same considerations applied for the damage models, which are used to evaluate the fracturing process. However, if problems occur during the Finite Element simulations, it is not certain that the cause is exclusively attributable to the damage model. Problems could be due to some imperfections in the mesh of the tested material, or due to incorrect executions of the virtual simulation. In case of damage models, the control process is more complex than the one related to the mathematical models used for the true curve fitting process.

The damage models here described consider always different variables, and so there's not a single model to choose and to apply directly. Every damage model could be valid for the actual analysis, or the majority of them should be avoided. The important thing is to understand which model, amongst the valid ones, could be chosen as preferred one. For example, the first model analysed was the Wierzbicki – Xue damage model. We have seen how this model, compared to others, provides more satisfactory results, due to its ability to describe the ductility evolution process as a function of the deviatoric state parameter, which correlates specific values of strains reached during the deformation to evaluate the o called *damage parameter*. The damage parameter variable is common in different damage models, but as said before it is evaluated in different ways. In the Wierzbicki – Xue damage model we have seen how the damage parameter is simply a relationship between the plastic strain and the triaxiality value, while in other models, such as the GISSMO, the damage parameter is a more complex function, which takes into account also the instability of the material, a factor which is exclusively considered in the GISSMO damage model.

GISSMO has been proved to be efficient for fracture predictions, since it can be used not only for tensile tests, but also for shear tests, as seen in this thesis. That model is very consistent with experimental tests, it provides a very good correlation between the damage observed in simulations, and the damage observed from real tests. However, it has some limitations, in the sense that the combination of the model variables does not always allow to obtain the best results in all the different tests in which it can be used. Indeed, we have seen how that model should not be used outside a certain accuracy range, although it is valid for the majority of applications.

Similar considerations can be done also for the Gurson – Tvergaard – Needleman (GTN) damage model. The biggest advantage of the GTN damage model is its flexibility in the evaluation of the plastic behaviour and fracture predictions. With a suitable combination of constitutive (q_i) and fracture (f_i) parameters, it is possible to obtain different fracture patterns, and different locations at which necking occur. This allows the GTN damage model to be used for a wide variety of applications, since it allows to analyse different loads applications, and to predict different behaviours, in order to have better estimates of what could be the real behaviour of the material. Different fracture estimations are also provided by the Kim – Yoon damage model. In fact, that model allows to estimate the fracture initiation and propagation process according to four different theories: principal plastic strain, equivalent plastic strain, maximum shear strain, and shear energy. All these methods take into account the damage parameter to set the beginning of the fracture. The outputs obtained are good approximations of the load – displacement curve of the tested material, apart from the shear energy damage model case, which provided very bad behaviours. The shear energy method is not the only limitation of the Kim – Yoon damage model. In addition, that model does not guarantee, at the same level seen for the GTN model for example, to obtain reliable results, and the studies performed by [45] are a proof. Some discrepancies are present between the fracture pattern inclination between virtual Finite Element simulations and experimental tests. The best combinations of the model variable require continuous repetitions of curve fitting operations, and a valid final result is still not guarantee. Although the fracture estimation obtained by [45] is still a good result, the Kim – Yoon model is more limited with respect to the other models described, therefore special attention is required before reaching a satisfactory level of fracture behaviour estimation. The factor which all the other models do not consider is the temperature, and the Johnson – Cook model is the only one which takes it into account for the fracture behaviour analyses. This model considers also constitutive and fracture parameters, as happens for the GTN damage model. Although the Johnson – Cook damage model provides god results, it is affected by a big limitation in case of high values of triaxiality. When this happen, the fracture pattern is not predicted correctly, which means that the virtual simulations provide notable differences with respect to what obtained in real tests.

Passing now to the mathematical plastic behaviour estimation models, also here there is no one only single solution to implement, i.e. there’s no one single estimation model which is the best in all the cases to use as a optimum solution for the material behaviour study. The final and best solution depends on the specific case considered. Let’s consider, for example, the initial material, the QP1180 quenching and partitioning steel. The mathematical model able to best fit the engineering curve is the El Magd estimating model, characterized by an average error of about 1.6%. It is possible to see that the El Magd approximations is the only one able to fit the engineering curve with a satisfactory level of precision, while the remaining estimating models’ approximations are way different. This could suggest that there could be some errors in the way in which the estimating model has been implemented, but if we have a look at the approximations obtained with the same models in the other materials, we could notice that the estimated curve approximate pretty well the engineering curve, although the Hollomon model has always some limitations. This fact means that the error, in the analysis of the QP1180 steel, could be due to the initial point of the curves set for the approximation. The models’ variables have been chosen according to the minimization of the sum of squared residuals, so it is possible that errors are imputable to it. A way to solve the problem could be the manual modification of the models’ variables, but for sure the estimated curve will deviate more from the engineering curve, or to manually change the starting point of the estimated curve. Combining both the methods it could be possible, making reference for the Hollomon model, to shift the curve vertically, and to avoid the crossing into the engineering curve. Furthermore, it could be possible to reduce the error, while obtaining the data in the necking region near the ones of the engineering curve.

Just to conclude, notice that in all the cases the El Magd model and the Swift & Voce model are the most precise and reliable ones, and they could be chosen as reference for the plastic behaviour analysis of steels.

Bibliography

[1] Rana, Radhakanta, and Shiv Brat Singh. Automotive steels: design, metallurgy, processing and applications. Woodhead Publishing, 2016.

[2] Callister Jr, William D., and David G. Rethwisch. Materials science and engineering. John Wiley & Sons, 2017.

[3] Gatto, A., Villani, G., & Secciani, A. Produzione metalmeccanica. 2006

[4] Bhadeshia, Harry, and Robert Honeycombe. Steels: microstructure and properties. Butterworth-Heinemann, 2017.

[5] Ahssi, Mohamed Ahmed Mohamed, et al. "The Effect of Nickel on the Microstructure, Mechanical Properties and Corrosion Properties of Niobium–Vanadium Microalloyed Powder Metallurgy Steels." Materials 13.18 (2020): 4021.

[6] Khanh, Pham Mai, et al. "Effects of Chromium Content and Impact Load On Microstructures and Properties of High Manganese Steel." Materials Science Forum. Vol. 804. Trans Tech Publications Ltd, 2015.

[7] Uranga, Pello, et al. "Molybdenum alloying in high-performance flat-rolled steel grades." Advances in Manufacturing 8.1 (2020): 15-34.

[8] Kaar, Simone, et al. "Effect of manganese on the structure-properties relationship of cold rolled AHSS treated by a quenching and partitioning process." Metals 9.10 (2019): 1122.

[9] Gürol, Ugur, and Kurnaz S. Can. "Effect of carbon and manganese content on the microstructure and mechanical properties of high manganese austenitic steel." Journal of Mining and Metallurgy B: Metallurgy 56.2 (2020): 171-182.

[10] Malik, Hussein I., and Abbas MR Al-Marafie. "Effect of silicon additions on the mechanical properties of eutectoid steel." Archiv für das Eisenhüttenwesen 55.5 (1984): 241-242.

[11] Samek, Ludovic, and Daniel Krizan. "Steel-material of choice for automotive lightweight applications." Metal Review (2012): 1-6.

[12] Satyendra Kumar Sarna, Interstitial. Free Steels, **https://www.ispatguru.com/interstitial-free-steels/**

[13] Majumdar, Shrabani, D. Bhattacharjee, and K. K. Ray. "Mechanism of fatigue failure in interstitial-free and interstitial-free high-strength steel sheets." Scripta Materialia 64.3 (2011): 288-291.

[14] Patel, Jitendra, Christian Klinkenberg, and Klaus Hulka. "Hot rolled HSLA strip steels for automotive and construction applications." Proc. Int. Symposium Niobium 2001. 2001.ù

[15] Catalogue of ArcelorMittal, **https://automotive.arcelormittal.com/products/flat/HYTSS/HSLA**

[16] Li, Shuo-shuo, and Hai-wen Luo. "Medium-Mn steels for hot forming application in the automotive industry." International Journal of Minerals, Metallurgy and Materials 28.5 (2021): 741-753.

[17] Flachstahl, Salzgitter. "22MnB5 boron alloyed quenched and tempered steel." Product catalogue (2014).

[18] Sun, Hongtu, et al. "Application of hot forming high strength steel parts on car body in side impact." Chinese Journal of Mechanical Engineering 2 (2010): 252.

[19] Mehdi, Y., and M. Tisza. "Formability investigations of advanced high strength steels." IOP Conference Series: Materials Science and Engineering. Vol. 448. No. 1. IOP Publishing, 2018.

[20] Catalogue of ArcelorMittal, **https://automotive.arcelormittal.com/products/flat/first_gen_AHSS/DP**

[21] **http://www.nationalmaterial.com/introduction-dual-phase-steels/dual-phase-steel-picture/#iLightb ox[postimages]/0**

[22] Krizan, Daniel. "TRIP steels: advanced high strength multiphase steels for automotive applications." Proc Int Conf. 2006.

[23] Zhang, Yinghui, et al. "Mechanical properties and microstructure of TRIP steels produced using TSCR process." Journal of University of Science and Technology Beijing, Mineral, Metallurgy, Material 13.5 (2006): 416-419.

[24] Tisza, Miklós. "Development of lightweight steels for automotive applications." Engineering Steels and High Entropy-Alloys. IntechOpen, 2020.

[25] Eun Jung Seo, Lawrence Cho, Bruno C. De Cooman, “Kinetics of the partitioning of carbon and substitutional alloying elements during quenching and partitioning (QP) processing of medium Mn steel”, Acta Materialia, Volume 107, 2016, Pages 354-365.

[26] Wang, Li, and John G. Speer. "Quenching and partitioning steel heat treatment." Metallography, Microstructure, and Analysis 2.4 (2013): 268-281.

[27] Nutor, Raymond Kwesi, Nana Kwabena Adomako, and Y. Z. Fang. "Using the Hollomon model to predict strain-hardening in metals." American Journal of Materials Synthesis and Processing 2.1 (2017): 1.

[28] Tu, Shengwen, et al. "Stress–strain curves of metallic materials and post-necking strain hardening characterization." Fatigue & Fracture of Engineering Materials & Structures 43.1 (2020): 3-19.

[29] Joun, Mansoo, et al. "Finite element analysis of tensile testing with emphasis on necking." Computational Materials Science 41.1 (2007): 63-69.

[30] M. Considère. “Annales des Ponts et Chaussées”, 9 (1885), pp. 574-775

[31] Lemaitre, Jean, ed. Handbook of Materials Behavior Models, Three-Volume Set: Nonlinear Models and Properties. Elsevier, Section 4.1 (2001): 197-198.

[32] Gupta, Manish Kumar, and Nilamber Kumar Singh. "Modelling and simulation on deformation behaviour of Al2014-T6 alloy beyond necking." Materials Today: Proceedings 44 (2021): 4204-4208.

[33] Şener, Bora, and M. Yurci. "Comparison of Quasi-Static Constitutive Equations and Modeling of Flow Curves for Austenitic 304 and Ferritic 430 Stainless Steels." (2017).

[34] Lourakis, Manolis IA. "A brief description of the Levenberg-Marquardt algorithm implemented by levmar." Foundation of Research and Technology 4.1 (2005): 1-6.

[35] Kim, J-H., et al. "Characterization of the post-necking strain hardening behavior using the virtual fields method." International Journal of Solids and Structures 50.24 (2013): 3829-3842.

[36] Mirone, Giuseppe. "Approximate model of the necking behaviour and application to the void growth prediction." International Journal of Damage Mechanics 13.3 (2004): 241-261.

[37] Mirone, Giuseppe. "A new model for the elastoplastic characterization and the stress–strain determination on the necking section of a tensile specimen." International Journal of Solids and Structures 41.13 (2004): 3545-3564.

[38] La Rosa, G., et al. "Numerical verification of the Bridgman model for notched and unnotched round specimens." WIT Transactions on Engineering Sciences 26 (2000).

[39] Berger, Andre. Numerical Modelling of Composite Materials Based on a Combined Manufacturing and Crash Simulation. Diss. Queen Mary University of London, 2014.

[40] Šebek, František, et al. "Phenomenological Ductile Fracture Criteria Applied to the Cutting Process." International Journal of Aerospace and Mechanical Engineering 8.12 (2014): 1342-1345.

[41] Wierzbicki, Tomasz, et al. "Calibration and evaluation of seven fracture models." International Journal of Mechanical Sciences 47.4-5 (2005): 719-743.

[42] Andrade, F. X. C., et al. "An incremental stress state dependent damage model for ductile failure prediction." International Journal of Fracture 200.1 (2016): 127-150.

[43] Sancho, A., et al. "An experimental methodology to characterise post-necking behaviour and quantify ductile damage accumulation in isotropic materials." International Journal of Solids and Structures 176 (2019): 191-206.

[44] Ockewitz, A., et al. “Damage Modelling of Automobile Components of Aluminium Material under Crash Loading”, Fraunhofer-Institut für Werkstoffmechanik Freiburg, 2006.

[45] Kim, Jong-Bong, and Jeong Whan Yoon. Necking behavior of AA 6022-T4 based on the crystal plasticity and damage models. International Journal of Plasticity 73 (2015) 3-23.

[46] Springmann, M., and M. Kuna. "Identification of material parameters of the Gurson–Tvergaard–Needleman model by combined experimental and numerical techniques." Computational Materials Science 33.4 (2005): 501-509.

[47] Slimane, Abdelkader, et al. "Parametric study of the ductile damage by the Gurson–Tvergaard–Needleman model of structures in carbon steel A48-AP." Journal of Materials Research and Technology 4.2 (2015): 217-223.

[48] Xu, Yidong, and Chunxiang Qian. "Application of Gurson–Tvergaard–Needleman constitutive model to the tensile behavior of reinforcing bars with corrosion pits." Plos one 8.1 (2013): e54368.

[49] International Digital Image Correlation Society, Jones, E.M.C. and Iadicola, M.A. (Eds.). "A Good Practises Guide for Digital Image Correlation", 2018.

[50] 2D – 3D Stereo Digital Image Correlation, Catalogue of LaVision, https://www.lavision.de/en/products/strainmaster/2d-stereo-dic/

[51] https://www.youtube.com/watch?v=kfP9XRz2vo0&t=863s&ab_channel=CorrelatedSolutions

[52] https://en.wikipedia.org/wiki/Stress%E2%80%93strain_curve

[53] Faridmehr, I., Osman, M. H., Adnan, A. B., Nejad, A. F., Hodjati, R., Azimi, M. (2014). "Correlation between engineering stress-strain and true stress-strain curve." American Journal of Civil Engineering and Architecture, 2(1), 53-59.

[54] https://en.wikipedia.org/wiki/Stress%E2%80%93strain_curve#/media/File:Stress_strain_ comparison.svg

[55] Madrid, M., et al. "Hole expansion ratio in intercritically annealed QP 980/1180 steel grades as a function of testing condition." IOP Conference Series: Materials Science and Engineering. Vol. 418. No. 1. IOP Publishing, 2018.

[56] Catalogue of Usiminas, **https://www.usiminas.com/?lang=en**

[57] Catalogue of Baosteel, **https://www.baosteel.com/group_en/**

[58] Catalogue of ThyssenKrupp, **https://www.thyssenkrupp-steel.com/en/**